

The evolution of sulphur-bearing molecules in high-mass star-forming cores

F. Fontani^{1,2,3}, E. Roueff², L. Colzi⁴, and P. Caselli³

¹ INAF - Osservatorio Astrofisico di Arcetri, Largo E. Fermi 5, I-50125, Florence (Italy)
e-mail: francesco.fontani@inaf.it

² LERMA, Observatoire de Paris, PSL Research University, CNRS, Sorbonne Université, F-92190 Meudon (France)

³ Centre for Astrochemical Studies, Max-Planck-Institute for Extraterrestrial Physics, Giessenbachstrasse 1, 85748 Garching, Germany

⁴ Centro de Astrobiología (CSIC-INTA), Ctra Ajalvir km 4, 28850, Torrejón de Ardoz, Madrid (Spain)

Received xxx; accepted yyy

ABSTRACT

Context. To understand the chemistry of sulphur (S) in the interstellar medium, models need to be tested by observations of S-bearing molecules in different physical conditions.

Aims. We aim to derive column densities and abundances of S-bearing molecules in high-mass dense cores in different evolutionary stages and with different physical properties.

Methods. We analyse observations obtained with the Institut de RadioAstronomie Millimétrique (IRAM) 30m telescope towards 15 well-known cores classified in the three main evolutionary stages of the high-mass star-formation process: high-mass starless cores, high-mass protostellar objects, and ultracompact HII regions.

Results. We have detected rotational lines of SO, SO⁺, NS, C³⁴S, ¹³CS, SO₂, CCS, H₂S, HCS⁺, OCS, H₂CS, and CCCS. We also analyse for the first time lines of the NO molecule to complement the analysis. From a local thermodynamic equilibrium approach, we have derived column densities of each species and excitation temperatures for those detected in multiple lines with different excitation. Based on a statistical analysis on the line widths and the excitation temperatures, we find that: NS, C³⁴S, ¹³CS, CCS, and HCS⁺ trace cold, quiescent, and likely extended material; OCS, and SO₂ trace warmer, more turbulent, and likely denser and more compact material; SO and perhaps SO⁺ trace both quiescent and turbulent material depending on the target. The nature of the emission of H₂S, H₂CS and CCCS is less clear. The molecular abundances of SO, SO₂, and H₂S show the strongest positive correlations with the kinetic temperature, believed to be an evolutionary indicator. Moreover, the sum of all molecular abundances show an enhancement of gaseous S from the less evolved to the more evolved stages. These trends could be due to the increasing amount of S sputtered from dust grains owing to the increasing protostellar activity with evolution. The average abundances in each evolutionary group increase especially in the oxygen-bearing molecules, perhaps due to the increasing abundance of atomic oxygen with evolution owing to photodissociation of water in gas phase.

Conclusions. Our observational work represents a test-bed for theoretical studies aimed at modelling the chemistry of sulphur during the evolution of high-mass star-forming cores.

Key words. astrochemistry – line: identification – ISM: molecules – stars: formation

1. Introduction

Sulphur (S) is one of the most mysterious elements from an astrochemical point of view. It has a cosmic abundance relative to hydrogen of 1.73×10^{-5} (Lodders 2003), and its ionised form has a relative abundance of 1.66×10^{-5} (Esteban et al. 2004), in close agreement with previous derivation in the Ionised Orion Nebula. This makes it the tenth most abundant element in the Universe. Sulphur is also the sixth most important biogenic element after hydrogen, oxygen, carbon, nitrogen, and phosphorus. It is a key component in most proteins, since it is contained in the methionine (C₅H₁₁NO₂S) and cysteine (C₃H₇NO₂S) amino acids, and a (minor) constituent of fats, biological fluids, and skeletal minerals. Also, in the form of H₂S, it can replace water in the photosynthesis of some bacteria. Nevertheless, its chemical behaviour in the interstellar medium (ISM), and in particular in star-forming molecular clouds, is still not well-understood.

The chemistry of sulphur in the ISM has been studied for a long time (e.g. Oppenheimer & Dalgarno 1974; Pineau des

Forêts et al. 1986; Drdla et al. 1989; Turner 1995; Goicoechea et al. 2006; Fuente et al. 2019; Navarro-Almáida et al. 2020; Esplugues et al. 2022), but still a major problem remains unsolved: what is the main reservoir (i.e. both in gas and in ice mantles of dust grains) of sulphur in the ISM? The problem arises from the fact that, despite observations of the diffuse interstellar medium suggest a negligible elemental depletion of S in solid phase (Howk, Sembach & Savage 2006; Jenkins 2009), its abundance in the gas-phase seen through molecular emission is at most a few percent of the cosmic value (McGuire 2018; see also references in Table 1 of Woods et al. 2015). A natural explanation would be severe freeze-out of S-bearing species on ice mantles of dust grains. However, measured abundances of S-bearing molecules on ices are too low to solve the problem. OCS and SO₂ (e.g. Boogert et al. 2015; McClure et al. 2023) were detected on ice mantles, but their abundances can account for only ~ 4% of the cosmic sulphur abundance. Theoretical models predict that H₂S should be one of the most important sulphur reservoirs on ice mantles owing to hydrogenation of atomic S

(Vidal et al. 2017), but observations of H₂S on ices around high-mass young stellar objects again provide upper limit abundances much lower than the S cosmic abundance (Jiménez-Escobar & Muñoz-Caro 2011). Recently Heyl et al (2022) have constrained the binding energies of various species on dust grains from available observations but acknowledge the uncertainties linked to sulphur containing species.

In addition to the problem of the missing volatile sulphur, even the formation of some S-bearing molecules detected in the gas-phase is unclear. For example, not only $S^+ + H_2 \rightarrow SH^+ + H$, which should be one of the most important reactions initiating sulphur chemistry, is strongly endothermic (by 9860 K, Millar et al. 1986), but the following $SH^+ + H_2 \rightarrow H_2S^+ + H$ and $H_2S^+ + H_2 \rightarrow H_3S^+ + H$ reactions are also endothermic by 6380 and 2900 K, respectively, due to the much higher binding energy of the reactants with respect to the products. Even in shocked material such as L1157 B1, S-bearing species can account for only small fractions of the cosmic sulphur abundance (e.g. Holdship et al. 2019).

To progress in this compelling but controversial aspect of astrochemistry and put stringent constraints on models, (accurate) abundance measurements of S-bearing species must be provided. The approach adopted in previous studies was twofold: either from line surveys of targeted objects with known physical structure (e.g. Esplugues et al. 2014; Fuente et al. 2016; Vastel et al. 2018; Cernicharo et al. 2021; Fuente et al. 2023), or from selected atomic or molecular lines in source surveys (e.g. Hatchell et al. 1998; Herpin et al. 2009; Anderson et al. 2013; Hily-Blant et al. 2022). Direct (Anderson et al. 2013) observational studies of atomic S in shocked regions or indirect (Hily-Blant et al. 2022) studies of young starless or protostellar cores suggest that an important component of volatile sulphur in the ISM may be in gaseous atomic form. In comet 67P/Churyumov-Gerasimenko, the abundance of atomic S in the coma is very high, and the total elemental abundance does not show depletion with respect to the Solar photospheric abundance (Calmonte et al. 2016; Altwegg et al. 2019). Model predictions indicate that H₂S, as well as organosulphur species and allotropes of S such as S₈, can be important sulphur reservoirs in ices (Laas & Caselli 2019; Shingledecker et al. 2020). These predictions are corroborated by laboratory experiments. For example, Cazaux et al. (2022) proposed that S⁺ in translucent clouds can favour the formation of long S chains, contributing significantly to S depletion in dense regions. But further, accurate abundance measurements of S-bearing molecules both in the gas-phase and on ices are required to better constrain the abundances of sulphur reservoirs and their variation with evolution.

In this framework, high-mass star-forming cores can play a relevant role. First, they have molecular spectra richer of lines than their low-mass counterparts, in particular in the stage of "hot molecular cores" (HMC, e.g. Kurtz et al. 2000; Fontani et al. 2007; Rivilla et al. 2017), but also in earlier evolutionary stages (e.g. Vasyunina et al. 2011; Taniguchi et al. 2018; Coletta et al. 2020; Mininni et al. 2021). Second, they are likely the birthplace of most stars in the Galaxy (e.g. Carpenter 2000; Evans et al. 2009), probably including the Sun (Adams 2010; Pflanzner 2013), and hence the chemical evolution of these regions can give us relevant constraints on the environmental conditions of the birthplace of the Solar system.

In this work, we present observations of S-bearing molecules towards 15 high-mass star forming regions, equally divided in three evolutionary classes: high-mass starless cores (HMSCs), which are infrared-dark, dense ($n \geq 10^3 - 10^5$) cm⁻³, and cold ($T_k \sim 10-20$ K) molecular clouds in an evolutionary stage im-

Table 1. List of the observed sources.

source	RA(J2000) h:m:s	Dec(J2000) °:′:″	V_{LSR}^a (km s ⁻¹)	acronym ^b
HMSC				
I00117-MM2	00:14:26.3	+64:28:28	-36.3	00117b
AFGL5142-EC ^w	05:30:48.7	+33:47:53	-3.9	AFGLa
05358-mm3 ^w	05:39:12.5	+35:45:55	-17.6	05358a
I20293-WC	20:31:10.7	+40:03:28	+6.3	20293a
I22134-B	22:15:05.8	+58:48:59	-18.3	22134b
HMPO				
I00117-MM1	00:14:26.1	+64:28:44	-36.3	00117a
05358-mm1	05:39:13.1	+35:45:51	-17.6	05358b
18517+0437	18:54:14.2	+04:41:41	+43.7	18517
I21307	21:32:30.6	+51:02:16	-46.7	21307
I23385	23:40:54.5	+61:10:28	-50.5	23385
UCHII				
G75-core ^c	20:21:44.0	+37:26:38	+0.2	G75
19410+2336	19:43:11.4	+23:44:06	+22.4	19410
I22134-VLA1	22:15:09.2	+58:49:08	-18.3	22134
23033+5951	23:05:24.6	+60:08:09	-53.0	23033
NGC7538-IRS9	23:14:01.8	+61:27:20	-57.0	NGC7538

Notes. ^(a) velocity at which we centred the spectra, corresponding to the systemic velocity; ^(b) acronym used in this paper; ^(c) Hyper-compact HII region. ^(w) "warm" ($T \geq 20$ K) HMSCs externally heated (Fontani et al. 2011).

diately before (or at the very beginning of) the gravitational collapse; high-mass protostellar objects (HMPOs), which are collapsing cores with evidence of at least one deeply embedded infrared-bright protostar, characterised typically by densities and temperatures higher than in the previous stage ($n \simeq 10^6$ cm⁻³, $T \geq 20$ K); ultra-compact HII regions (UCHII), which are cores containing at least one embedded Zero-Age-Main-Sequence star associated with an expanding HII region, whose surrounding molecular cocoon ($n \geq 10^5$ cm⁻³, $T_k \sim 20 - 100$ K) can be affected by its progressive expansion and by heating and irradiation from the central star.

The paper is organised as follows: the source sample, the observations, and the data reduction are described in Sect. 2; the results are shown in Sect. 3, and discussed in Sect. 4. Conclusions and future perspectives are given in Sect. 5

2. Sample, observations, and data reduction

2.1. Sample

We have studied 15 high-mass star-forming cores selected from the sample of Fontani et al. (2011), and extensively used to investigate specific aspects of (astro-)chemical evolution (e.g. Fontani et al. 2014; 2015a; 2015b; 2018; 2021; Colzi et al. 2018; Mininni et al. 2018; Coletta et al. 2020; Rivilla et al. 2020a). We have selected a comparable number of sources belonging to the three evolutionary groups described in Sect. 1 (i.e. HMSCs, HMPOs, and UCHII) without applying any specific selection criterion to avoid selection biases due to a specific physical parameter. In Fontani et al. (2011), five of these cores are classified as HMSCs, six as HMPOs, and four as UCHII. One of the HMPOs, G75, contains a hyper-compact HII region, and in this paper we have considered it as belonging to the UCHII group, bearing in mind that this object is in between the HMPO and the UCHII groups from the evolutionary point of view. The HMSCs AFGLa and

05358a have kinetic temperature, T_k , higher than 20 K. Both cores are likely externally heated by a nearby protostellar core (Colzi et al. 2019; Rivilla et al. 2020b) whose emission at 3mm could be partly included in the telescope beam, and are classified as "warm" cores in Fontani et al. (2011). In the case of 05358a, we observed also the nearby protostar 05358b. The other HMSCs have $T_k < 20$ K and are labelled as "quiescent" in Fontani et al. (2011). The targets are listed in Table 1. Additional information (e.g. source distances, bolometric luminosities of the associated star forming regions, reference papers) are given in Table 1 of Fontani et al. (2011).

2.2. Observations

The observed transitions of S-bearing molecules are listed in Table 2. Rest frequencies, quantum numbers, energy of the lower and upper energy level, and Einstein coefficients are taken from the Cologne Database for Molecular Spectroscopy (CDMS, Endres et al. 2016) and the Jet Propulsion Laboratory (JPL, Pickett et al. 1998). Some transitions have been detected in the datasets described in Fontani et al. (2015b) and Colzi et al. (2018). They are labelled in Table 2. The others have been observed in January and March 2017 (IRAM 30m project 116-16, PI: Fontani). For the latter observing run, observations were performed in band E2 of the EMIR receiver, covering the frequency ranges 250.540-258.320 GHz and 266.220-274.000 GHz with the Fast Fourier Transform spectrometer at 200 kHz resolution (FTS200). We observed each source in Wobbler-switching mode, with a Wobbler throw of $\pm 120''$. The observations were calibrated with the Chopper-Wheel technique (Kutner & Ulich 1981). Pointing was checked at the beginning of each observing day, and every hour towards nearby quasars. Focus was checked on planets at the beginning of each observing run, and after sunset and sunrise. System temperature was variable source by source, ranging from ~ 170 K to ~ 700 K, with an average value of ~ 300 K.

The spectra were obtained in antenna temperature units, T_A^* and converted in main beam temperature units, T_{MB} , from the formula $T_A^* = T_{MB}(B_{\text{eff}}/F_{\text{eff}}) = T_{MB}\eta_{MB}$, where $\eta_{MB} = B_{\text{eff}}/F_{\text{eff}}$ is the ratio between the main beam efficiency and the forward efficiency of the telescope. At the frequencies observed in this work, $B_{\text{eff}} \sim 0.46$ and $F_{\text{eff}} \sim 0.88$. For completeness, in Table 3 we show the spectral parameters of NO, a species that does not contain S but that we analyse in this paper for the first time to help the overall interpretation of the results (Sections 3 and 4). In particular, the comparison between NS and NO is useful to explore the relative S/O ratio in the various sources, and investigate trends as a function of the evolutionary stage.

2.3. Data reduction

The first steps of the data reduction (e.g. average of the scans, baseline removal, flag of bad scans and channels) were made with the CLASS package of the GILDAS¹ software using standard procedures. Then, the baseline-subtracted spectra in main beam temperature (T_{MB}) units were fitted with the MADRID Data CUBE Analysis (MADCUBA², Martín et al. 2019) software.

The transitions of S-bearing species listed in Table 2 were identified via the Spectral Line Identification and Local Thermodynamic Equilibrium Modelling (SLIM) tool of MADCUBA,

which assumes Local Thermodynamic Equilibrium (LTE) conditions. The lines were fitted with the AUTOFIT function of SLIM. This function produces the synthetic spectrum that best matches the data assuming as input parameters: total molecular column density (N_{tot}), radial systemic velocity of the source (V), line full-width at half-maximum (FWHM), excitation temperature (T_{ex}), and angular size of the emission (θ_S). AUTOFIT assumes that V , FWHM, θ_S , and T_{ex} are the same for all transitions fitted simultaneously. In each source, all transitions of a given molecule have been fit simultaneously.

The input parameters have all been left free except θ_S , for which we assumed that the emission fills the telescope beam. This assumption could not be appropriate in some sources and some lines. However, we do not have interferometer observations of the observed lines from which the angular emitting size can be estimated. Some targets have been observed at high-angular resolution in S-bearing molecules. For example, Beuther et al. (2009) observed 05358-mm3 and derived angular emitting sizes of a few arcseconds in $C^{34}S$ and SO_2 but in lines at much higher excitation (i.e. above 100 K) than ours. Wang et al. (2016) observed the $SO J(K) = 6(5) - 5(4)$ transition towards I22134-VLA1, and found several clumps of a few arcseconds within the beam of our data, which is unlikely to be representative of all transitions we have observed. Therefore, we decided to assume a unity filling factor, bearing in mind that this can introduce large uncertainties in the individual column densities. However, in computing the fractional abundances, the neglected dilution factor in the molecular column density is compensated (at least partially) by the comparable neglected dilution factor on the H_2 column density.

Some spectra show deviations from the LTE approximation, especially in the SO and SO_2 lines. Figs. A.3, A.4 and A.5 show that in some sources (e.g. AFGLa, G75, 05358b, NGC7538), some lines of SO and SO_2 are underestimated by the best fit, while others are overestimated. The lines that are underestimated by the fit could be either blended with nearby transitions of other species, and/or be in non-LTE conditions. The lines that are overestimated are likely in non-LTE conditions, for example due to multiple components with different temperatures that make the approximation of a single T_{ex} , inappropriate.

In this respect, some sources require a comment:

(i) the warm HMSC AFGLa (Fig. A.3): the $SO J(K) = 6(5) - 5(4)$ line is underestimated by a factor three by AUTOFIT. We have used RADEX on-line³ to investigate the effect of non-LTE conditions. Using the line width estimated in the LTE approach, that is 4.4 km s^{-1} , assuming $N_{\text{tot}} = 5 \times 10^{14} \text{ cm}^{-2}$, $T_{\text{ex}} = 100$ K, and a H_2 volume density of $\sim 10^9 \text{ cm}^{-3}$, the intensity of the $J(K) = 6(5) - 5(4)$ transition is ~ 6 K and that of the $J(K) = 2(2) - 1(1)$ line is ~ 1 K, as observed. However, the other two lines should be stronger than observed, maybe because of a different beam dilution not taken into account by RADEX. Hence, even a non-LTE approach does not allow to fit all lines properly. The OCS lines also show deviations from the LTE approach (Fig. A.13), but even in this case neither a non-LTE approach significantly improves the predicted intensity of the three lines, nor a fit with two velocity features with different line width.

(ii) the HMPO 23385 (Fig. A.4): the presence of two Gaussian features separated in radial velocity by $\sim +3.5 \text{ km s}^{-1}$ is clear in $SO J(K) = 2(1) - 1(1)$ and $J(K) = 6(5) - 5(4)$, and maybe also in the CCCS line (Fig. A.19). This second velocity feature was already revealed in previous observations of HCN and HNC isotopologues (Colzi et al. 2018), and it is likely due to a

³ <https://var.sron.nl/radex/radex.php>

¹ <https://www.iram.fr/IRAMFR/GILDAS/>

² MADCUBA is a software developed in the Madrid Center of Astrobiology (INTA-CSIC) which enables to visualise and analyse single spectra and data cubes: <https://cab.inta-csic.es/madcuba/>.

Table 2. Spectral parameters of the observed lines of the analysed S-bearing species

Line ^a	ν_0 (GHz)	E_l (K)	E_u (K)	A_{ul} (s ⁻¹)	Ref. ^b	θ_{MB}^c ($''$)
¹³ CS						
$J = 2 - 1$	92.494308	2	7	1.41×10^{-5}	Fontani et al. (2015b)	~ 27
C ³⁴ S						
$J = 2 - 1$	96.41294	2	6	1.60×10^{-5}	Fontani et al. (2015b)	~ 26
SO						
$J(K) = 2(2) - 1(1)$	86.09395	15	19	0.50×10^{-5}	Colzi et al. (2018)	~ 29
$J(K) = 6(5) - 5(4)$	219.949442	24	35	1.34×10^{-4}	Fontani et al. (2015b)	~ 11
$J(K) = 5(6) - 4(5)$	251.82577	39	51	1.93×10^{-4}	this work	~ 10
$J(K) = 8(9) - 8(8)$	254.573628	87	100	0.42×10^{-5}	this work	~ 10
$J(K) = 6(6) - 5(5)$	258.255826	44	56	2.12×10^{-4}	this work	~ 10
$J(K) = 3(4) - 4(3)$	267.197746	16	29	7.1×10^{-7}	this work	~ 9
SO ⁺						
$J = 11/2 - 9/2, \Omega = 1/2, l = e$	254.977935	27	39	8.63×10^{-5}	this work	~ 10
$J = 11/2 - 9/2, \Omega = 1/2, l = f$	255.353237	27	39	8.67×10^{-5}	this work	~ 10
NS ^d						
$J = 11/2 - 9/2, F = 13/2 - 11/2$ $\Omega = 1/2, l = e$	253.570476	27	39	2.83×10^{-4}	this work	~ 10
$J = 11/2 - 9/2, F = 13/2 - 11/2$ $\Omega = 1/2, l = f$	253.968393	28	40	2.84×10^{-4}	this work	~ 10
CCS						
$N(J) = 7(6) - 6(5)$	86.181391	19	23	2.78×10^{-5}	Colzi et al. (2018)	~ 29
$N(J) = 7(7) - 6(6)$	90.686381	21	26	3.29×10^{-5}	Fontani et al. (2015b)	~ 27
$N(J) = 7(8) - 6(7)$	93.870107	15	20	3.80×10^{-5}	Fontani et al. (2015b)	~ 26
$N(J) = 13(12) - 12(12)$	94.9394789	57	62	3.9×10^{-7}	Fontani et al. (2015b)	~ 26
$N(J) = 12(11) - 11(10)$	153.4497738	46	54	1.66×10^{-4}	Colzi et al. (2018)	~ 16
$N(J) = 17(18) - 16(17)$	221.0711222	88	98	5.07×10^{-4}	Fontani et al. (2015b)	~ 11
$N(J) = 7(6) - 7(7)$	223.5624057	15	26	3.06×10^{-6}	Fontani et al. (2015b)	~ 11
$N(J) = 10(10) - 9(10)$	254.2139143	31	43	3.21×10^{-6}	Fontani et al. (2015b)	~ 10
HCS ⁺						
$J = 2 - 1$	85.34789	2	6	1.11×10^{-5}	Colzi et al. (2018)	~ 29
$J = 6 - 5$	256.0271	31	43	3.46×10^{-4}	this work	~ 10
p-H ₂ S						
$J(K_a, K_b) = 2(2, 0) - 2(1, 1)$	216.710437	74	84	4.87×10^{-5}	Fontani et al. (2015b)	~ 11
OCS						
$J = 18 - 17$	218.903356	89	100	3.04×10^{-5}	Fontani et al. (2015b)	~ 11
$J = 21 - 20$	255.374456	123	135	4.84×10^{-5}	this work	~ 10
$J = 22 - 21$	267.530219	135	148	5.57×10^{-5}	this work	~ 9
SO ₂						
$J(K_a, K_b) = 8(3, 5) - 9(2, 8)$	86.6390877	51	55	1.34×10^{-6}	Colzi et al. (2018)	~ 28
$J(K_a, K_b) = 11(1, 11) - 10(0, 10)$	221.9652196	50	60	1.14×10^{-4}	Fontani et al. (2015b)	~ 11
$J(K_a, K_b) = 13(1, 13) - 12(0, 12)$	251.199675	70	82	1.76×10^{-4}	this work	~ 10
$J(K_a, K_b) = 8(3, 5) - 8(2, 6)$	251.2105851	43	55	1.20×10^{-4}	this work	~ 10
$J(K_a, K_b) = 6(3, 3) - 6(2, 4)$	254.2805358	29	41	1.14×10^{-4}	this work	~ 10
$J(K_a, K_b) = 4(3, 1) - 4(2, 2)$	255.5533022	19	31	9.28×10^{-5}	this work	~ 10
$J(K_a, K_b) = 3(3, 1) - 3(2, 2)$	255.9580440	15	28	6.63×10^{-5}	this work	~ 10
$J(K_a, K_b) = 5(3, 3) - 5(2, 4)$	256.2469451	24	36	1.07×10^{-4}	this work	~ 10
$J(K_a, K_b) = 7(3, 5) - 7(2, 6)$	257.0999657	35	48	1.22×10^{-4}	this work	~ 10
$J(K_a, K_b) = 9(3, 7) - 9(2, 8)$	258.9421992	51	63	1.32×10^{-4}	this work	~ 9
$J(K_a, K_b) = 7(2, 6) - 6(1, 5)$	271.5290139	22	35	1.11×10^{-4}	this work	~ 9
CCCS						
$J = 15 - 14$	86.708379	29	33	5.04×10^{-5}	Colzi et al. (2018)	~ 29
$J = 16 - 15$	92.488490	33	38	6.13×10^{-5}	Fontani et al. (2015b)	~ 27
o-H ₂ CS						
$J(K_a, K_b) = 8(1, 8) - 7(1, 7)$	270.521931	59	72	2.90×10^{-4}	this work	~ 9

Notes. For CCS, H₂S, CCCS, and SO₂, only the transitions with $E_u \leq 100$ K are listed; ^(a) All parameters are taken from the CDMS catalogue (Endres et al. 2016), except that for SO⁺, for which we use the Jet Propulsory Laboratory (JPL) catalogue (Pickett et al. 1998); ^(b) Reference paper where the observations are presented; ^(c) Beam size; ^(d) we list only the two strongest hyperfine components.

Table 3. Spectral line parameters of the NO molecule

line	ν_0 GHz	E_l K	E_u K	A_{ul} s^{-1}	Ref. ^a	θ_{MB} ^b
NO						
$J = 5/2 - 3/2, \Omega = 1/2, F = 7/2 - 5/2$	250.796436	7.2	19.3	1.85×10^{-6}	this work	~ 10
$J = 5/2 - 3/2, \Omega = 1/2, F = 5/2 - 3/2$	250.815594	7	19	1.55×10^{-6}	this work	~ 10

Notes. All parameters are taken from the CDMS catalogue (Endres et al. 2016). ^(a) Reference paper where the observations are presented; ^(b) Beam size;

cloud south of 23385 detected in interferometer images (Fontani et al. 2004). Only the main component at the systemic velocity of -49.5 km s^{-1} has been analysed in the following.

(ii) *the UCHII G75*: the SO $J(K) = 2(2) - 1(1)$ line is overestimated by the LTE fit. In Fig. 1 we show the best fit to the SO lines considering one and two Gaussian components. The fit with only one Gaussian provides a FWHM of $\sim 6.2 \text{ km s}^{-1}$, and there is a clear residual in the high velocity wings. The fit with two Gaussian components provides FWHM of $\sim 4.2 \text{ km s}^{-1}$ and $\sim 9.6 \text{ km s}^{-1}$, and the profile is better fitted in the wings. Similarly, assuming two Gaussian components improves the fit of the SO₂ $J(K_a, K_b) = 11(1, 11) - 10(0, 10)$ line in G75 and also in NGC7538, but worsens that of the other lines. However, the column density of the most intense component of the 2-Gaussian method is smaller but comparable within the errors as the one obtained with one component only. Therefore, in summary, in the sources in which some lines are under- or overestimated by the fit in LTE with a single Gaussian component there is likely a mix of non-LTE effects and multiple velocity features. Because the relative effect of both features is not easy to estimate, we will adopt the results obtained from the best-fit LTE approach using a single Gaussian component, except when an alternative approach improves significantly (i.e. difference larger than the uncertainties) the residuals.

Finally, the OCS $J = 22 - 21$ line is often contaminated by the broad high-velocity red wing of HCO⁺ $J = 3 - 2$ at 267557.6259 MHz. Therefore, we have simultaneously fit OCS and HCO⁺ to properly derive the OCS best fit in the sources with clear contamination.

3. Results

The spectra of the lines listed in Tables 2 and 3, as well as their best fit obtained with MADCUBA (Sect. 2.3), are shown in Figures A.1 - A.21 in Appendix A. For the species with more than three lines detected, e.g. SO, CCS, and SO₂, we show only the most intense ones.

3.1. Line profiles

The best fit results for all sources and all molecular species are reported in Appendix B. Tables B.1 and B.2 show the best fit radial centroid velocities, and tables B.3 and B.4 list the best fit line widths at half maximum. Both parameters have been obtained with MADCUBA as described in Sect. 2.3.

In most cases, the lines are very well fit with a single Gaussian. This is especially apparent in ¹³CS, C³⁴S, SO⁺, NS, CCS, HCS⁺, CCCS, and NO. The transitions detected in this work have upper level energies up to $\sim 40 \text{ K}$ (Table 2), suggesting that they likely trace relatively cold material. Their spectral shapes confirm, overall, this interpretation, even though in some sources clear high-velocity wings are present: the warm HMSC AFGLA,

and the two HII regions G75 and NGC7538. The transitions that are likely associated with shocked or warmer gas are those of SO, OCS, p-H₂S, and SO₂. In fact, their upper level energies are higher than 40 K, and they show often high-velocity wings. These wings are clearly present in the three sources already mentioned, and also towards: the warm HMSC 05358a, the HMPOs 05358b, 18517, and 23385, and all UCHII regions except 22134. The SO⁺, NS, and NO transitions do not show high-velocity wings, however their signal-to-noise ratios are on average much lower than those of the transitions discussed above, and hence the lack of these wings can be due to the limited sensitivity.

Figures 2 – 4 show the comparison between the FWHM of the lines obtained with MADCUBA as explained in Sect. 2.3. Among all possible combinations, we have chosen ¹³CS as reference species being the best tracer of quiescent gas (Fig. 2). We also investigate correlations with HCS⁺ and CCS, which both have a temperature estimate. Such comparisons allow us to understand the species that are more likely associated with similar gas, and to check for significant variations among the different lines/species.

Figure 2 indicates that the FWHMs of the ¹³CS lines are positively correlated with those of almost all species, except CCCS. The correlation is perfect with C³⁴S (Pearson's ρ correlation coefficient 0.99), good with HCS⁺, SO, NO, CCS, and SO⁺ ($\rho \sim 0.81 - 0.92$), and faint with H₂CS, NS, H₂S, OCS, and SO₂ ($\rho \sim 0.29 - 0.64$). Clearly, the ¹³CS, C³⁴S, and HCS⁺ observed transitions trace the same gas, based on their correlations and on the almost identical range of FWHMs measured. This is consistent with the fact that these species are all strictly chemically related to CS, and the observed transitions have the same quantum numbers (except for HCS⁺ $J = 6 - 5$). CCS is also tightly correlated with ¹³CS, and in all these species (C³⁴S, ¹³CS, HCS⁺, and CCS), the FWHM never exceeds $\sim 5 \text{ km s}^{-1}$, indicating that they are all associated with relatively quiescent material.

Interestingly, the FWHMs derived from NS are narrower than those of ¹³CS except than in two UCHII regions, perhaps indicating that NS tends to trace the most quiescent and extended material in the less evolved stages. There is a very good positive correlation also with SO ($\rho = 0.92$), but SO lines have systematically larger FWHM. This suggests that the SO emission is affected by a warmer, denser, and more turbulent component, for example associated with outflow cavities, which likely adds to the quiescent component. Indeed, high-velocity non-Gaussian wings in SO are found towards HMPOs and UCHIIs, while in cold HMSCs only the quiescent component is detected. The FWHMs of the other O-bearing molecules, namely SO⁺, OCS, and SO₂, are systematically larger than those of ¹³CS as well. This, and the additional evidence of hints of non-Gaussian wings in the spectra of OCS and SO₂ (see Figs. A.14, A.15, A.17, A.18), indicate that these species trace more turbulent material. The nature of the SO⁺ emission is not

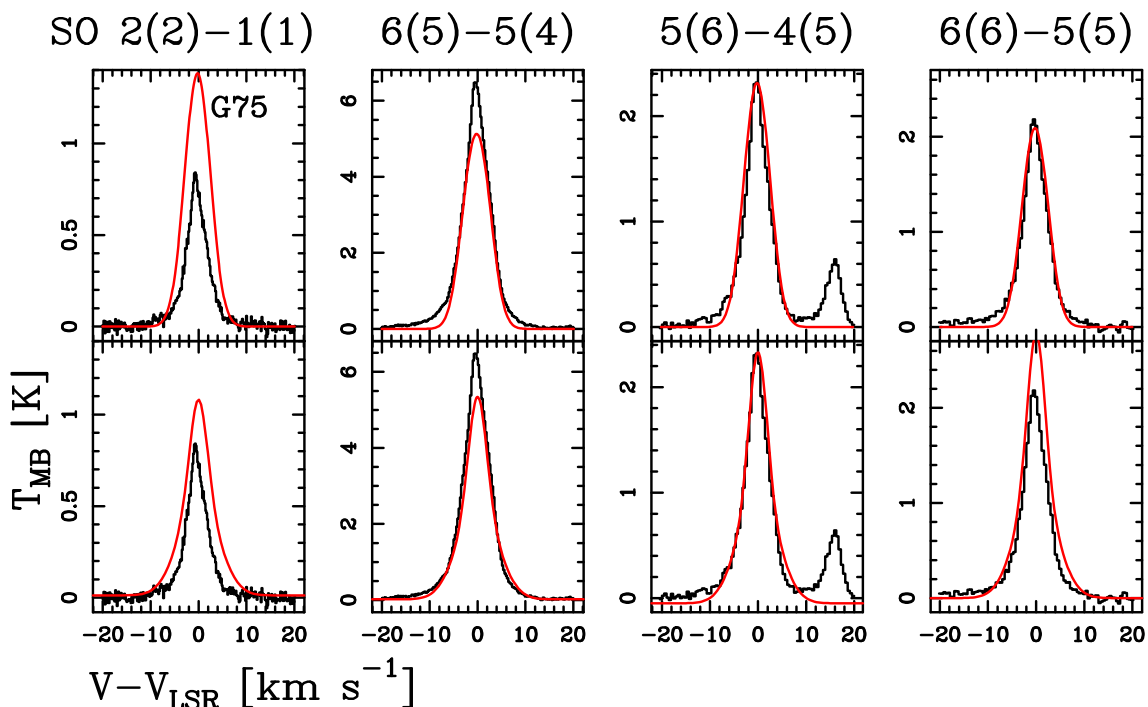


Fig. 1. Best fit to the SO lines towards the UCHII G75. On the x-axis we show the velocity shift from the systemic velocity V_{LSR} listed in Table 1. The red curves superimposed on the observed spectrum (in black) represent the best fit with one Gaussian component in the upper panels, and with two Gaussian components in the lower panels.

easy to determine: its FWHMs are well correlated with those of ^{13}CS , but, like SO, are systematically larger. Hence, they could contain both a quiescent and a turbulent component like SO. However, the lines do not show clear hints of non-Gaussian wings. This could be due to the fact that the SO^+ lines are fainter, and hence the lower signal-to-noise ratio in the spectra prevents us to detect the high-velocity emission in the wings

About NO, this molecule is found to be associated with both envelope material and outflow cavities in low-mass star-forming cores (Codella et al. 2018). In Fig. 2 (see also Table B.4) one can see that the FWHMs of NO are smaller than those of SO, indicating that the emission from the envelope component is dominant in our NO lines. This is further supported by the lack of non-Gaussian wings in the spectra (see Fig. A.21), and it is consistent with the larger range in E_u of the SO lines with respect to the NO ones (19–100 K against 19 K, Tables 2 and 3).

Figures 3 and 4 show the comparison between the lines FWHM of HCS^+ and CCS and those of the other tracers. The FWHMs of HCS^+ correlate very well with those of C^{34}S , SO, SO^+ , and NO ($\rho \geq 0.8$). However, the relations closest to a $y=x$ relation are found with C^{34}S and NO, while SO and SO^+ have larger FWHMs. Those of CCS (Fig. 4) correlates well ($\rho \geq 0.8$) only with SO^+ and C^{34}S , but the range of values indicate that SO^+ is associated with more turbulent material, as for HCS^+ . In summary, the lines of the C- and N-bearing species tend to trace the most quiescent, and probably extended, envelope of the sources. In particular NS seems associated with the most quiescent gas in early sources, and then ^{13}CS , C^{34}S , HCS^+ , and CCS trace a similar, but maybe slightly inner, envelope. The O-bearing species are associated with more turbulent, and thus likely inner, regions of the cores based both on the larger FWHMs and on the presence of non-Gaussian wings in evolved objects. Among these molecules, NO seems to trace the outermost layers, then SO and SO^+ arise from slightly more turbulent inner regions, and finally OCS and SO_2 from the most turbu-

lent inner regions. The origin of o- H_2CS , p- H_2S , and CCCS is very source-dependent, but while the o- H_2CS and p- H_2S lines show hints of non-Gaussian high velocity wings in some targets (05358a, 05358b, 23385, 18517, G75, NGC7538), the CCCS lines are always Gaussian and hence likely associated uniquely with an envelope component.

3.2. Excitation temperatures and total column densities

The excitation temperatures, T_{ex} , of the molecules listed in Tables 2 and 3 are shown in Table B.5. The molecular total column densities are listed in Tables B.6 and B.7. They have been derived assuming LTE conditions as described in Sect. 2.3. T_{ex} were derived from MADCUBA as explained in Sect. 2.3 for the five species for which we detected at least two transitions with different energies, namely SO, CCS, HCS^+ , OCS, and SO_2 . For the species for which we have only one transition, that is ^{13}CS , C^{34}S , p- H_2S , o- H_2CS , and CCCS, or multiple transitions with too similar energies of the levels (i.e. SO^+ , NS, and NO), we had to fix T_{ex} to compute N_{tot} . The T_{ex} adopted is discussed below.

In Figure 5 we investigate correlations between each pair of measured excitation temperatures. As done for the FWHMs, we make a quantitative analysis computing the Pearson's ρ correlation coefficients. A clear positive correlation is found only between SO and SO_2 ($\rho = 0.78$), even though the trend is strongly influenced by one source only. Fainter, still positive correlations are found between HCS^+ and CCS, HCS^+ and SO, SO and CCS. Negative correlations are found between HCS^+ and OCS, and CCS and OCS. The tracers associated with gas having temperature lower than ~ 30 K are HCS^+ and CCS. The molecule SO also traces relatively cold gas because its T_{ex} is between $\sim 10 - 33$ K, except for the UCHII region NGC7538, for which T_{ex} from SO is ~ 50 K. This source is also responsible for the positive correlation between SO and SO_2 , which would be not significant without it ($\rho \sim 0.14$), and it is hence likely an out-

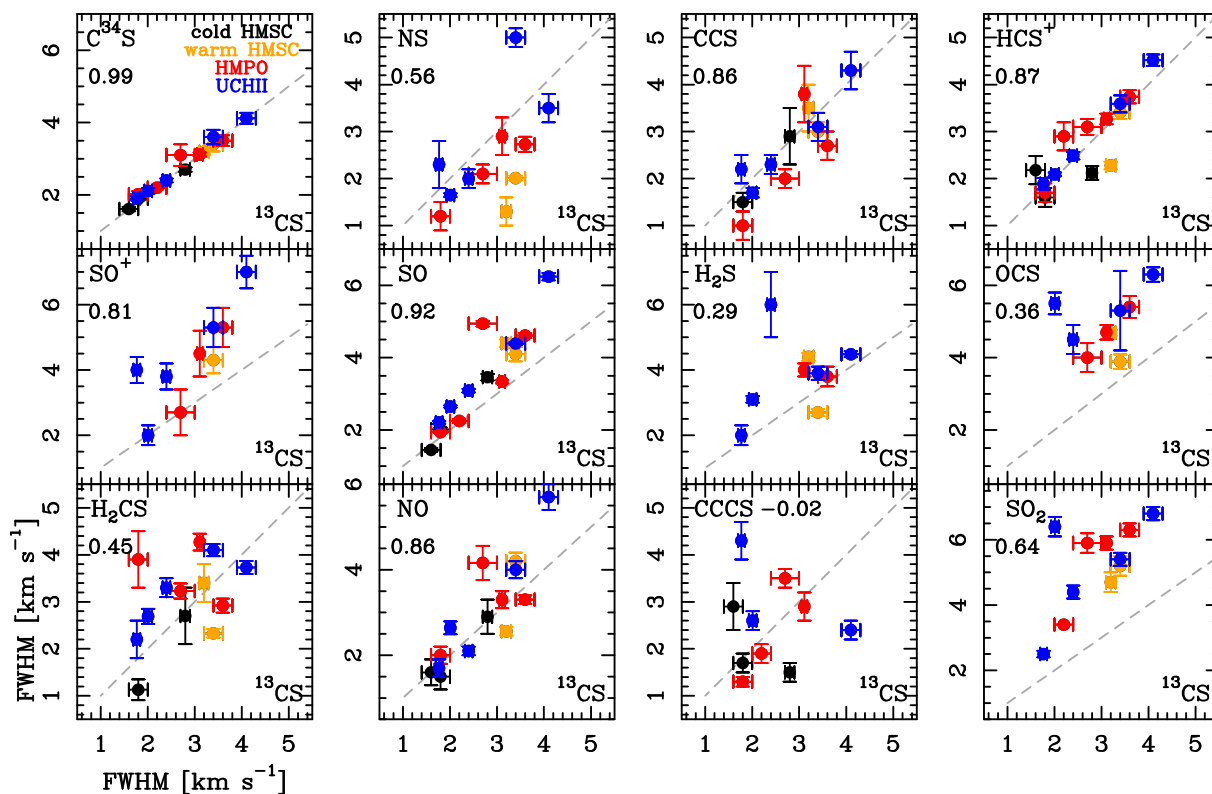


Fig. 2. Comparison between the lines FWHMs of the observed species and those of ^{13}CS . In all plots, the black points indicate the cold HMSCs, the orange ones the two warm HMSCs, the red ones the HMPOs, and the blue ones the UCHII regions. The dashed grey line indicates the locus $y=x$. The number in the upper left corner of each panel is the Pearson's ρ correlation coefficient.

lier. The tracers that are clearly associated with material warmer than ~ 40 K are SO_2 and OCS , both having temperature above 45 K. All this is consistent with the previous suggestion based on the lines FWHMs that the lines of the C-bearing species trace a colder extended envelope, SO maybe a denser and more compact but still relatively cold region, and OCS and SO_2 the warmer and likely innermost regions.

The correlations between the FWHM of the lines shown in Figs. 2 – 4 allow us to determine which species are most likely arising from similar gas, and hence to assign to the molecules for which we do not have a direct T_{ex} estimate the best representative one. Fig. 3 shows that ^{13}CS , C^{34}S , NS , and $\text{o-H}_2\text{CS}$, have a good positive correlation with the FWHM of HCS^+ , and a similar velocity range. Hence, we have fixed T_{ex} from that of HCS^+ to derive the column density of these species. Among the O-bearing species, the molecule NO shows the best positive correlation with HCS^+ ($\rho = 0.90$). However, we have computed the correlation also with SO , and found a similar coefficient ($\rho = 0.91$). Therefore, due to the fact that NO and SO are oxygen-containing species while HCS^+ is not, we have computed the NO column density fixing T_{ex} to that of SO . The FWHM of SO^+ also shows the best positive correlation with HCS^+ ($\rho = 0.8$), but because of the fair correlation coefficient with SO ($\rho = 0.65$), the similar range of FWHMs measured, and their chemical relation, we adopted T_{ex} from SO to compute the SO^+ column density. The molecule $\text{p-H}_2\text{S}$ does not show a compelling correlation with any of the tracers inspected. We thus decided to adopt T_{ex} from SO because it is the most accurate estimate, owing to the large number of transitions with relatively wide energy range ($E_{\text{u}} = 19 - 56$ K) on which it is based. For CCCS we do not have correlation with any tracer, and the dispersions are similar. We

have used T_{ex} from HCS^+ to be consistent with other C-only-bearing species.

For undetected species, an upper limit on N_{tot} has been evaluated fixing FWHM and T_{ex} to those of the species that likely trace similar gas. For example, for OCS and SO_2 we have used FWHM and T_{ex} from SO . Fixing FWHM and T_{ex} in this way, we have computed the upper limit on N_{tot} simulating Gaussian lines below an intensity peak of $\sim 3\sigma$ rms.

3.3. Molecular fractional abundances

From the molecular column densities in Tables B.6 and B.7, we computed the fractional abundances, X , dividing them by the H_2 total column densities, $N(\text{H}_2)$, given in Fontani et al. (2018). These are average values within an angular beam of $28''$. Because the total column densities have been estimated assuming that the emission is more extended than the beam, the abundances are hence average values within $28''$. They are given in Tables 4 and 5.

We have checked if the correlations, and tentative correlations, found based on the FWHMs with ^{13}CS (Fig. 2) are also apparent in the fractional abundances. We performed the same check with the abundances of SO as reference species for the abundances of O-bearing molecules. The comparison with ^{13}CS and SO are shown in Figures 6 and 7, respectively. Let us consider first ^{13}CS (Fig. 6). The clear correlations already found with C^{34}S , SO , HCS^+ , and NO based on the FWHMs are confirmed between the abundances of such species and that of ^{13}CS . Among the other species, we find a positive correlation of $X[^{13}\text{CS}]$ with $X[\text{NS}]$, $X[\text{SO}^+]$, $X[\text{p-H}_2\text{S}]$, $X[\text{SO}_2]$, $X[\text{OCS}]$, and $X[\text{o-H}_2\text{CS}]$. We stress, however, that these trends consider only the detected sources and do not include the upper limits. Hence,

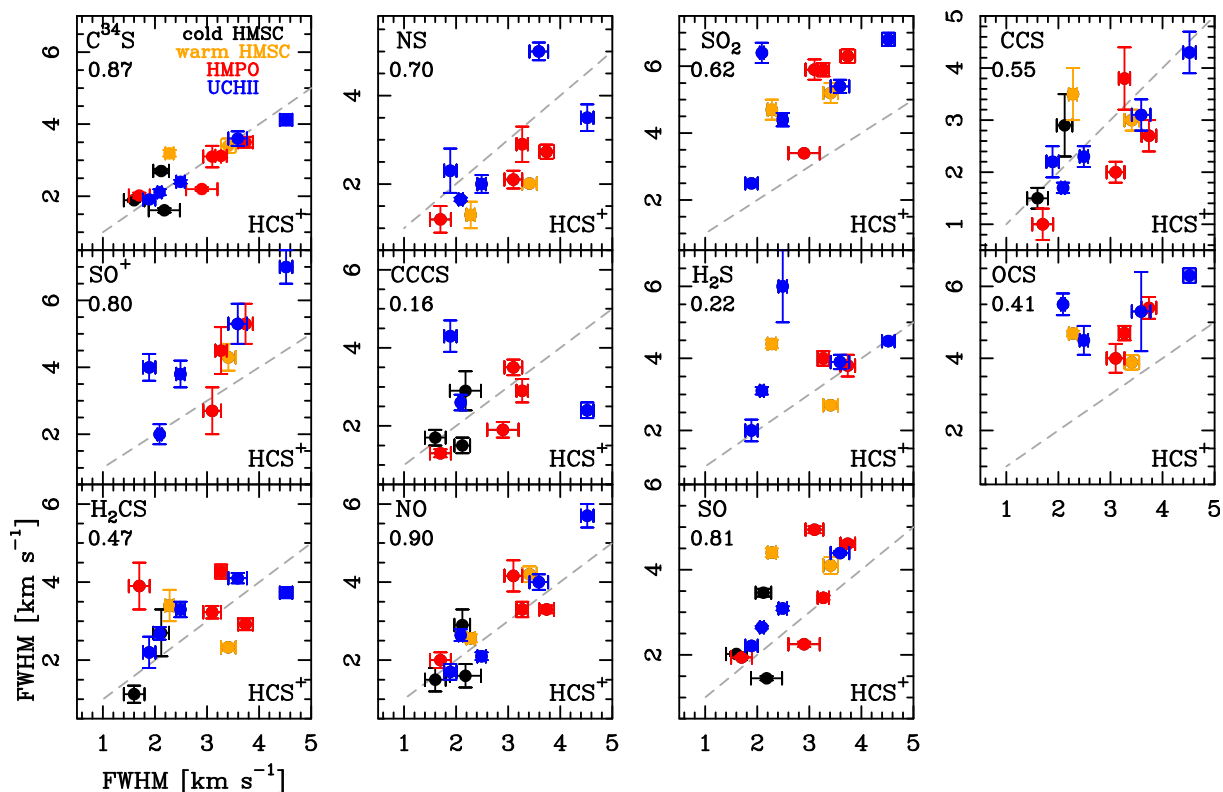


Fig. 3. Same as Fig. 2, but using HCS⁺ as reference species. The comparison with ¹³CS is shown already in Fig. 2.

they must be taken with caution. Moreover, the strong correlations with OCS, p-H₂S, and SO₂, are influenced mostly by the UCHII G75. These correlations are less strong ($\rho \leq 0.5$) excluding this target, while those with C³⁴S, SO, HCS⁺, NO, and o-H₂CS remain strong even excluding G75 from the statistical analysis. A very poor correlation ($\rho \leq 0.4$) is found with CCS, and no correlation is found with CCCS, like in the FWHMs.

As for the correlations with the SO fractional abundances (Fig. 7), we find positive correlations with ¹³CS, C³⁴S, HCS⁺, NO, but also with o-H₂CS, p-H₂S, SO⁺, and OCS, that confirms the double origin of SO in both quiescent and turbulent material. SO is also positively correlated with NS and SO₂, but the trend is determined mostly by one source only, that is again the UCHII region G75, as for ¹³CS. No correlation between SO and CCS or CCCS is found. As for ¹³CS, we stress that for some molecules the correlation coefficient is calculated without the upper limits (i.e. NS, SO⁺, p-H₂S, OCS, SO₂, and o-H₂CS), and hence they should be considered with caution.

4. Discussion

4.1. Chemistry of the tracers with correlated physical parameters

Based on the FWHMs, the T_{ex} , and the molecular fractional abundances we have found correlations between some tracers. Let us discuss here the possible chemical reasons of these correlations. We base our discussion on the chemical network of Shingledecker et al. (2020).

First, we note the perfect correlation in both FWHMs and abundances between ¹³CS and C³⁴S that shows a common origin for the two isotopologues, independent of either evolution and source physical properties. In particular, the correlation of the abundances also implies that fractionation effects of both carbon

and sulphur are irrelevant. We will discuss better this point in Sect. 4.4. The relation between both CS isotopologues and HCS⁺ points to a ion-molecule schema for the formation of CS where dissociative recombination of HCS⁺ leads to CS. Formation of HCS⁺ may occur via both:



and



where CS⁺ results from SO + C⁺, and/or CH + S⁺ reactions, and charge transfer between CS and H⁺. CS may also be formed through neutral-neutral reaction pathways from the reactions O + CCS and C + SO that may stand for the FWHM correlations observed in Fig. 2 between ¹³CS and CCS, and ¹³CS and SO. The latter correlation is also observed between their abundances (Fig. 6). Also, because both CS isotopologues and SO have non-Gaussian high-velocity wings in the HMPO and UCHII stages (Figs. A.1, A.2, A.4, and A.5), they are likely both partially produced from grain sputtering in protostellar outflows in evolved sources.

NS is the molecule that is associated with the smallest FWHMs, except for the UCHII NGC7538. NS is produced starting from atomic S either on grain surfaces or in the gas via:



and destroyed mainly via:



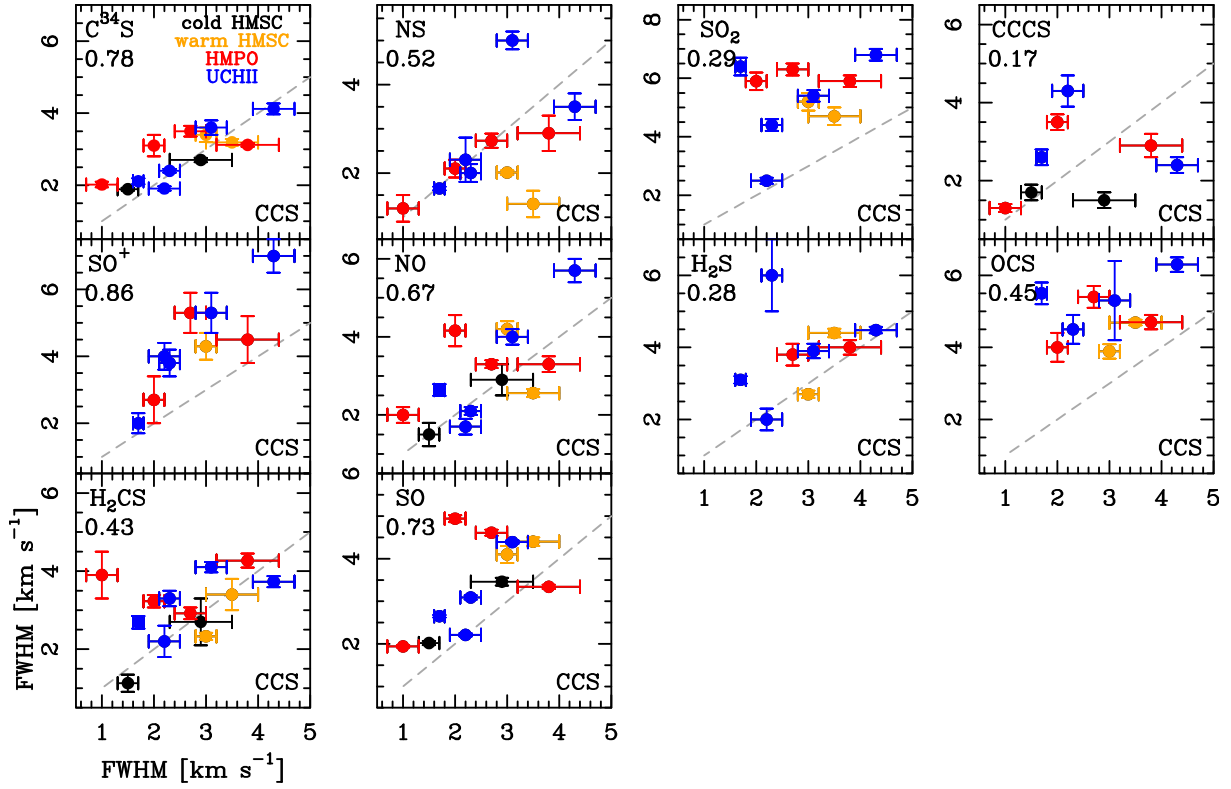


Fig. 4. Same as Fig. 2, but using CCS as reference species. The comparison with ^{13}CS and HCS^+ is shown already in Figs. 2 and 3, respectively.

Table 4. Abundances with respect to H_2 of the analysed diatomic molecules

source	^{13}CS	C^{34}S	SO	SO^+	NS	NO
HMSCs						
00117b	$6(3)\times 10^{-11}$	$2.0(0.7)\times 10^{-10}$	$1.1(0.4)\times 10^{-9}$	2.0×10^{-10}	$3.0(1.0)\times 10^{-11}$	$1.2(0.5)\times 10^{-8}$
AFGLa	$8(3)\times 10^{-11}$	$2.1(0.7)\times 10^{-10}$	$2.7(0.9)\times 10^{-9}$	1.1×10^{-10}	$2.1(1.4)\times 10^{-11}$	$1.3(0.4)\times 10^{-8}$
05358a	$7(2)\times 10^{-11}$	$1.7(0.5)\times 10^{-10}$	$1.3(4)\times 10^{-9}$	$7(2)\times 10^{-11}$	$1.8(0.4)\times 10^{-10}$	$8(2)\times 10^{-9}$
20293a	$3.0(0.9)\times 10^{-11}$	$8(2)\times 10^{-11}$	$3.0(0.9)\times 10^{-10}$	7×10^{-11}	7×10^{-12}	$3(1)\times 10^{-9}$
22134b	$3(2)\times 10^{-11}$	$1.0(0.3)\times 10^{-10}$	$6(2)\times 10^{-10}$	1.8×10^{-11}	4×10^{-11}	$8(4)\times 10^{-9}$
HMPOs						
00117a	$4.7(1.9)\times 10^{-11}$	$1.1(0.4)\times 10^{-10}$	$8(3)\times 10^{-10}$	1.9×10^{-10}	4.0×10^{-11}	$8(3)\times 10^{-9}$
05358b	$8(2)\times 10^{-11}$	$1.9(0.6)\times 10^{-10}$	$1.6(0.5)\times 10^{-9}$	$9(3)\times 10^{-11}$	$8(2)\times 10^{-11}$	$8(2)\times 10^{-9}$
18517	$1.1(0.2)\times 10^{-10}$	$2.5(0.4)\times 10^{-10}$	$2.3(0.4)\times 10^{-9}$	$1.7(0.5)\times 10^{-10}$	$1.0(0.2)\times 10^{-10}$	$1.4(0.3)\times 10^{-8}$
21307	$4.4(1.3)\times 10^{-11}$	$1.3(0.3)\times 10^{-10}$	$1.9(0.5)\times 10^{-9}$	1.9×10^{-10}	5.5×10^{-11}	8×10^{-9}
23385	$1.6(0.5)\times 10^{-10}$	$4.3(1.4)\times 10^{-10}$	$3.0(0.8)\times 10^{-9}$	$1.2(0.4)\times 10^{-10}$	$1.0(0.3)\times 10^{-10}$	$1.8(0.6)\times 10^{-8}$
UCHIIs						
G75	$3.5(1.0)\times 10^{-10}$	$8.0(2.0)\times 10^{-10}$	$1.4(0.4)\times 10^{-8}$	$5.3(1.6)\times 10^{-10}$	$2.3(0.7)\times 10^{-10}$	$3.3(1.0)\times 10^{-8}$
19410	$8(2)\times 10^{-11}$	$1.8(0.5)\times 10^{-10}$	$8(2)\times 10^{-10}$	$3.5(1.1)\times 10^{-11}$	$1.0(0.2)\times 10^{-10}$	$5.6(1.5)\times 10^{-9}$
22134	$1.0(0.3)\times 10^{-10}$	$2.9(0.8)\times 10^{-10}$	$2.1(0.6)\times 10^{-9}$	$6.3(1.7)\times 10^{-10}$	$5(2)\times 10^{-11}$	$1.0(0.3)\times 10^{-8}$
23033	$5.7(1.5)\times 10^{-11}$	$1.5(0.4)\times 10^{-10}$	$8(2)\times 10^{-10}$	$7(2)\times 10^{-11}$	$2.4(0.9)\times 10^{-11}$	$6.6(1.8)\times 10^{-9}$
NGC7538	$5.7(1.6)\times 10^{-11}$	$1.4(0.4)\times 10^{-10}$	$9(2)\times 10^{-10}$	$4.6(1.3)\times 10^{-11}$	$4.7(1.2)\times 10^{-11}$	$5.6(1.5)\times 10^{-9}$

Notes. The numbers in brackets are the uncertainties calculated according to the propagation of errors.

Therefore, the fact that NS is associated with very quiescent gas could be due to the destruction of NS by atomic oxygen in evolved stages. Atomic oxygen could be more abundant in these stages owing to photodissociation of water (see e.g. van Dishoeck et al. 2021). If so, a positive correlation between the abundances of NS and NO should be expected in evolved stages. In fact, we find a positive correlation between the two abundances ($\rho \sim 0.65$). We will discuss better this point in Sect. 4.2.

4.2. Abundances as a function of the evolutionary stage

We have searched for relations between the fractional abundances and the source parameters supposed to be evolutionary indicators, such as the gas kinetic temperature (T_k), the dust temperature (T_{dust}), the luminosity (L), and the luminosity-to-mass ratio (L/M). All parameters were derived from *Herschel* dust thermal emission measurements (Mininni et al. 2021), except for

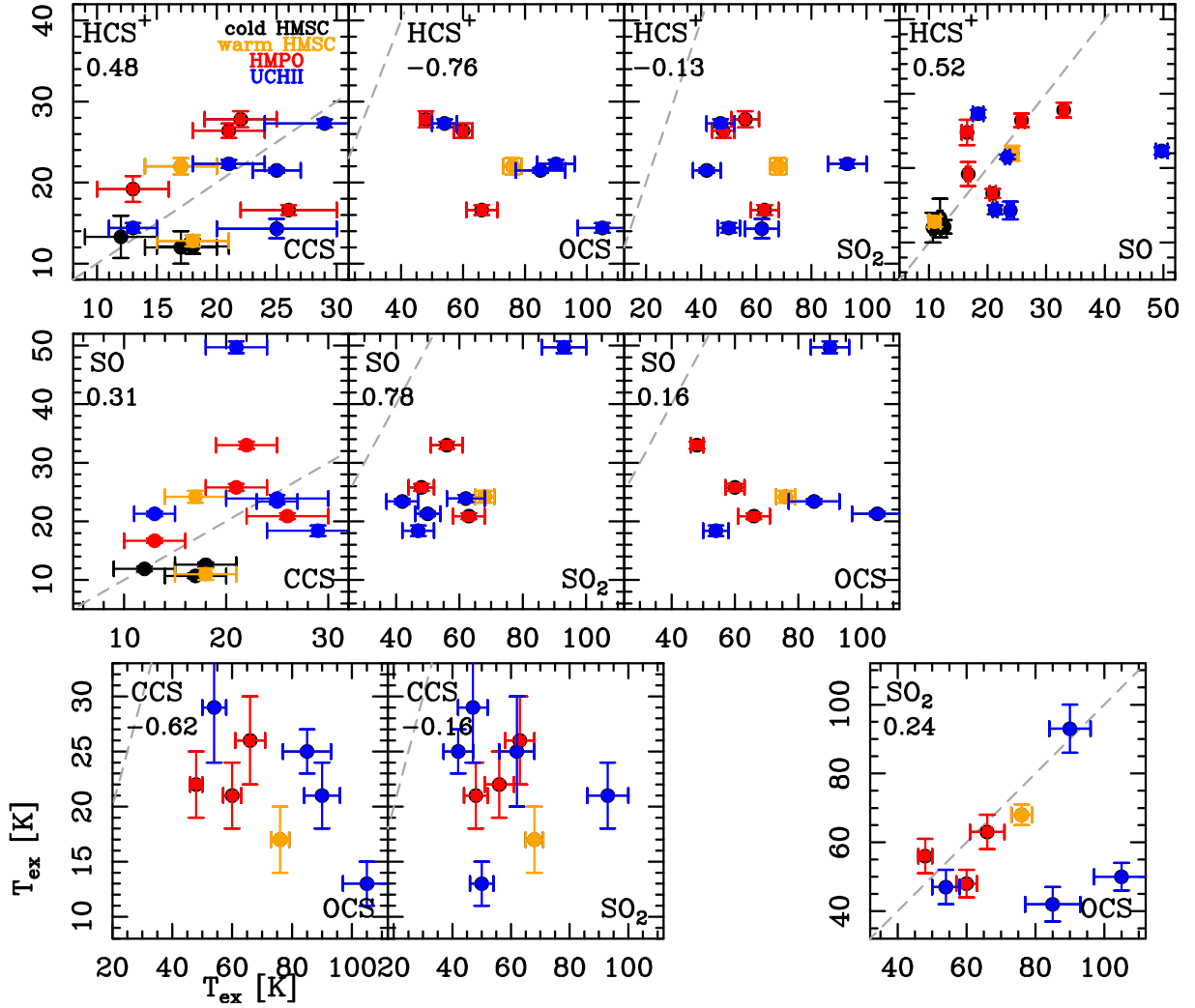


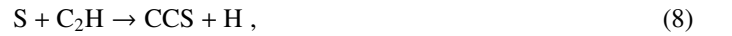
Fig. 5. Comparison between the excitation temperatures of the various molecules. In all plots, the black points indicate the cold HMSCs, the orange ones the two warm HMSCs, the red ones the HMPOs, and the blue ones the UCHII regions. The dashed grey line indicates the locus $y=x$.

T_k that was derived from ammonia observations (Fontani et al. 2011).

Molecular fractional abundances as a function of the gas kinetic temperature are shown in Fig. 8. All except those of CCS and CCCS are positively correlated with T_k . For each molecule, we computed the Pearson's ρ correlation coefficient and performed a linear regression fit to the data (plotted in logarithmic scale in Fig. 8). The strongest positive correlations are found for $C^{34}S$, ^{13}CS , HCS^+ , SO , SO_2 , and H_2S , having all $\rho \geq 0.9$, while the other tracers show a lower correlation. No significant correlation is found for CCS and CCCS. Plots of the abundances as a function of the other evolutionary indicators (T_{dust} , L , M/L) are shown in appendix C. We have grouped the sulphuretted molecules in C-only-bearing (Fig. C.1), CH-bearing (Fig. C.2), O-only-bearing (Fig. C.3), and others (Fig. C.4). The C-only-bearing species, namely $C^{34}S$, ^{13}CS , CCS, and CCCS, and the CH-bearing species HCS^+ and o- H_2CS , overall do not show obvious trends with the four evolutionary parameters except that with T_k . However, while $C^{34}S$, ^{13}CS , HCS^+ , and o- H_2CS show hints of an increasing trend with T_{dust} , L , and M/L , especially for $T_{dust} \geq 25$ K and $L \geq 10^3 L_\odot$, CCS and CCCS do not show any trend over the full temperature ($\sim 10 - 100$ K) and luminosity ($\sim 10^2 - 10^5 L_\odot$) ranges. Furthermore, CCCS is the only species

detected in all the cold HMSCs but not in the warm HMSCs (see Fig. A.19).

Both CCS and CCCS are thought to be gas-phase products mainly via:



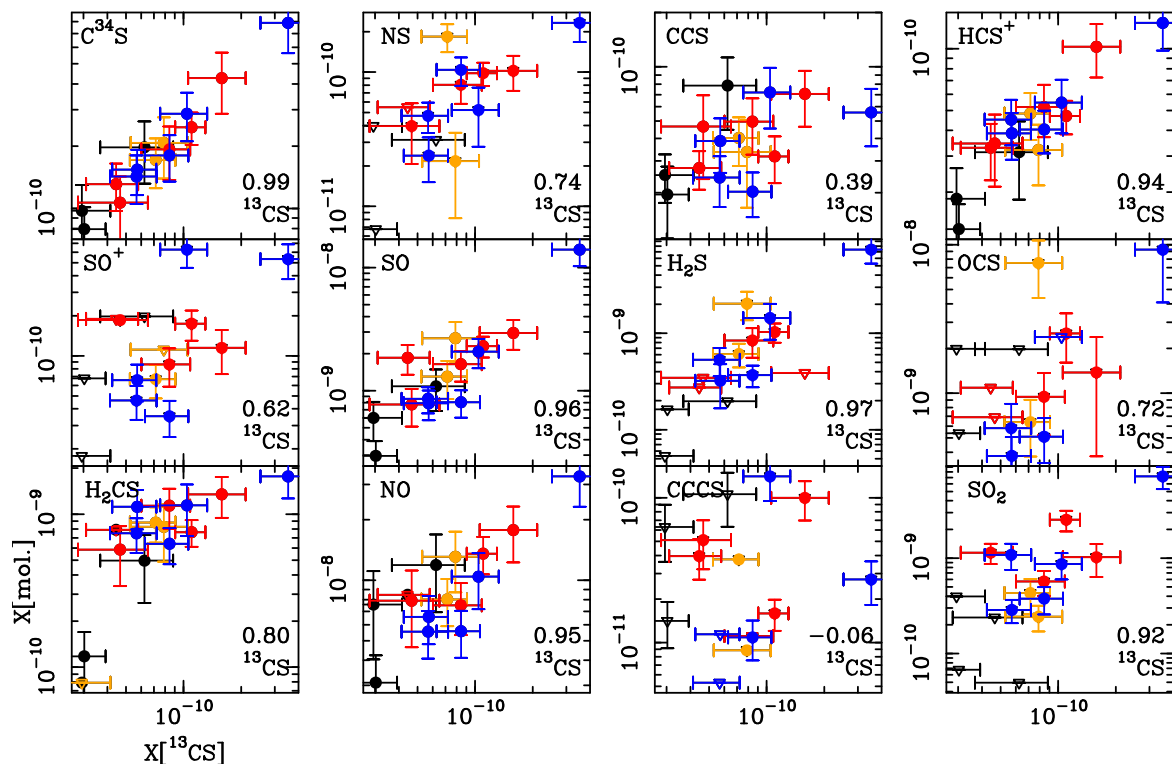


Fig. 6. Comparison between the fractional abundances of the observed species and that of ^{13}CS . In all plots, the black points indicate the cold HMSCs, the orange ones the two warm HMSCs, the red ones the HMPOs, and the blue ones the UCHII regions. The empty triangles are upper limits. The number in the lower-right corner of each panel is the Pearson's ρ correlation coefficient.



and the dissociative recombination reactions (Eq. 6, 7, and 10) are the dominant formation pathways for both CCS and CCCS. The main destruction channel of CCS is via reactions with atomic oxygen and nitrogen that give back CS, whereas CCCS does not react with atomic oxygen nor nitrogen as a consequence of the presence of a (small) barrier, as discussed in Vidal et al. (2017). If this barrier is overtaken in warm(er) environments, CCCS starts to be destroyed. This would explain the lower abundance in warm HMSCs than in cold HMSCs. Then, the fact that CCCS is present again at later stages could be due to a renewed efficient production, even though the non-detection in two UCHII again demonstrates an efficient destruction also in these later stages.

The abundances of the O-bearing species SO, SO^+ and SO_2 are overall positively correlated with T_{dust} , T_{k} , L , and M/L . The clearest trends are for SO and especially SO_2 , as both molecules show the best correlation with T_{k} (Fig. C.3). Finally, among the remaining species that are NS, OCS, and p- H_2S (Fig. C.4), the latter shows a clear increasing trend with all evolutionary parameters, in particular with T_{k} , while NS and OCS show less obvious trends. Both SO_2 and H_2S are well-known shock tracers, and our study indicates that they are evolutionary indicators for high-mass star-forming regions.

We have also computed the mean fractional abundances for each evolutionary stage. The results are shown in Fig. 9). In particular, for the HMSC group the mean has been computed separately for the cold sources (00117b, 20293a and 22134b) and the warm sources (AFGLa, 05358a). In some tracers, the cold HMSCs were both undetected: SO^+ , NS, p- H_2S , OCS, and

SO_2 . For these, we have computed the mean upper limit. The plot shows an increase of the mean abundances with the evolutionary stage in almost all molecules. However, the increase is different: (1) it jumps by about an order of magnitude from the cold HMSC group to the other groups for NS, p- H_2S , and o- H_2CS , and then stays almost constant; (2) it gradually increases through all stages in SO, SO^+ , and SO_2 ; (3) it increases by less than an order of magnitude from the cold HMSC group to the other groups for ^{13}CS and HCS^+ , and then stays almost constant; (4) it is (almost) constant in all groups for NO, OCS, and CCS (but OCS contains several upper limits).

Let us start with the molecules that show marginal or no enhancement. The negligible increase for ^{13}CS , NO, CCS, and HCS^+ is consistent with the fact that they are associated with extended material likely not affected, or marginally affected, by inner protostellar activity. However, OCS is thought to be produced in protostellar shocks, but because we only have upper limits in the cold HMSC group, the negligible enhancement could simply be due to the fact that these upper limits are too high with respect to the real abundances. About the species that show significant enhancement: the clear increase observed for SO, SO^+ , SO_2 , p- H_2S , and o- H_2CS indicates a favoured production of these species in warm gas and/or protostellar outflows. In particular, the gradual increase up to the UCHII phase of SO, SO^+ , and SO_2 , could be due to the increasingly larger abundance of atomic oxygen with evolution, owing to photodissociation of water in gas phase. In fact, low water abundances of $\sim 10^{-4}$ measured in protostellar environments (much lower than $\sim 4 \times 10^{-4}$ expected if all volatile oxygen is driven into water) were explained by strong UV radiation in shocks that dissociates water into O and OH (van Dishoeck et al. 2021; Tabone et al. 2021).

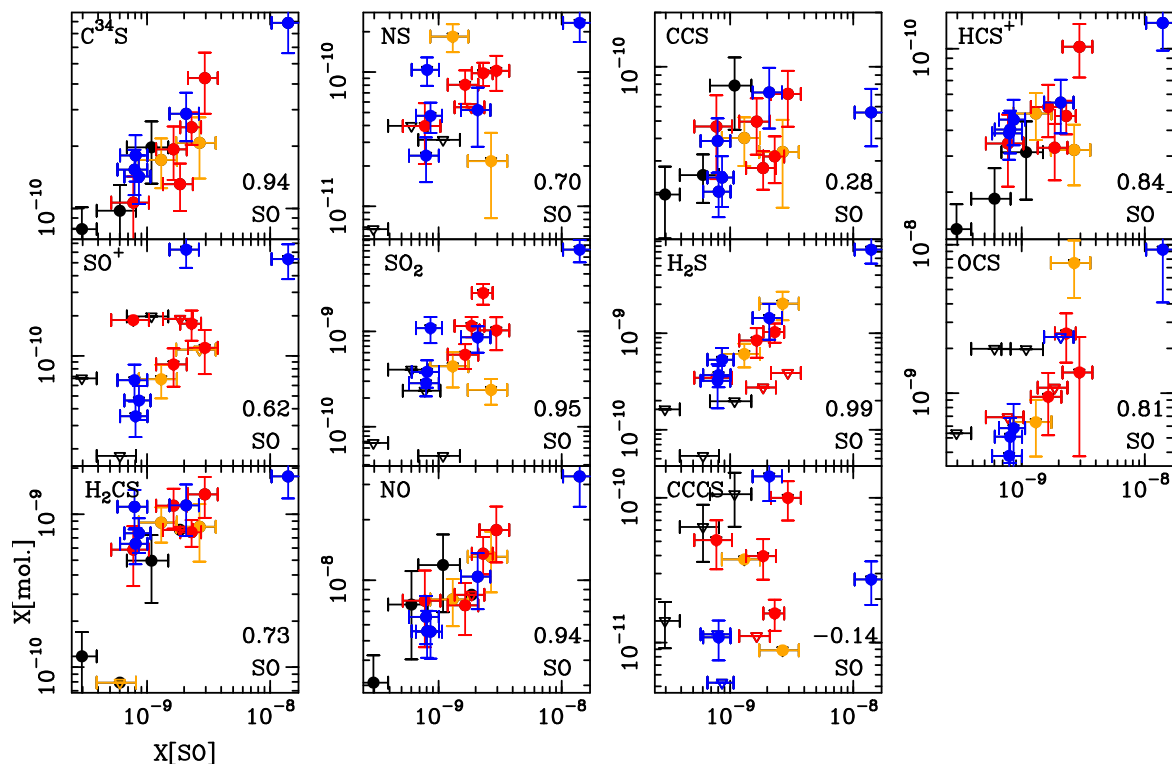


Fig. 7. Same as Fig. 6, but using SO as reference species. The comparison between SO and ^{13}CS is already shown in Fig. 6.

We summed the abundances of all S-bearing molecules to estimate the total budget of gaseous sulphur in each source. This sum, that we call $X_{\text{tot}}[\text{S}]$, is shown in Fig. 10. The *o*-H₂CS and *p*-H₂S abundances have been converted into the total ones assuming their LTE relative ratio of 3/4 and 1/4, respectively. The total abundance of CS has been computed multiplying the ^{13}CS abundance for the average local ISM carbon isotope ratio of 68 (Milam et al. 2005). We considered also the upper limits in the sum, and hence in each source $X_{\text{tot}}[\text{S}]$ is an upper limit to the total budget of gaseous sulphur, especially for the cold HMSCs that are associated with the highest number of upper limits. Despite this, the minimum average value is found towards the cold HMSCs, and the maximum enhancement of sulphur is found towards the UCHIIIs, that are the most evolved objects. The global increasing trend is likely due to the increasing amount of S sputtered from dust grains owing to the increasing protostellar activity with evolution. The largest $X_{\text{tot}}[\text{S}]$ is $\sim 10^{-7}$ found towards G75. Because the reference elemental abundance of atomic sulphur is 1.73×10^{-5} (Lodders 2003), still this maximum enhancement is lower by more than a factor 100 than the cosmic elemental abundance, in agreement with previous observational results and theoretical models (e.g. Esplugues et al. 2014, Fuente et al. 2016).

4.3. Abundance ratios as a function of the evolutionary stage

Previous works suggest that some abundance ratios between S-bearing species depend on the temperature of the host core. Herpin et al. (2009) studied two infrared (IR) dark and two IR bright high-mass dense cores in several sulphur-bearing molecules, and found that the SO/CS ratio increases from the IR dark to the IR bright objects, owing to an increase of the SO abundance. On the other hand, el Akel et al. (2022) find that the SO/CS ratio decreases from the cold envelope of intermediate-mass proto-

stars to warmer inner regions. Our observed SO/CS ratios are shown in Fig. 11. The ratio is the lowest in cold HMSCs, and then slightly increases in the later stages, in agreement with the study of Herpin et al. (2009). Other ratios claimed to increase with the evolutionary stage by Herpin et al. (2009) are H₂S/OCS and SO/SO₂, while CS/H₂S and OCS/SO₂ are found to decrease. As it can be seen from Fig. 11, the increasing trend for H₂S/OCS and the decreasing trends for CS/H₂S and OCS/SO₂ are confirmed in our sources.

The SO/SO₂ ratio was proposed by Wakelam et al. (2011) to decrease with time in massive cores. Our observations show a decrease by a factor 3-6 from the HMSCs to the later stages (Fig. 11). SO₂ can be produced on the surfaces of dust grains via oxygenation of SO, but also in the gas phase via (e.g. Vastel et al. 2018):



which is barrierless and favoured at high temperatures by the enhanced presence of OH in the gas, leading to a decrease in the SO/SO₂ ratio.

Finally, the NO/NS ratio can be seen as a proxy to the O/S elemental abundance ratio. As discussed in Sect. 4.2, the atomic abundance of both S and O is expected to increase with the evolutionary stage, as the enhancement of atomic S is due to dust grain evaporation and/or sputtering, and that of O to photodesorption and following photodissociation of water. We note that the NO/NS ratio is ~ 100 and constant in the evolved groups, while it is higher than 120 in the cold HMSCs. Fig. 9 indicates that this is mostly due to the lower abundance of NS in the cold HMSCs, as the abundance of NO is relatively constant in all evolutionary groups. This may be due to a higher depletion of S with respect to O in the early stages. Eq.(5) indicates that NS is destroyed by atomic O to form NO. However, this channel is a very

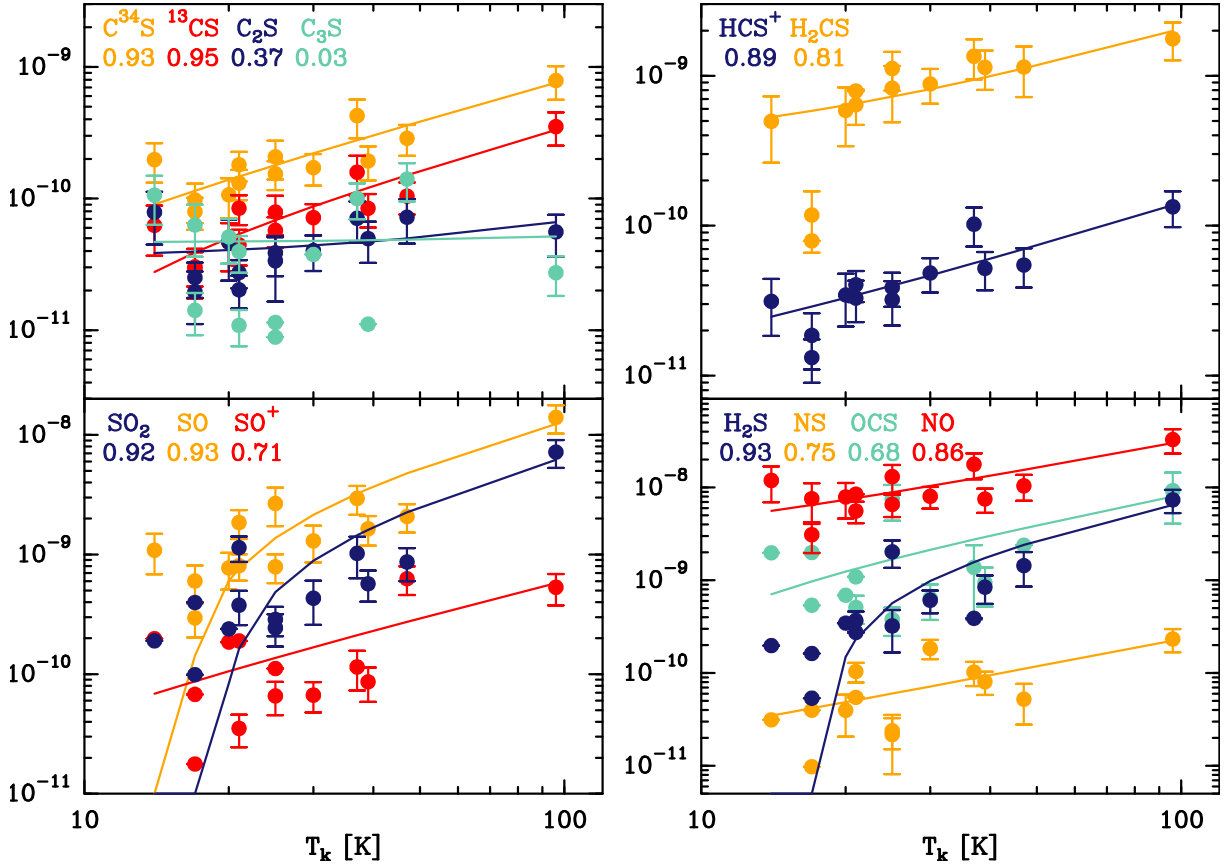


Fig. 8. Fractional abundances as a function of the kinetic temperature. T_k is derived from ammonia (Fontani et al. 2011). The four panels show sulphur-bearing molecules which contain: only carbon (top-left panel); carbon and hydrogen (top-right panel); only oxygen (bottom-left panel); anything else (bottom-right panel). The symbols without uncertainty are upper limits. The numbers below the label of each molecule is the Pearson's ρ correlation coefficient. The curves represent linear fits to the data including upper limits plotted in logarithmic scale.

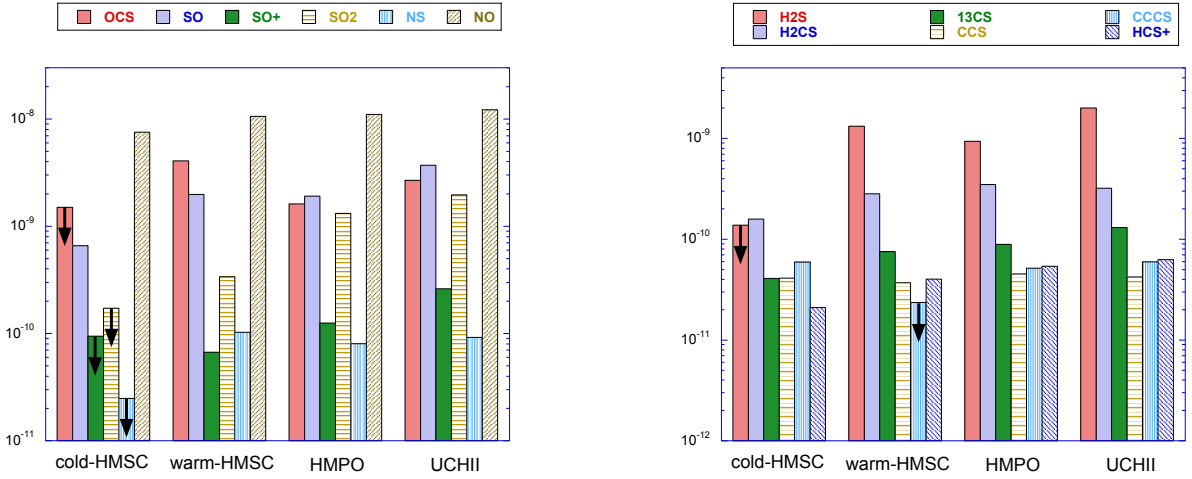


Fig. 9. Mean fractional abundances as a function of the evolutionary stage. Pointing-down arrows indicate mean upper limits. *Left panel:* measured mean abundances of S-bearing species containing oxygen and/or nitrogen. The sources are ordered from left to right according to their evolutionary stage (from HMSCs to UCHII). *Right panel:* same as the left panel for S-bearing species containing only carbon and/or hydrogen.

minor destruction mechanism of NO and has no impact on the NO/NS ratio.

Interestingly, the $SO/^{13}CS$ ratio below 13 in all evolutionary groups (see Fig. 11) indicates that the $SO/^{12}CS$ is smaller than

0.2 assuming the standard $^{12}C/^{13}C = 68$ ratio, consistent with carbon-rich environments.

Furthermore, the NO/NS ratio is ~ 100 and constant in the evolved groups, and higher than 120 in cold HMSCs. This points to a higher depletion of S with respect to O in this early stage,

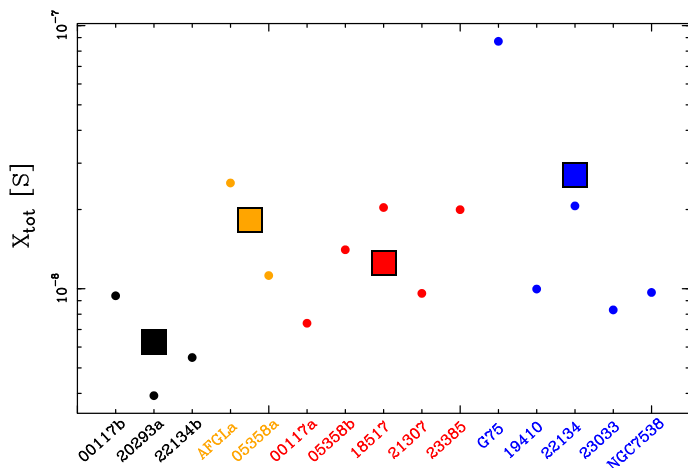


Fig. 10. Sum of the molecular fractional abundances in each source. The sources are indicated on the x-axis. The small symbols represent the total molecular abundances in each source, while the big symbols are the average values calculated in each group: cold HMSCs (in black); warm HMSCs (in orange); HMPOs (in red); UCHII (in blue).

and a similar relative abundance in the later stages. We stress, however, that care needs to be taken in the interpretation of these ratios, since the emission of the various molecules can arise from different regions inside the telescope beam.

4.4. Sulphur and carbon isotopic ratio

From ^{13}CS and C^{34}S $J = 2 - 1$, we have estimated the double isotopic ratio $^{34}\text{S}/^{32}\text{S} \times ^{12}\text{C}/^{13}\text{C}$. The reference Solar System values are $^{12}\text{C}/^{13}\text{C} \sim 89$, and $^{32}\text{S}/^{34}\text{S} \sim 22$ (Lodders 2003), so the reference Solar value is $^{34}\text{S}/^{32}\text{S} \times ^{12}\text{C}/^{13}\text{C} \sim 4$. The local interstellar medium (ISM) $^{12}\text{C}/^{13}\text{C}$ ratio derived from molecular data is ~ 68 (Milam et al. 2005), and hence in this case $^{34}\text{S}/^{32}\text{S} \times ^{12}\text{C}/^{13}\text{C}$ would be ~ 3 . The plot in Figure 11 shows the average column density ratio $\text{C}^{34}\text{S}/^{13}\text{CS}$ as a function of the evolutionary stage. The ratio is ~ 3 , consistent with the local ISM $^{34}\text{S}/^{32}\text{S} \times ^{12}\text{C}/^{13}\text{C}$ value. In particular, it decreases from ~ 3 to ~ 2.3 from the cold HMSCs to the warm HMSCs, and then it is almost constant in the later stages.

Fractionation processes for Sulphur are usually considered negligible in dense clouds especially in warm cores, as indicated by theoretical and observational works (Loison et al. 2019; Humire et al. 2020; Yan et al. 2023). On the other hand, the models of Colzi et al. (2020) predict that the $^{12}\text{C}/^{13}\text{C}$ ratio in CS can attain values up to a factor ~ 3 higher with respect to the local value in cold (~ 10 K) and dense ($2 \times 10^4 \text{ cm}^{-3}$) cores. Such physical parameters are appropriate for the gaseous envelope of quiescent HMSCs, in which the measured $\text{C}^{34}\text{S}/^{13}\text{CS}$ ratio is the highest. The constant trend in warm, later stages indicates that local carbon (and sulphur) fractionation processes are irrelevant at these stages in the emission regions probed by our observations.

5. Summary and conclusions

We analysed observations of S-containing molecules obtained with the IRAM 30m telescope towards 15 star-forming cores divided equally in the evolutionary stages HMSCs, HMPOs, and UCHII. The HMSCs are further divided into cold HMSCs and warm HMSCs, as already done in previous works. We have derived column densities assuming LTE conditions of SO, SO^+ ,

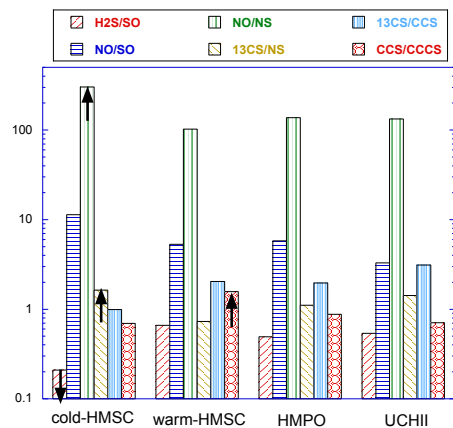
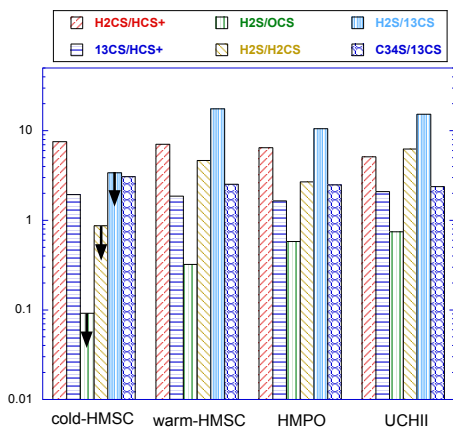
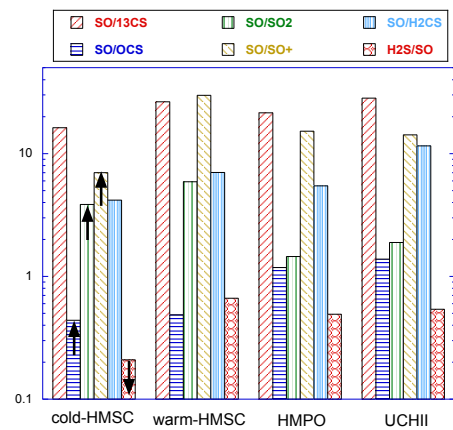


Fig. 11. Column density ratios as a function of the evolutionary stage. Arrows pointing upwards show lower limits. Arrows pointing downwards show upper limits.

NS, C^{34}S , ^{13}CS , SO_2 , CCS, H_2S , HCS^+ , OCS, H_2CS , and CCCS. We also analyse for the first time lines of the NO molecule to complement the analysis. For CCS, HCS^+ , SO, OCS, and SO_2 , we also derived the excitation temperatures. The line widths and excitation temperatures indicate that C^{34}S , ^{13}CS , CCS, HCS^+ , and NS trace preferentially quiescent and likely extended material, SO and maybe SO^+ both quiescent and turbulent material depending on the target, while OCS, and SO_2 trace warmer, more turbulent, and likely denser and more compact material.

The nature of the emission of the H₂S, H₂CS, and CCCS emission is less clear. We also found a global increasing trend of the total gaseous sulphur going from cold HMSCs to UCHIIIs. This is likely due to the increasing amount of S sputtered from dust grains owing to the increasing protostellar activity with evolution. Still, the maximum total abundance that we find is $\sim 10^{-7}$ towards the UCHII G75, which is two orders of magnitude lower than the elemental S abundance. The abundances that show the best positive correlations with the evolutionary indicators are those of SO and SO₂, and in general oxygen-bearing species have higher abundances in more evolved stages than carbon-bearing ones have, perhaps due to the larger availability of atomic oxygen with evolution produced by photodissociation of water. We confirm that the abundance ratios SO/CS, H₂S/OCS, CS/H₂S, and OCS/SO₂, claimed to be possible evolutionary indicators, are found to vary with the evolution also in our study. Interestingly, we find that the NO/NS ratio, which can be considered a proxy of the O/S abundance ratio, is higher in the HMSCs than in the other three groups, perhaps due to the higher S-depletion with respect to O in this early stage. Our observational work represents an observational test-bed for theoretical studies aimed at modelling the chemistry of sulphur during the evolution of high-mass star-forming cores, and need to be complemented by higher-angular resolution observations to overcome possible problems due to different filling factors.

Acknowledgements. We thank the anonymous Referee for their careful reading of the paper and their constructive comments. F.F. is grateful to the IRAM staff for their precious help during observations. L.C. acknowledges financial support through the Spanish grant PID2019-105552RB-C41 funded by MCIN/AEI/10.13039/501100011033. This work is based on observations carried out under project number 116-16 with the IRAM 30m telescope. IRAM is supported by INSU/CNRS (France), MPG (Germany) and IGN (Spain).

References

- Adams, F.C. 2010, *ARA&A*, 48, 47
 el Akel, M., Kristensen, L.E., Le Gal, R., van der Walt, S.J., Pitts, R.L., Dulieu, F. 2023, *A&A*, 659, A100
 Altwegg, K., Balsiger, H., Fuselier, S.A. 2019, *ARA&A*, 57, 113
 Anderson, D.E., Bergin, E.A., Maret, S., Wakelam, V. 2013, *ApJ*, 779, 141
 Asplund, M., Grevesse, N., Sauval, A.J., Scott, P. 2009, *ARA&A*, 47, 481
 Beuther, H., Zhang, Q., Bergin, E.A., Sridharan, T.K. 2009, *AJ*, 137, 406
 Boogert A.C.A., Gerakines P.A., Whittet D.C. B. 2015, *ARA&A*, 53, 541
 Calmonte, U., Altwegg, K.; Balsiger, H., et al. 2016, *MNRAS*, 462, 253
 Carpenter, J.M. 2000, *AJ*, 120, 3139
 Cazaux, S., Carrascosa, H., Muñoz Caro, G.M., Caselli, P., Fuente, A., Navarro-Almáida, D., Rivière-Marichalar, P. 2022, *A&A*, 657, A100
 Cernicharo, J., Cabezas, C., Agúndez, M. 2021, *A&A*, 648, L3
 Codella, C., Viti, S., Lefloch, B., et al. 2018, *MNRAS*, 474, 5694
 Coletta, A., Fontani, F., Rivilla, V.M., Mininni, C., Colzi, L., Sánchez-Monge, Á., Beltrán, M.T. 2020, *A&A*, 641, 54
 Colzi, L., Fontani, F., Caselli, P., Ceccarelli, C., Hily-Blant, P., Bizzocchi, L. 2018, *A&A*, 609, 129
 Colzi, L., Fontani, F., Caselli, P., Leurini, S., Bizzocchi, L., Quaia, G. 2019, *MNRAS*, 485, 5543
 Colzi, L., Sipilä, O., Roueff, E., Caselli, P., Fontani, F. 2020, *A&A*, 640, 51
 Drdla, K., Knapp, G.R. & van Dishoeck, E.F. 1989, *ApJ* 345, 815
 Endres, P., Schlemmer, S., Schilke, P., Stutzki, J., Müller, H.S.P. 2016, *J.Mol.Spec.*, 327, 95
 Esplugues, G.B., Viti, S., Goicoechea, J.R., Cernicharo, J. 2014, *A&A*, 567, 95
 Esplugues, G., Fuente, A., Navarro-Almáida, D., et al. 2022, *A&A*, 662, A52
 Esteban, C., Peimbert, M., García-Rojas, J., Ruiz, M.T., Peimbert, A., Rodríguez, M. 2004, *MNRAS*, 355, 229
 Evans, N.J.II, Dunham, M.M., Jørgensen, J. K., et al. 2009, *ApJS*, 181, 321
 Fontani, F., Cesaroni, R., Testi, L., et al. 2004, *A&A*, 414, 299
 Fontani, F., Pascucci, I., Caselli, P., Wyrowski, F., Cesaroni, R., Walmsley, C.M. 2007, *A&A*, 470, 639
 Fontani, F., Palau, Aina, Caselli, P., et al. 2011, *A&A*, 529, L7
 Fontani, F., Sakai, T., Furuya, K., Sakai, N., Aikawa, Y., Yamamoto, S. 2014, *MNRAS*, 440, 448
 Fontani, F., Caselli, P., Palau, Aina, Bizzocchi, L., Ceccarelli, C. 2015a, *ApJ*, 808, L46
 Fontani, F., Busquet, G., Palau, Aina, et al. 2015b, *A&A*, 575, 87
 Fontani, F., Barnes, A.T., Caselli, P., et al. 2021, *MNRAS*, 503, 4320
 Fontani, F., Vagnoli, A., Padovani, M., Colzi, L., Caselli, P., Rivilla, V.M. 2018, *MNRAS*, 481, L79
 Fontani, F., Colzi, L., Redaelli, E., Sipilä, O., Caselli, P. 2021, *A&A*, 651, 94
 Fuente, A., Cernicharo, J., Roueff, E., et al. 2016, *A&A*, 593, 94
 Fuente, A., Navarro, D.G., Caselli, P., et al. 2019, *A&A*, 624, A105
 Fuente, A., Rivière-Marichalar, P., Beitia-Antero, L., et al. 2023, *A&A*, 670, A114
 Goicoechea, J.R., Pety, J., Gerin, M., Teyssier, D., Roueff, E., Hily-Blant, P., Baek, S. 2006, *A&A* 456, 565
 Hatchell, J., Thompson, M.A., Millar, T.J., MacDonald, G.H. 1998, *A&A* 338, 713
 Herpin, F., Marseille, M., Wakelam, V., Bontemps, S., Lis, D.C. 2009, *A&A*, 504, 853
 Heyl, J., Sellentin, E., Holdship, J. and Viti, S. 2022, *MNRAS* 517, 38
 Hily-Blant, P., Pineau des Forêts, G., Faure, A., Lique, F. 2022, *A&A*, 658, A168
 Holdship, J., Jiménez-Serra, I., Viti, S., et al. 2019, *ApJ*, 878, 64
 Howk, J.C., Sembach, K.R., Savage, B.D. 2006, *ApJ*, 637, 333
 Humire, P.K., Thiel, V., Henkel, C., et al. 2020, *A&A*, 642, A222
 Jenkins, E.B. 2009, *ApJ*, 700, 1299
 Jiménez-Escobar A., Muñoz Caro G.M. 2011, *A&A*, 536, A91
 Kurtz, S., Cesaroni, R., Churchwell, E., Hofner, P., Walmsley, C.M. 2000, in *Protostars and Planets IV* (Book - Tucson: University of Arizona Press; eds Mannings, V., Boss, A.P., Russell, S. S.), p. 299-326
 Kutner, M.L., & Ulich, B.L. 1981, *ApJ*, 250, 341
 Laas, J. & Caselli, P. 2019, *A&A*, 624, A118
 Lodders, K. 2003, *ApJ*, 591, 1220L
 Loison, J.-C., Wakelam, V., Gratier, P., et al. 2019, *MNRAS*, 485, 5777
 Martín, S., Martín-Pintado, J., Blanco-Sánchez, C., et al. 2019, *A&A*, 631, 159
 McClure, M.K., Rocha, W.R.M., Pontoppidan, K.M., et al. 2023, *Nature Astronomy*, 7, 431
 McGuire, B.A. 2018, *ApJS*, 239, 17
 Milam, S.N., Savage, C., Brewster, M.A., Ziurys, L.M. 2005, *ApJ*, 634, 1126
 Millar, T. J., Adams, N. G., Smith, D., Lindinger, W. and Villinger, H. 1986, *MNRAS* 221, 673
 Mininni, C., Fontani, F., Rivilla, V.M., Beltrán, M.T., Caselli, P., Vasyunina, A. 2018, *MNRAS*, 476, L39
 Mininni, C., Fontani, F., Sánchez-Monge, A., Rivilla, V.M., Beltrán, M.T. 2021, *A&A*, 653, 87
 Navarro-Almáida, D., Le Gal, R., Fuente, A., et al. 2020, *A&A*, 637, A39
 Oppenheimer, M. & Dalgarno, A. 1974, *ApJ*, 187, 231
 Pickett, H.M., Poynter, R.L., Cohen, E.A., et al. 1998, *J. Quant. Spectr. Rad. Transf.*, 60, 883
 Pineau des Forêts, G., Roueff, E. & Flower, D.R., 1986, *MNRAS* 223, 743
 Pfalzner, S. 2013, *A&A*, 549, A82
 Rivilla, V.M., Beltrán, M.T., Cesaroni, R., Fontani, F., Codella, C., Zhang, Q. 2017, *A&A*, 598, 59
 Rivilla, V.M., Colzi, L., Fontani, et al. 2020a, *MNRAS*, 496, 1990
 Rivilla, V.M., Drozdovskaya, M. N.; Altwegg, K., et al. 2020b, *MNRAS*, 492, 1180
 Shingledecker, C.N., Lamberts, T., Laas, J.C., et al. 2020, *ApJ*, 888, 52
 Tabone, B., van Hemert, M.C., van Dishoeck, E.F., Black, J.H. 2021, *A&A*, 650, A192
 Taniguchi, K., Saito, M., Sridharan, T.K., Minamidani, T. 2018, *ApJ*, 854, 133
 Turner, B. 1995, *ApJ*, 455, 556
 van Dishoeck, E.F., Kristensen, L.E., Mottram, J.C., et al. 2021, *A&A*, 648, A24
 Vastel, C., Quénard, D., Le Gal, R., et al. 2018, *MNRAS*, 478, 5514
 Vasyunina, T., Linz, H., Henning, Th., Zinchenko, I., Beuther, H., Voronkov, M. 2011, *A&A*, 527, 88
 Vidal, T.H.G., Loison, J.-C., Jaziri, A.Y., Ruaud, M., Gratier, P., Wakelam, V. 2017, *MNRAS*, 469, 435
 Wakelam, V., Hersant, F., Herpin, F. 2011, *A&A*, 529, A112
 Wang, Y., Audard, M., Fontani, F., et al. 2016, *A&A*, 587, A69
 Woods, P.M., Occhiogrosso, A., Viti, S., Kaňuchová, Z., Palumbo, M.E., Price, S.D.
 Yan, Y.T., Henkel, C., Kobayashi, C., et al. 2023, *A&A*, 670, A98
 Zanchet, A., Agúndez, M., Herrero, V.J., et al. 2013, *AJ*, 146, 125

Table 5. Abundances with respect to H₂ of the molecules with three and four atoms

source	CCS	HCS ⁺	p-H ₂ S	OCS	SO ₂	CCCS	o-H ₂ CS
HMSCs							
00117b	8(3)×10 ⁻¹¹	3.1(1.3)×10 ⁻¹¹	2×10 ⁻¹⁰	2×10 ⁻⁹	5×10 ⁻¹¹	1.1(0.4)×10 ⁻¹⁰	5(2)×10 ⁻¹⁰
AFGLa	3.4(1.7)×10 ⁻¹¹	3.2(1.1)×10 ⁻¹¹	2.0(0.7)×10 ⁻⁹	7.5(3.2)×10 ⁻⁹	2.4(0.7)×10 ⁻¹⁰	0.9×10 ⁻¹¹	8.3(3.4)×10 ⁻¹⁰
05358a	4.0(1.2)×10 ⁻¹¹	4.8(1.2)×10 ⁻¹¹	6.1(1.7)×10 ⁻¹⁰	6.4(2.6)×10 ⁻¹⁰	4.3(1.7)×10 ⁻¹⁰	3.8×10 ⁻¹¹	8.8(2.3)×10 ⁻¹⁰
20293a	2.0(0.8)×10 ⁻¹¹	1.3(0.4)×10 ⁻¹¹	1.6×10 ⁻¹⁰	5.4×10 ⁻¹⁰	6.8×10 ⁻¹¹	1.4(0.5)×10 ⁻¹¹	1.2(0.5)×10 ⁻¹⁰
22134b	2.5×10 ⁻¹¹	1.9(0.8)×10 ⁻¹¹	5.4×10 ⁻¹¹	2.0×10 ⁻⁹	4.0×10 ⁻¹⁰	6.3(2.7)×10 ⁻¹¹	7.9×10 ⁻¹¹
HMPOs							
00117a	5(2)×10 ⁻¹¹	3.5(1.3)×10 ⁻¹¹	3.5×10 ⁻¹⁰	6.9×10 ⁻¹⁰	2.4×10 ⁻¹⁰	5.1(1.9)×10 ⁻¹¹	6(2)×10 ⁻¹⁰
05358b	5.0(1.7)×10 ⁻¹¹	5.2(1.5)×10 ⁻¹¹	8.4(2.9)×10 ⁻¹⁰	9.5(4.3)×10 ⁻¹⁰	5.7(1.7)×10 ⁻¹⁰	1.1×10 ⁻¹¹	1.1(0.3)×10 ⁻⁹
18517	3.2(0.9)×10 ⁻¹¹	4.7(0.9)×10 ⁻¹¹	1.0(0.2)×10 ⁻⁹	2.5(0.9)×10 ⁻⁹	2.5(0.6)×10 ⁻⁹	1.6(0.4)×10 ⁻¹¹	7.6(1.5)×10 ⁻¹⁰
21307	2.7×10 ⁻¹¹	3.3(1.0)×10 ⁻¹¹	2.7×10 ⁻¹⁰	1.1×10 ⁻⁹	1.1×10 ⁻⁹	4.0(1.2)×10 ⁻¹¹	7.9×10 ⁻¹⁰
23385	7.1(2.4)×10 ⁻¹¹	1.0(0.3)×10 ⁻¹⁰	3.9×10 ⁻¹⁰	1.4(1.0)×10 ⁻⁹	1.0(0.4)×10 ⁻⁹	1.0(0.3)×10 ⁻¹⁰	1.3(0.4)×10 ⁻⁹
UCHIIs							
G75	5.6(2.0)×10 ⁻¹¹	1.3(0.4)×10 ⁻¹⁰	7.4(2.1)×10 ⁻⁹	9.3(5.2)×10 ⁻⁹	7.2(1.9)×10 ⁻⁹	2.7(0.9)×10 ⁻¹¹	1.8(0.5)×10 ⁻⁹
19410	2.0(0.6)×10 ⁻¹¹	4.0(0.9)×10 ⁻¹¹	3.7(0.9)×10 ⁻¹⁰	5.1(1.7)×10 ⁻¹⁰	3.8(1.2)×10 ⁻¹⁰	1.1(0.3)×10 ⁻¹¹	6.4(1.7)×10 ⁻¹⁰
22134	7.2(2.7)×10 ⁻¹¹	5.5(1.6)×10 ⁻¹¹	1.4(0.6)×10 ⁻⁹	2.4×10 ⁻⁹	8.7(2.7)×10 ⁻¹⁰	1.4(0.5)×10 ⁻¹⁰	1.1(0.4)×10 ⁻⁹
23033	3.9(1.3)×10 ⁻¹¹	3.9(1.0)×10 ⁻¹¹	3.2(1.6)×10 ⁻¹⁰	3.8(1.3)×10 ⁻¹⁰	2.9(0.8)×10 ⁻¹⁰	1.1×10 ⁻¹¹	1.1(0.3)×10 ⁻⁹
NGC7538	2.4(0.8)×10 ⁻¹¹	4.5(1.1)×10 ⁻¹¹	5.3(1.7)×10 ⁻¹⁰	5.8(2.7)×10 ⁻¹⁰	1.1(0.3)×10 ⁻⁹	5.3×10 ⁻¹²	7.5(1.9)×10 ⁻¹⁰

Notes. The numbers in brackets are the uncertainties calculated according to the propagation of errors.

Appendix A: Spectra

In this appendix, we show the spectra of all molecular species analysed. For those having more than three transitions detected, we show only the brightest ones.

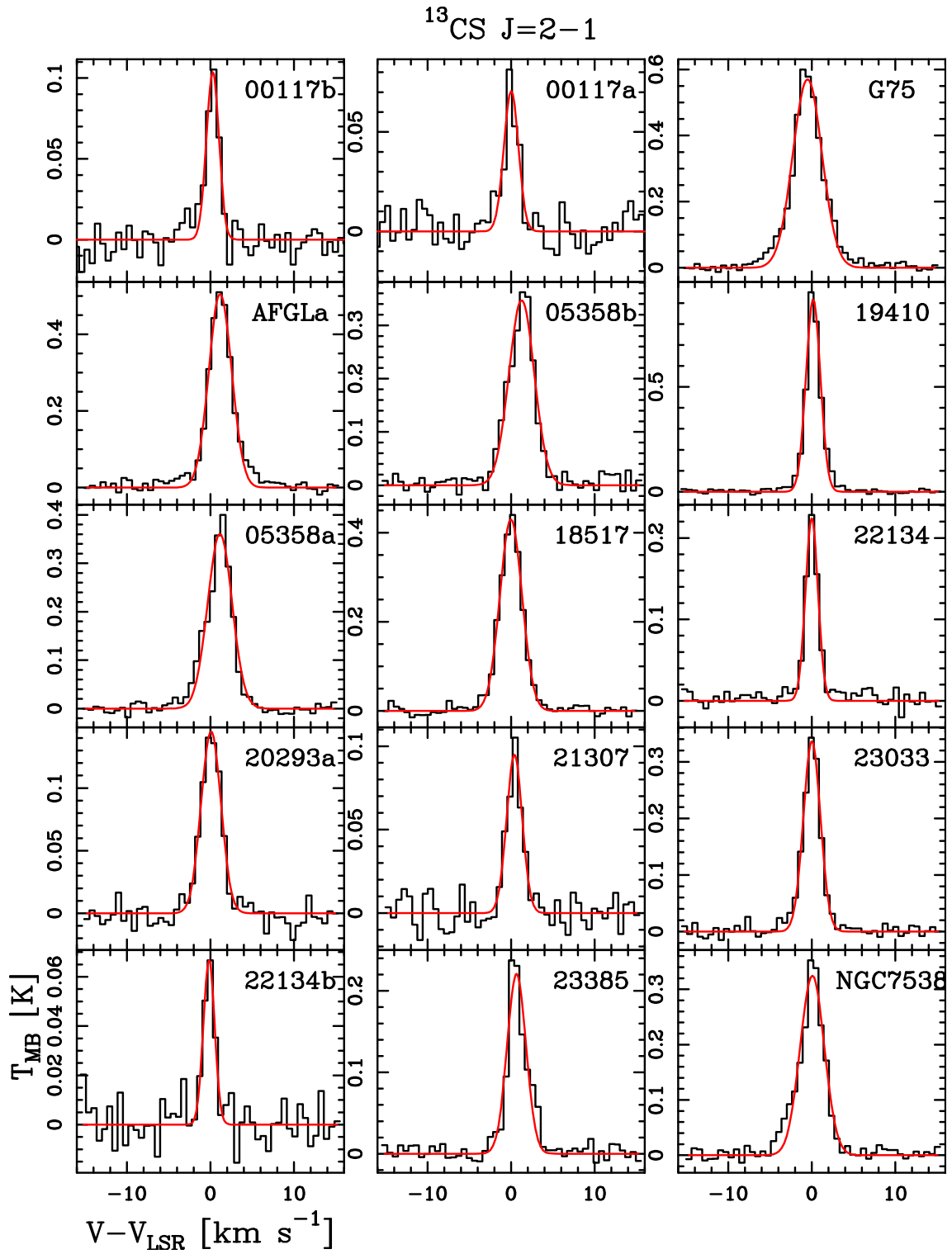


Fig. A.1. Spectra of the $^{13}\text{CS } J = 2 - 1$ lines. On the x-axis we show the velocity shift from the systemic velocity V_{LSR} listed in Table 1. In each frame, the red curve represents the best Gaussian fit performed with `MADCUBA` (see Sect. 2.3). The first column contains the HMSCs, the second the HMPOs, and the third the UCHIIs.

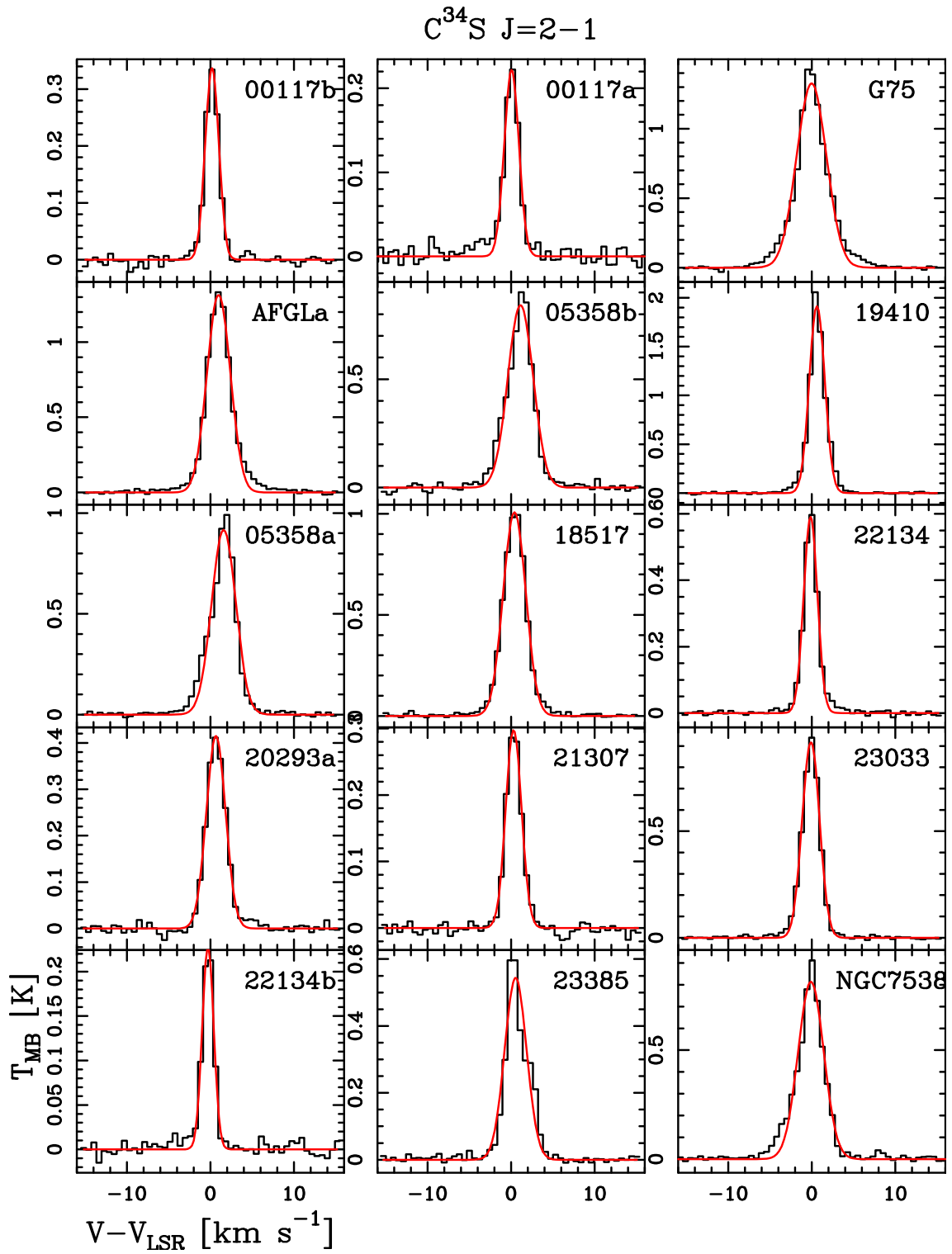


Fig. A.2. Same as Fig. A.1 for the $C^{34}S$ $J = 2 - 1$ lines.

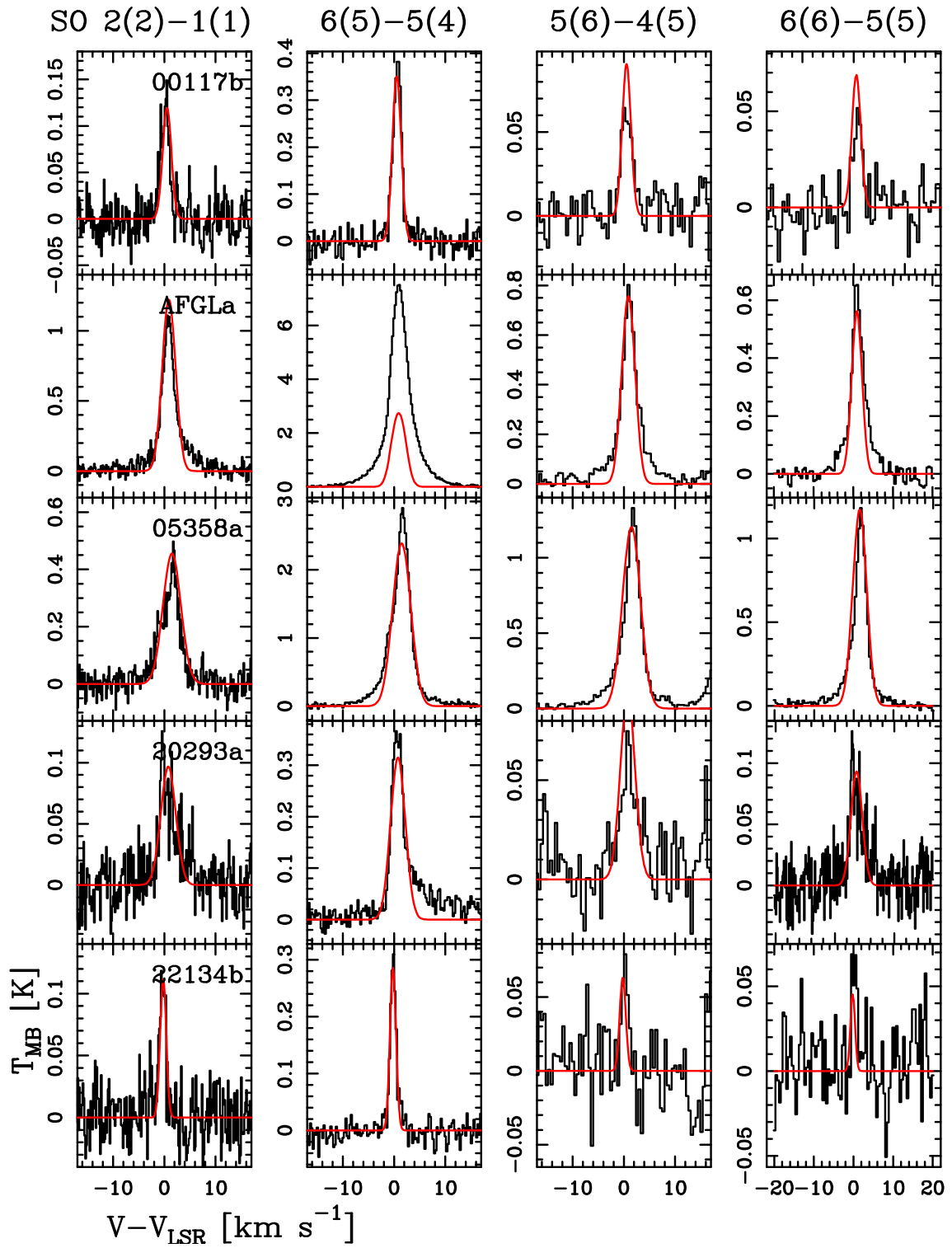


Fig. A.3. Spectra of SO $J(K) = 2(1) - 1(1)$, $6(5) - 5(4)$, $5(6) - 4(5)$, and $6(6) - 5(5)$ observed towards the HMSCs. The red curves indicate the best-fit Gaussians performed with `MADCUBA`.

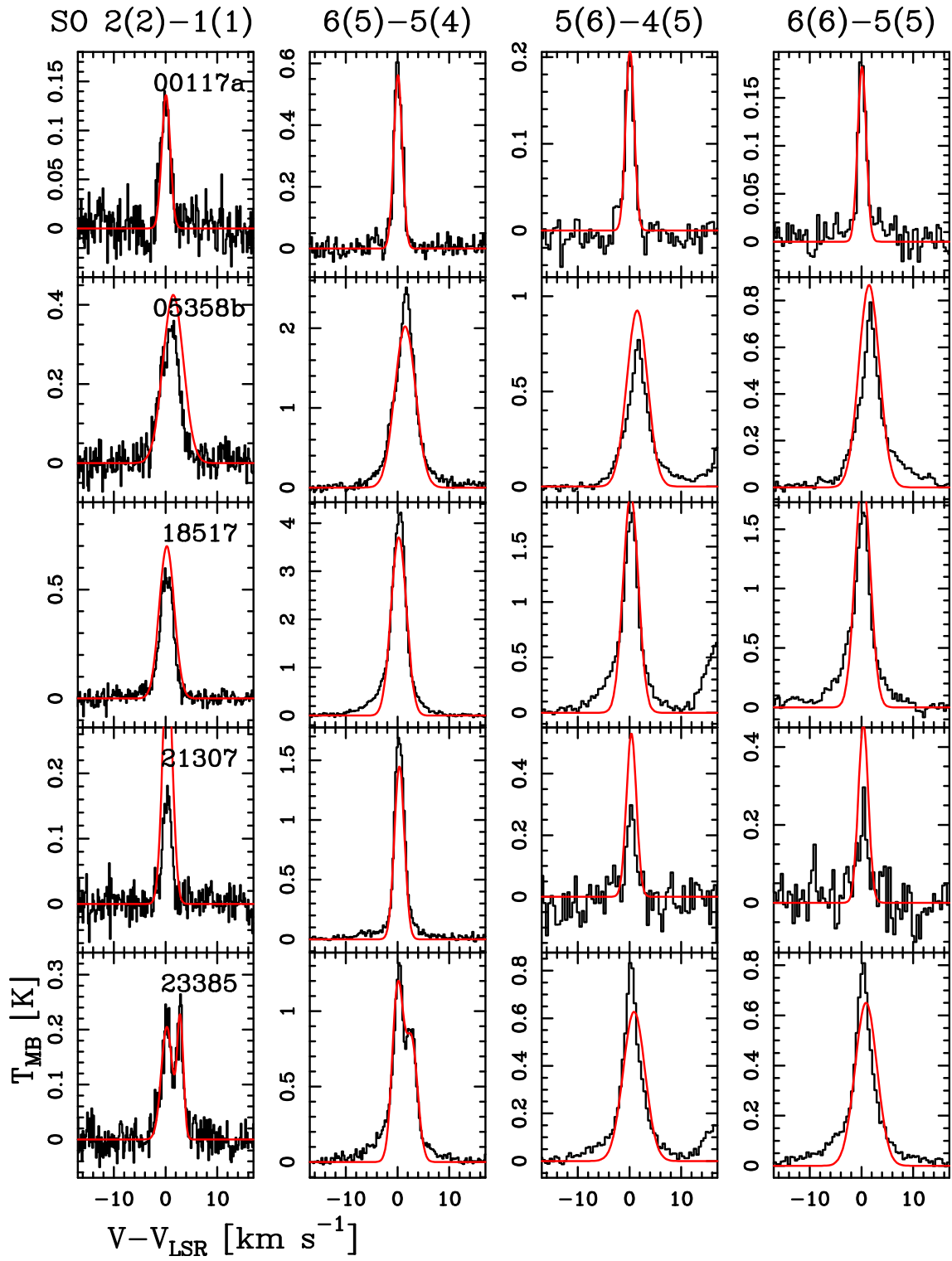


Fig. A.4. Same as Fig. A.3 for the HMPOs.

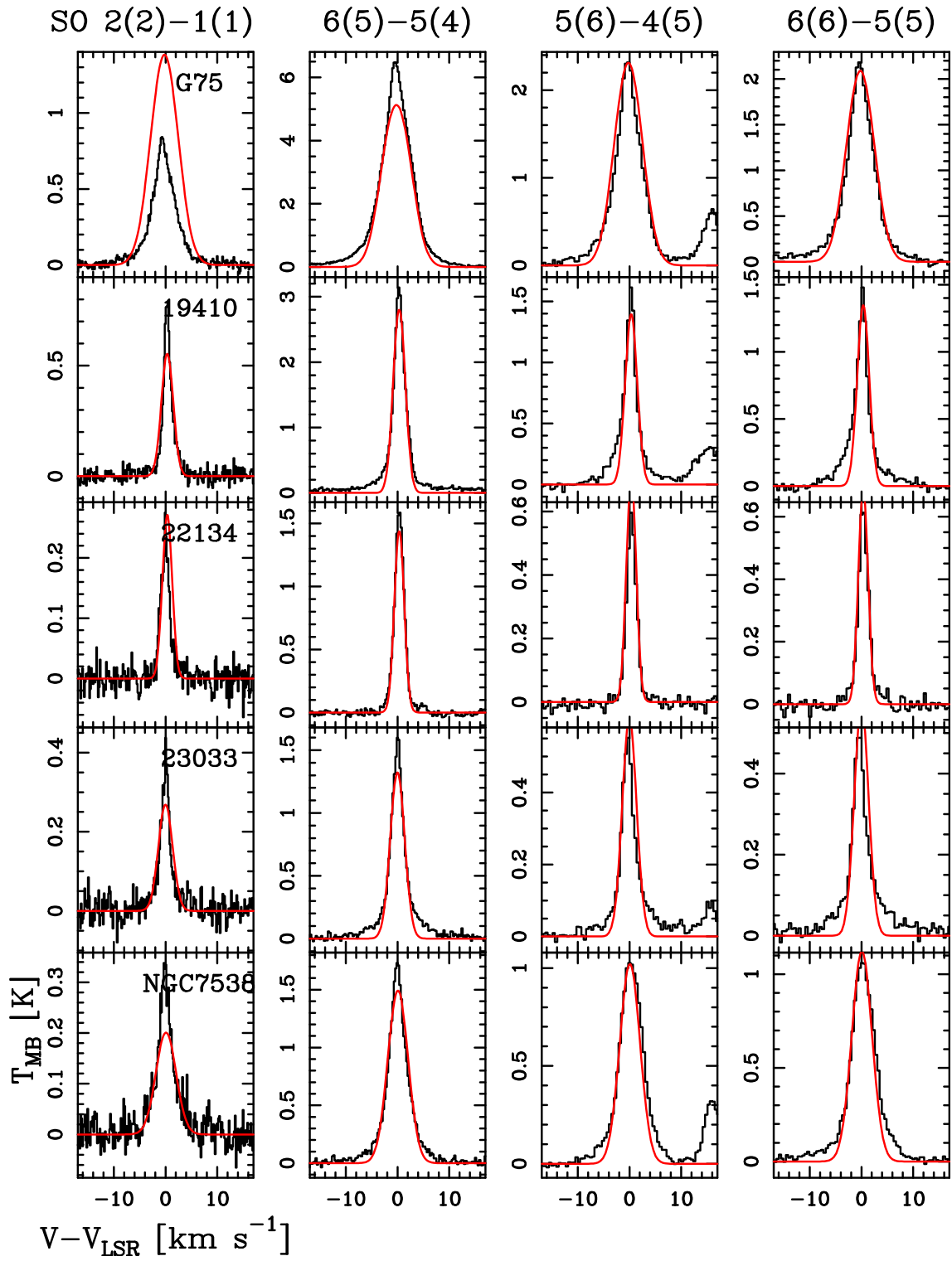


Fig. A.5. Same as Fig. A.3 for the UCHIIIs.

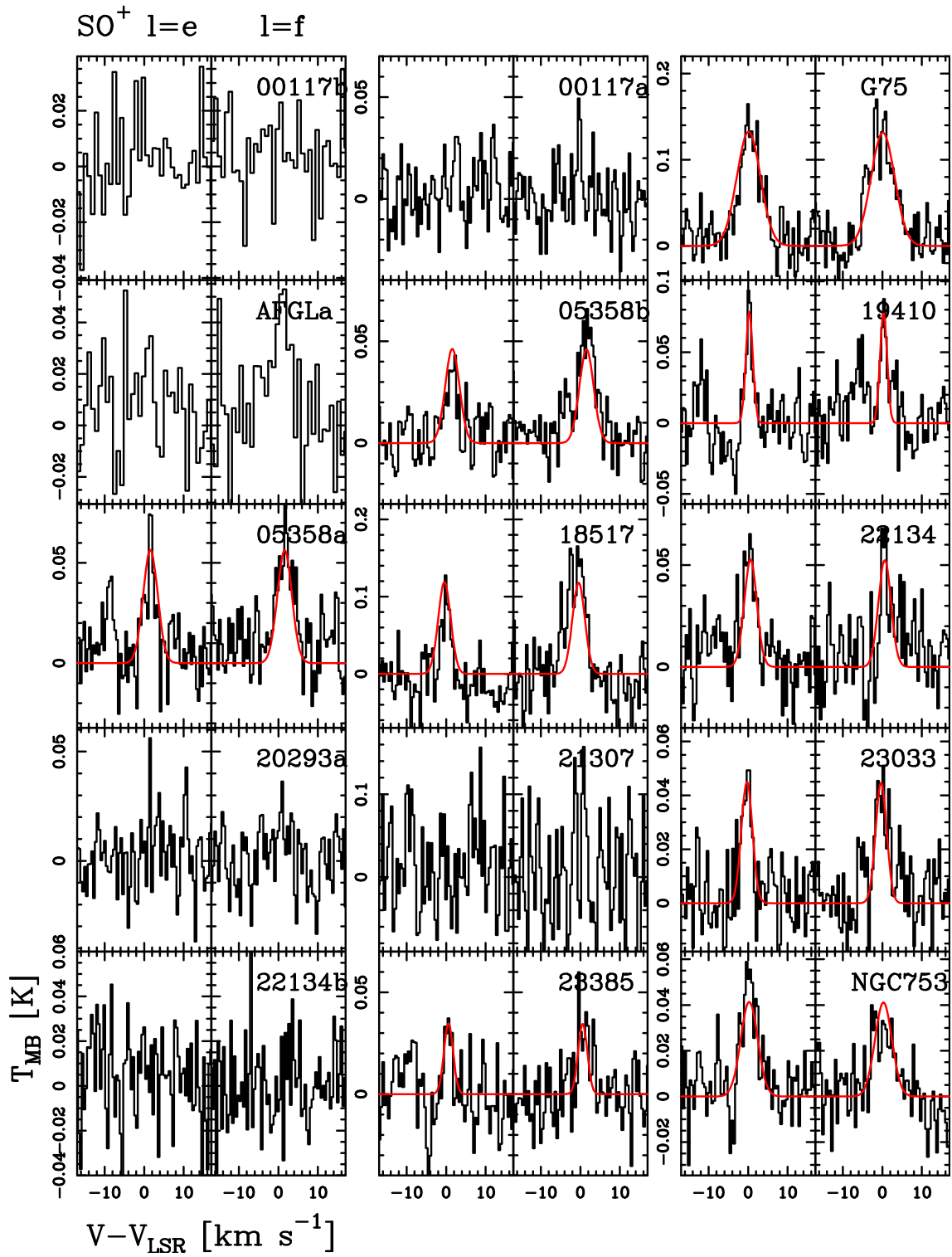


Fig. A.6. Same as Fig. A.1 for the SO^+ $J = 11/2 - 9/2$ lines.

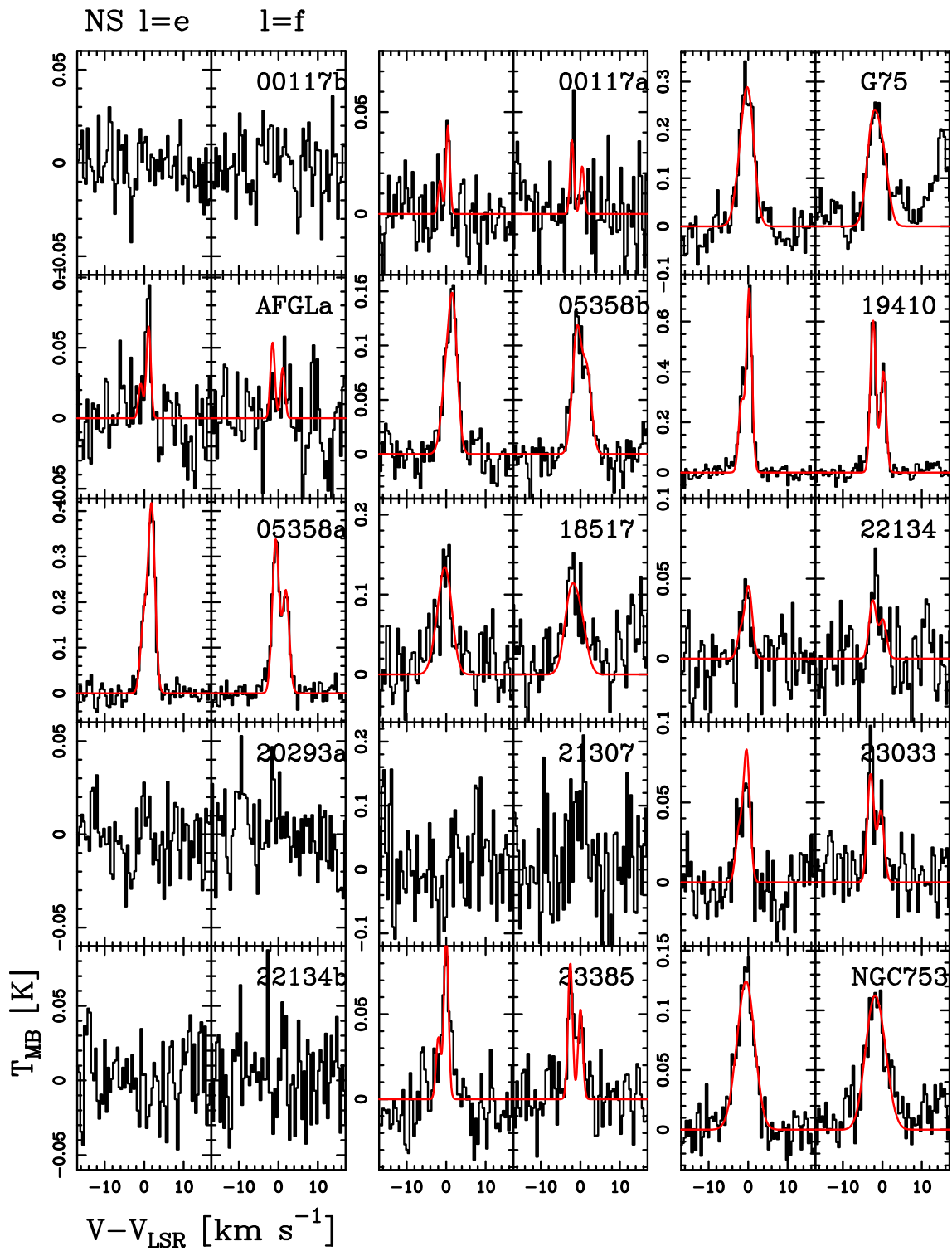


Fig. A.7. Same as Fig. A.1 for the NS $J = 11/2 - 9/2$, $F = 13/2 - 11/2$ lines.

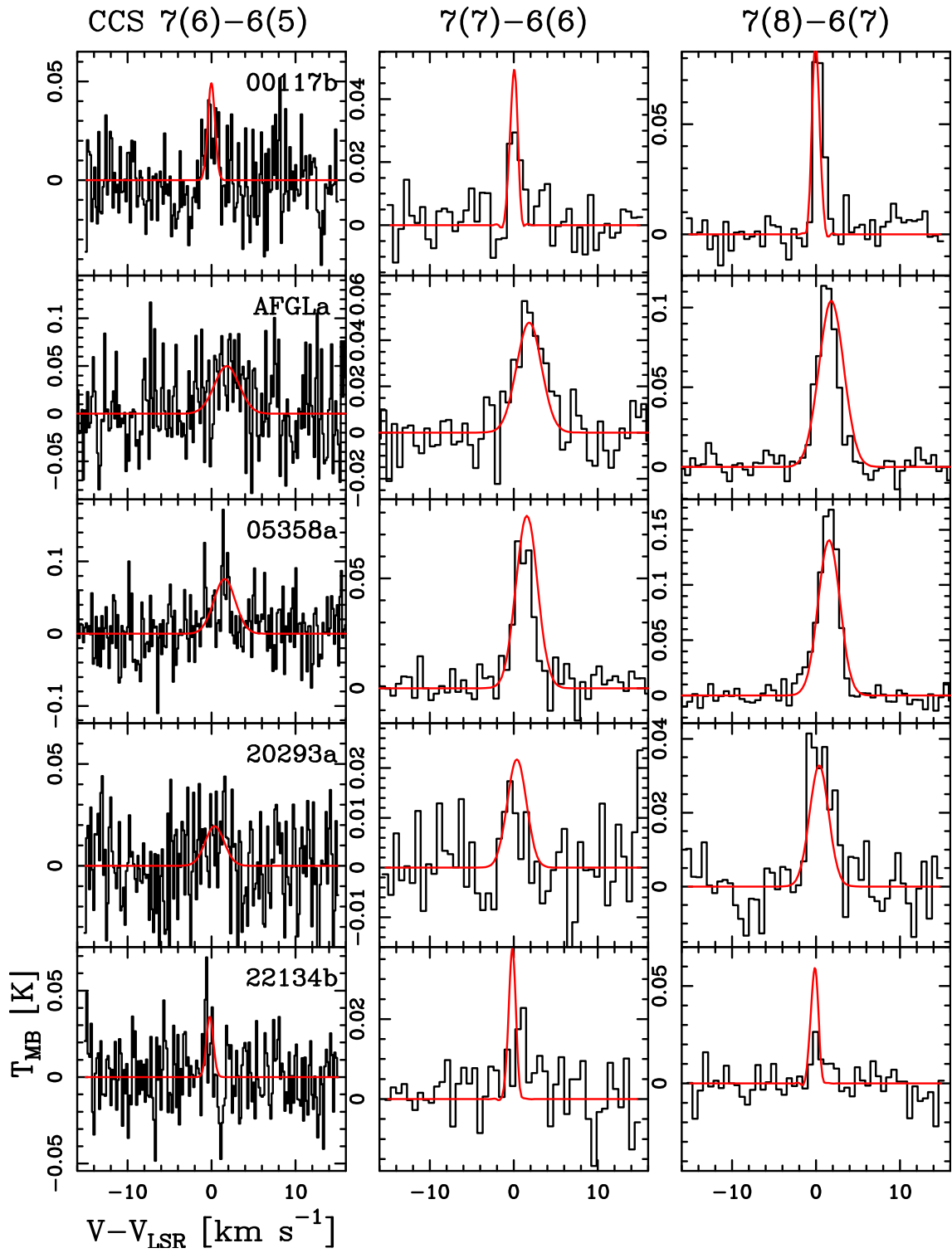


Fig. A.8. Spectra of CCS $N(J) = 7(6) - 6(5)$, $7(7) - 6(6)$, and $7(8) - 6(7)$ for the HMSCs. The red curves indicate the best fit Gaussian curves obtained with MADCUBA

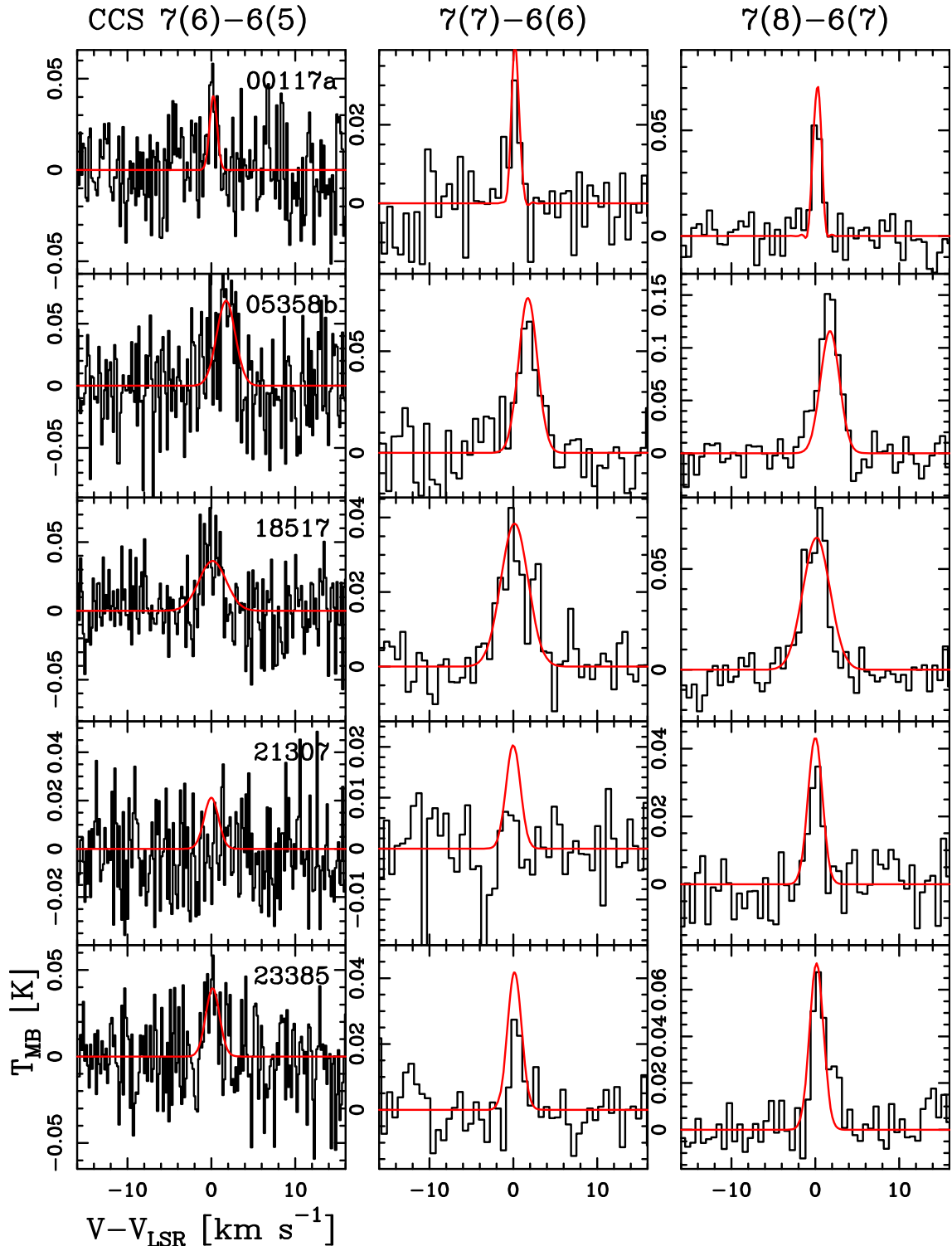


Fig. A.9. Same as Fig. A.8 for the HMPOs lines.

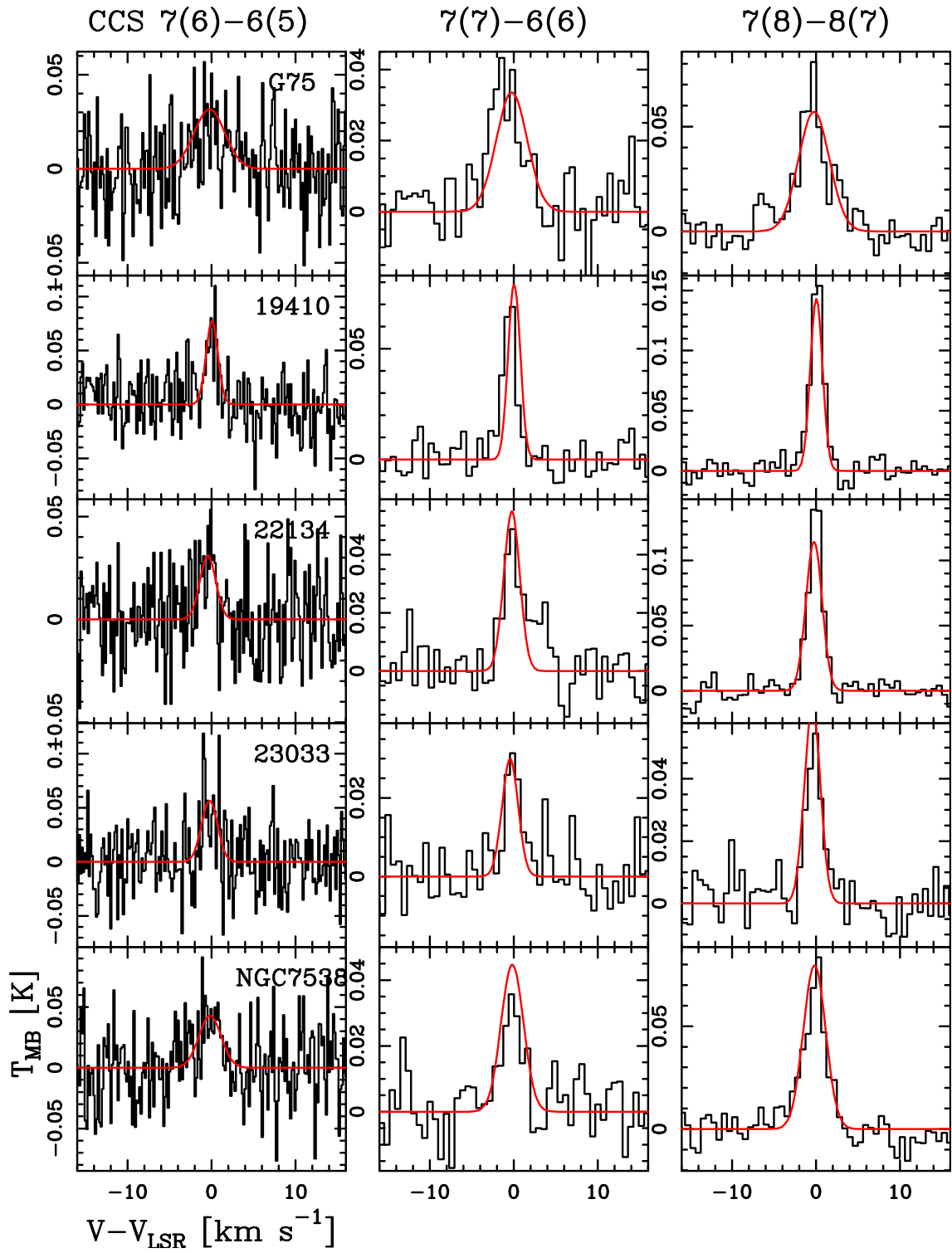


Fig. A.10. Same as Fig. A.8 the UCHII.

HCS⁺ J=2-1 J=6-5

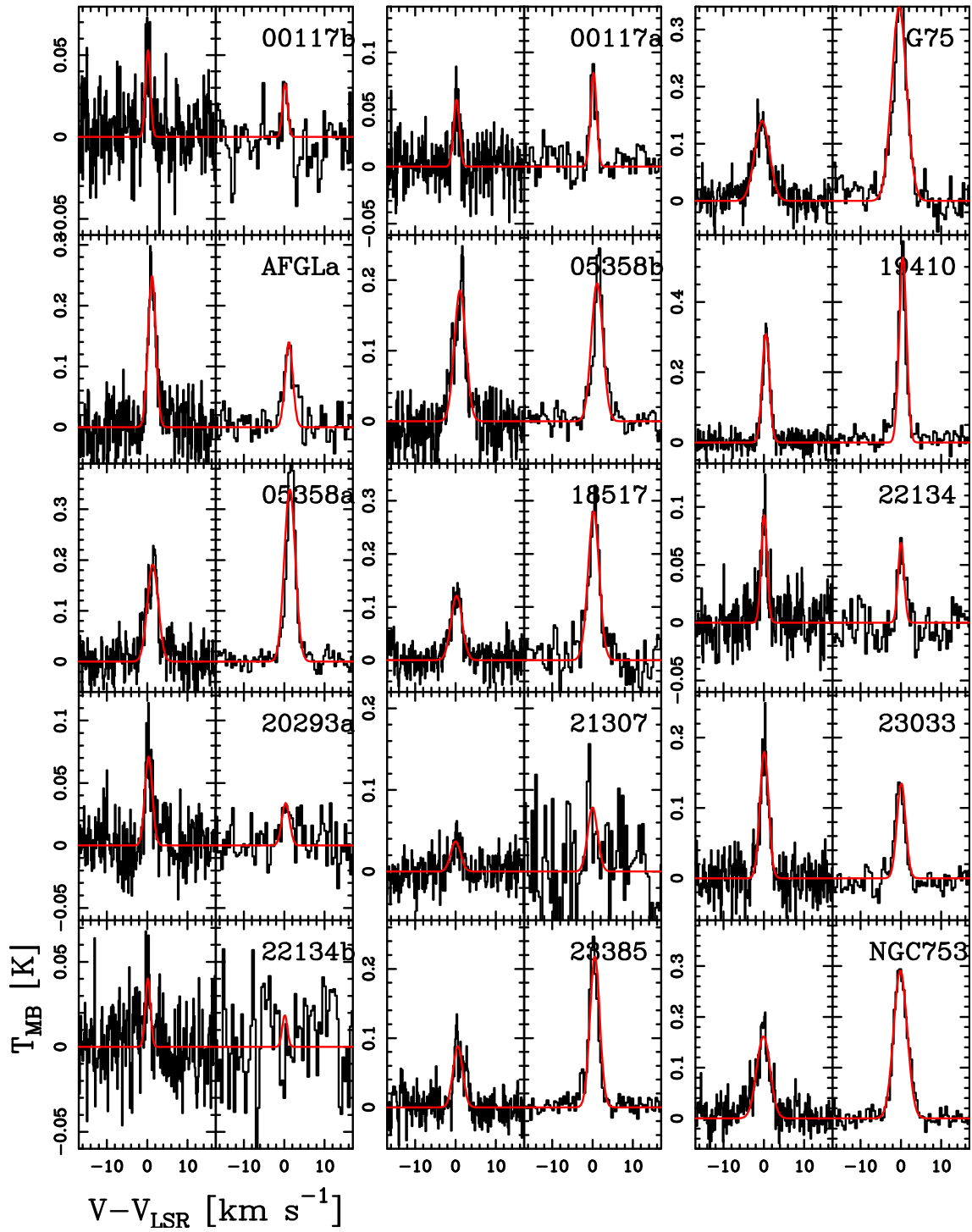


Fig. A.11. Same as Fig. A.1 for the HCS⁺ $J = 2 - 1$ and $J = 6 - 5$ lines.

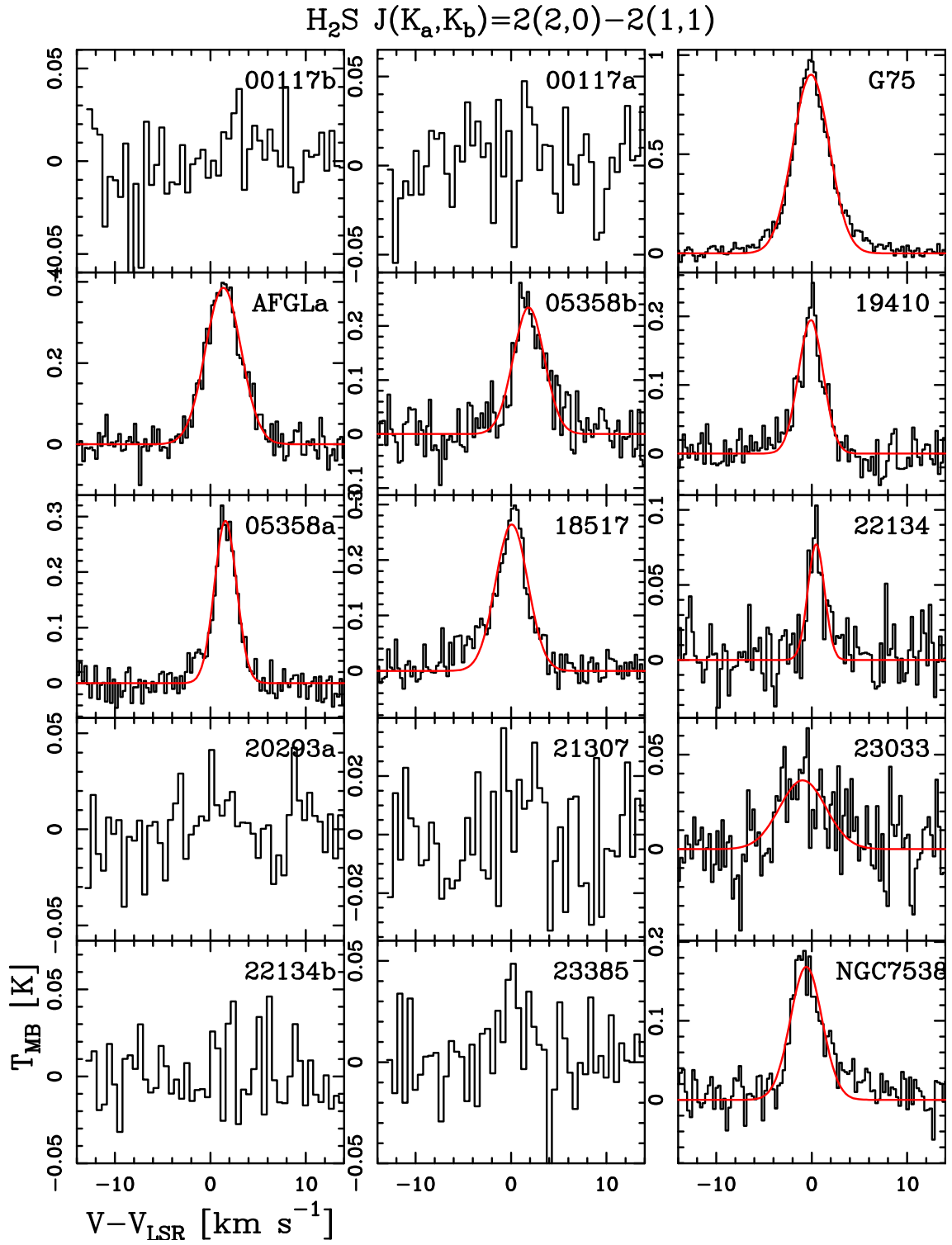


Fig. A.12. Same as Fig. A.1 for the $\text{H}_2\text{S } J(K_a, K_b) = 2(2,0) - 2(1,1)$ lines.

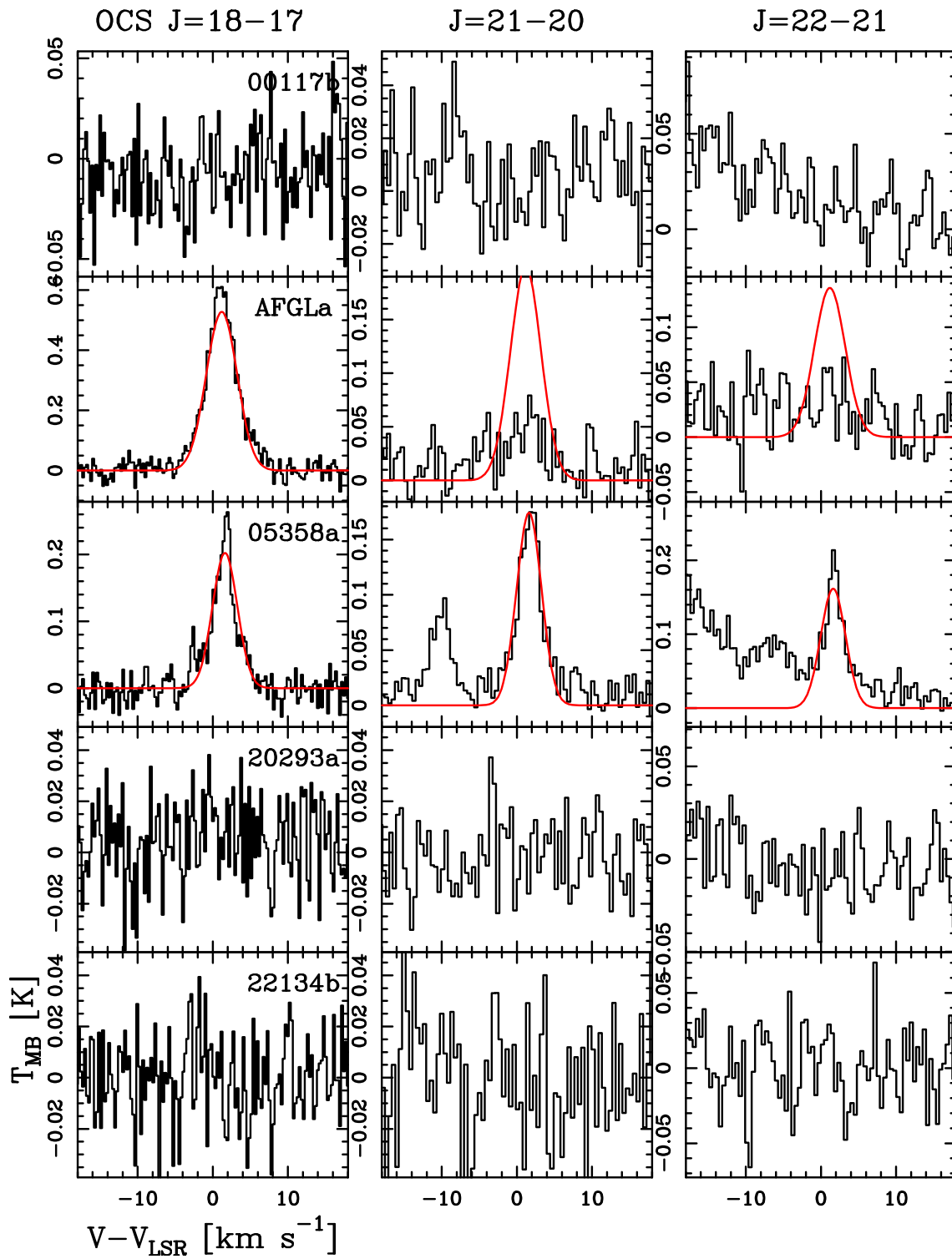


Fig. A.13. Spectra obtained towards the HMSCs of the OCS $J = 18 - 17$, $J = 21 - 20$ and $J = 22 - 21$ lines. The red curves indicate the best fit obtained with MADCUBA.

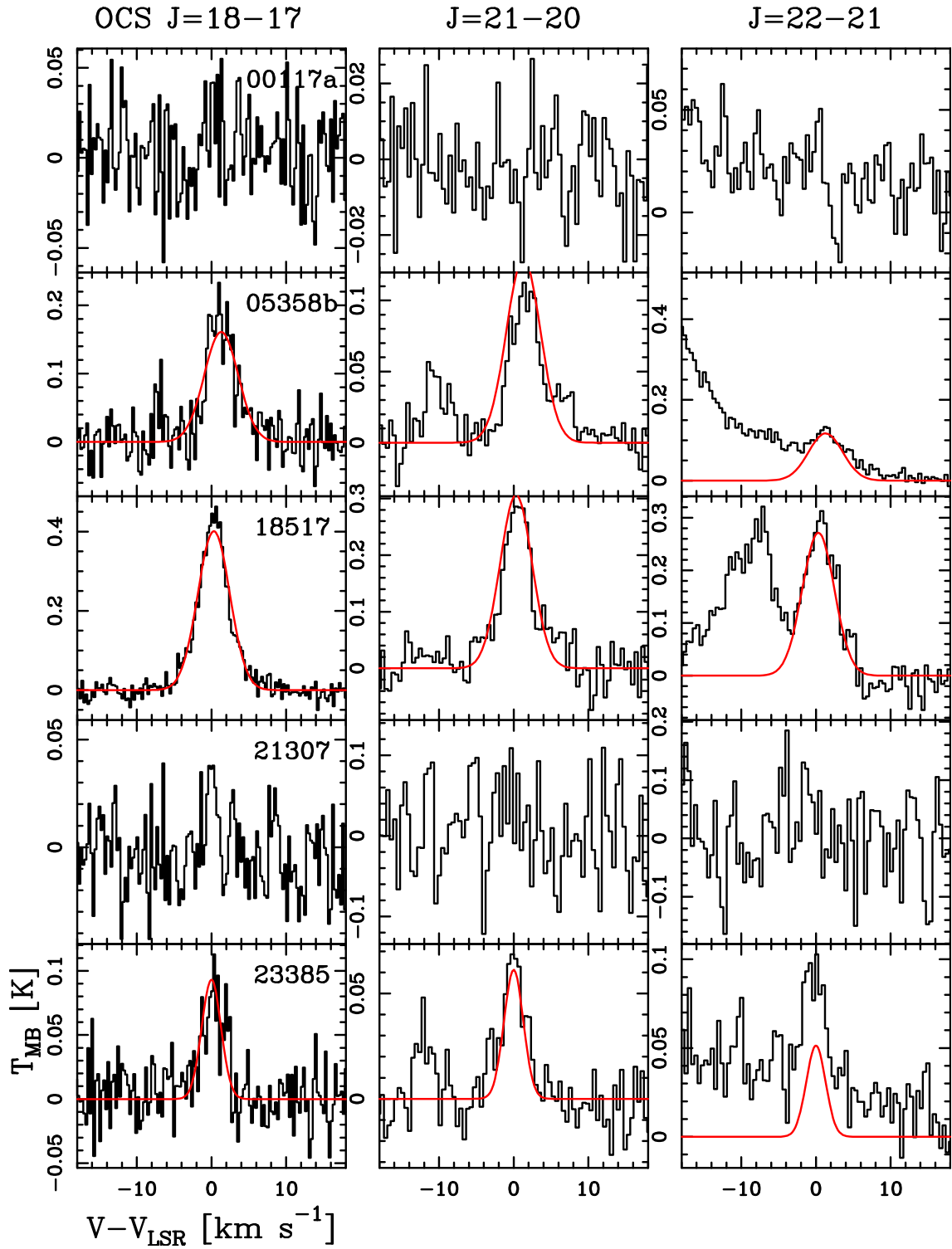


Fig. A.14. Same as Fig. A.13 for the HMPOs.

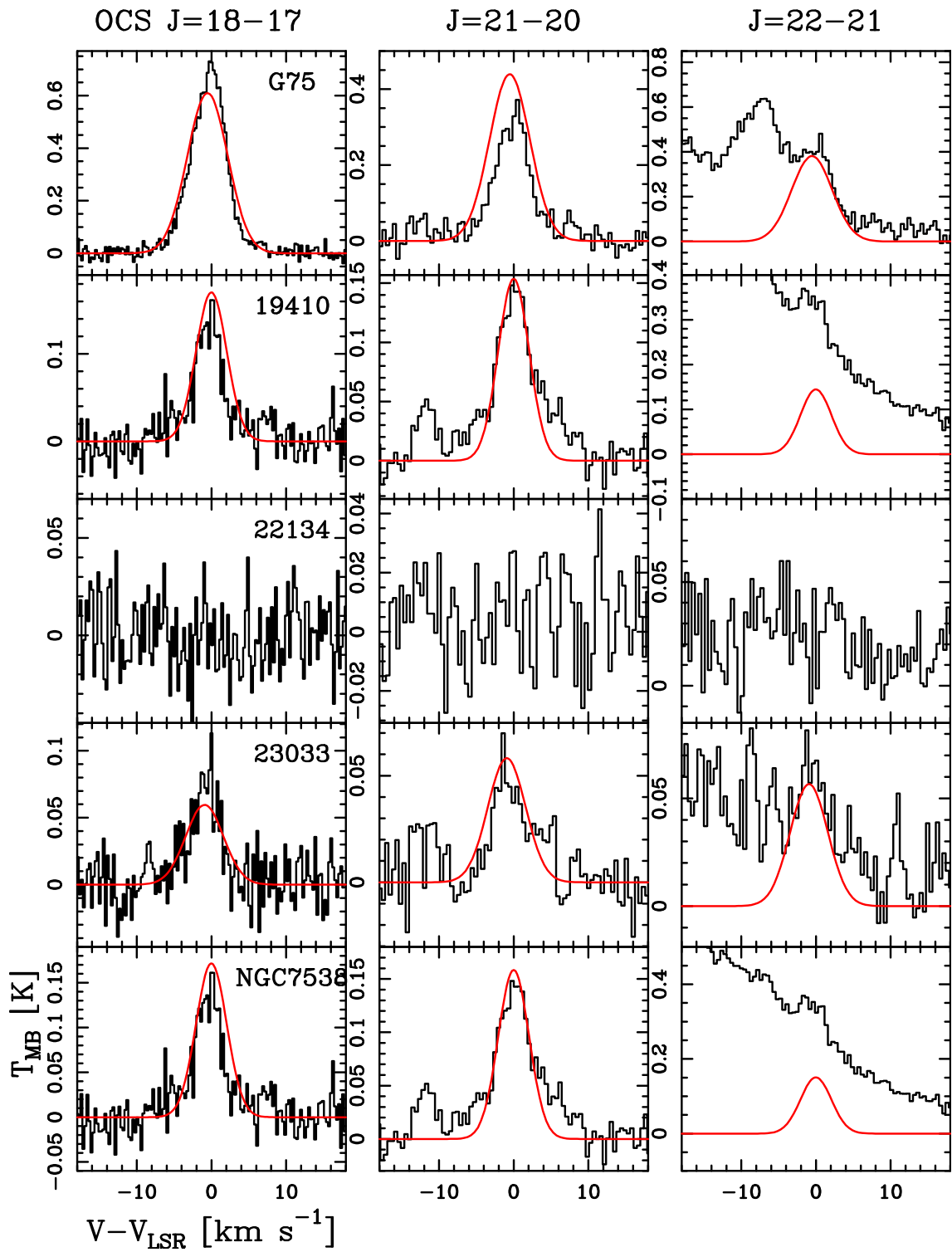


Fig. A.15. Same as Fig. A.13 for the UCHIIIs.

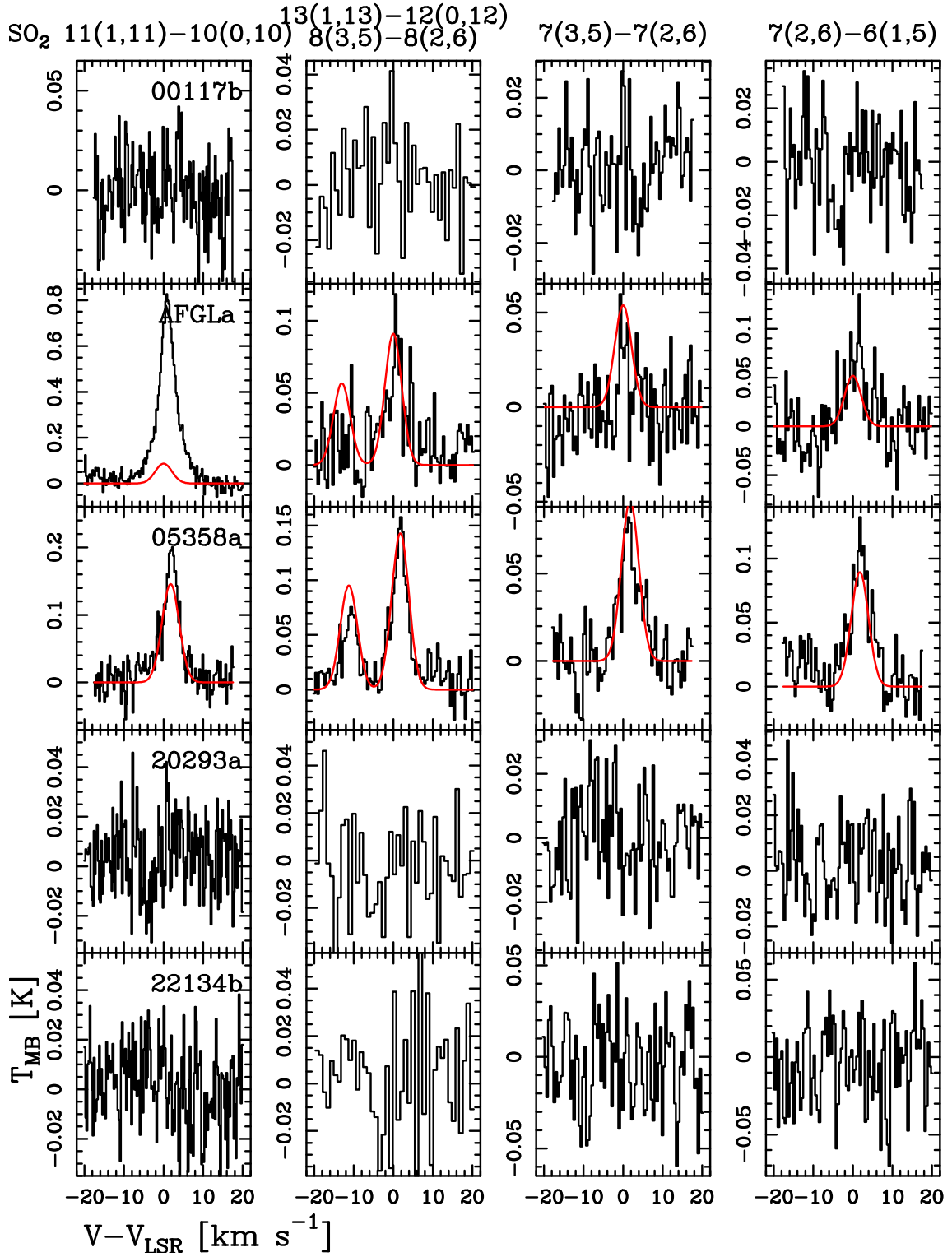


Fig. A.16. Spectra obtained towards the HMSCs of the SO₂ $J(K_a, K_b) = 11(1, 11) - 10(0, 10)$, $^{13}SO_2$ $13(1, 13) - 12(0, 12)$, $8(3, 5) - 8(2, 6)$, $7(3, 5) - 7(2, 6)$, and $7(2, 6) - 6(1, 5)$ lines. The red curves indicate the best fit obtained with MADCUBA.

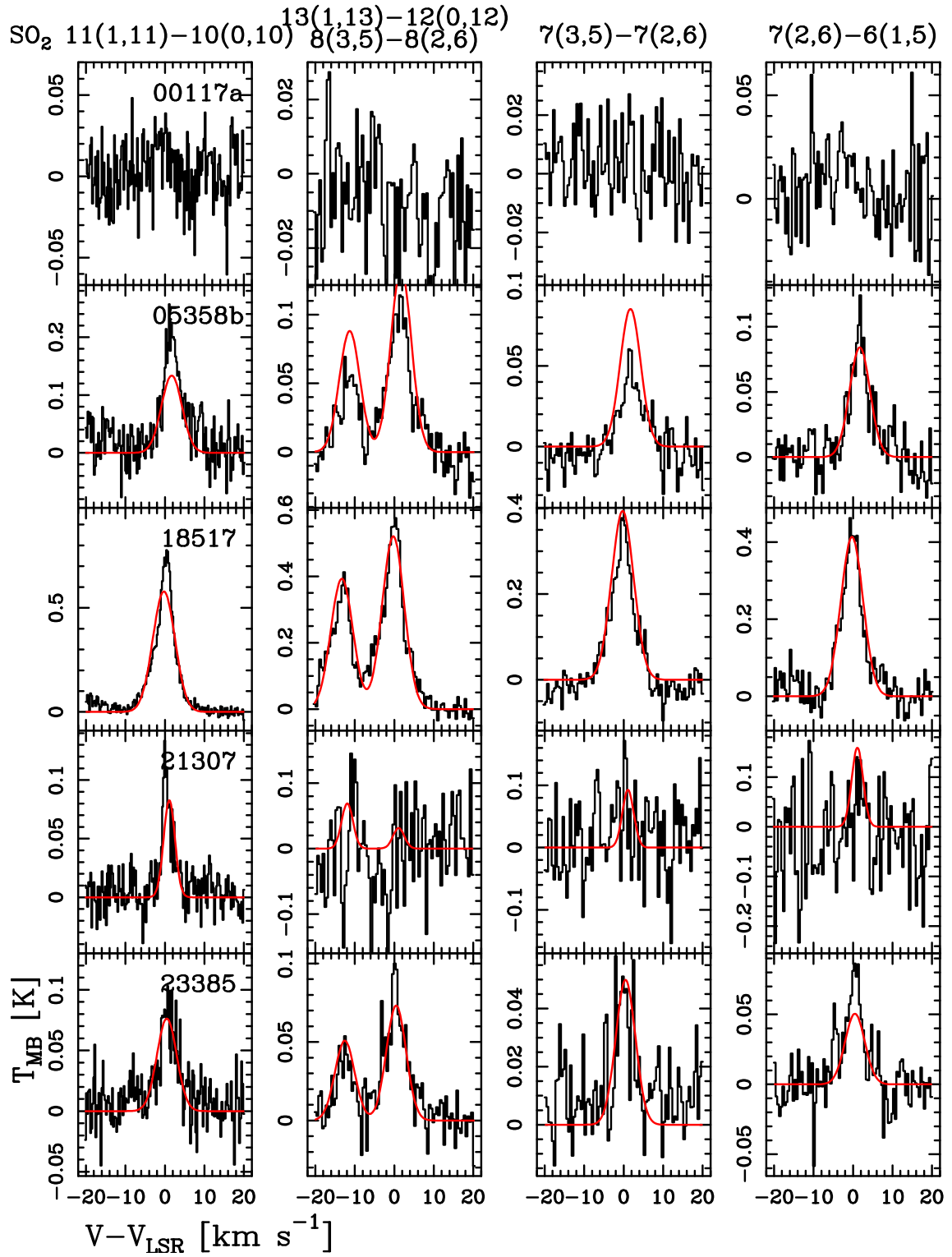


Fig. A.17. Same as Fig. A.16 for HMPOs.

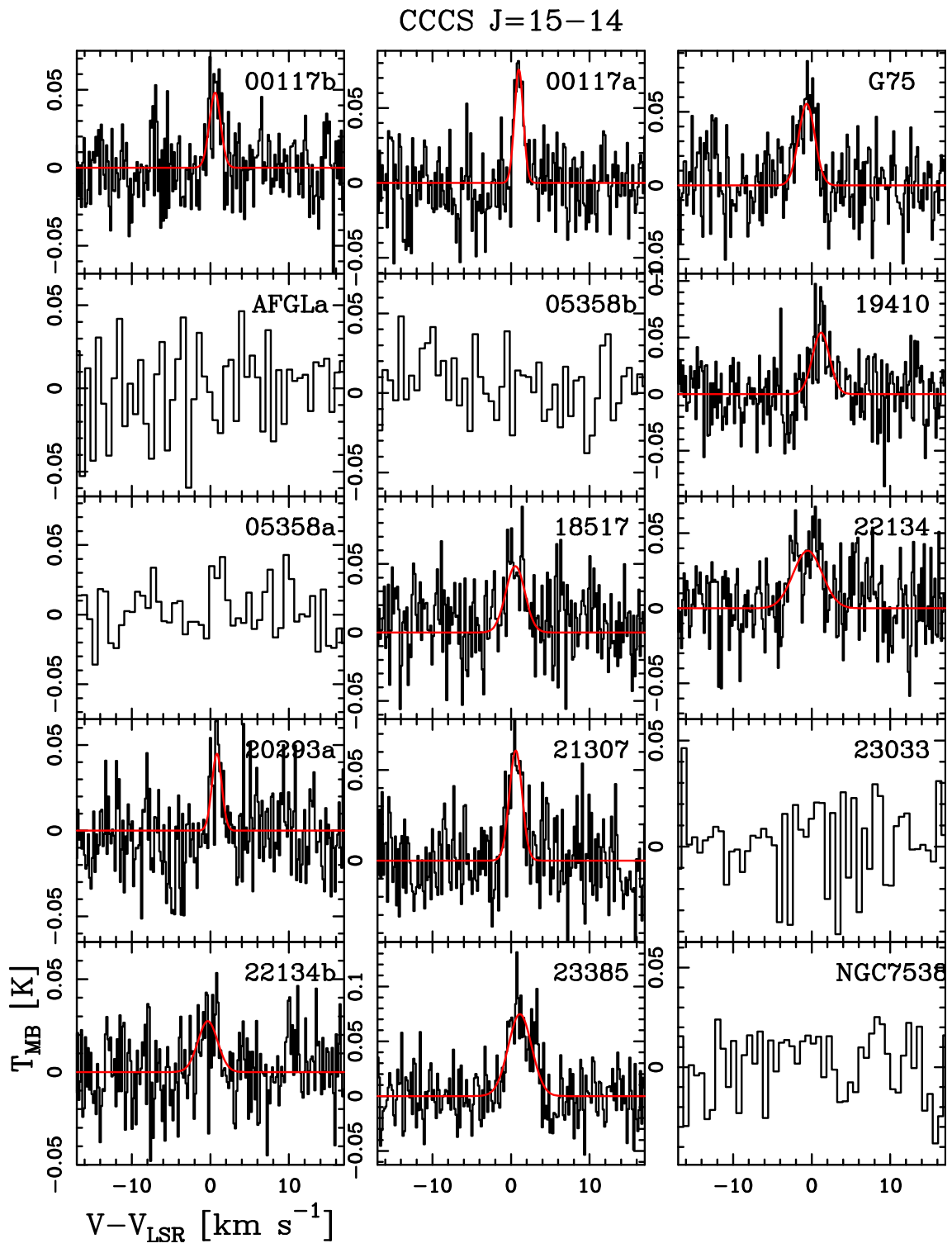


Fig. A.19. Same as Fig. A.1 for the CCCS $J = 15 - 14$ lines.

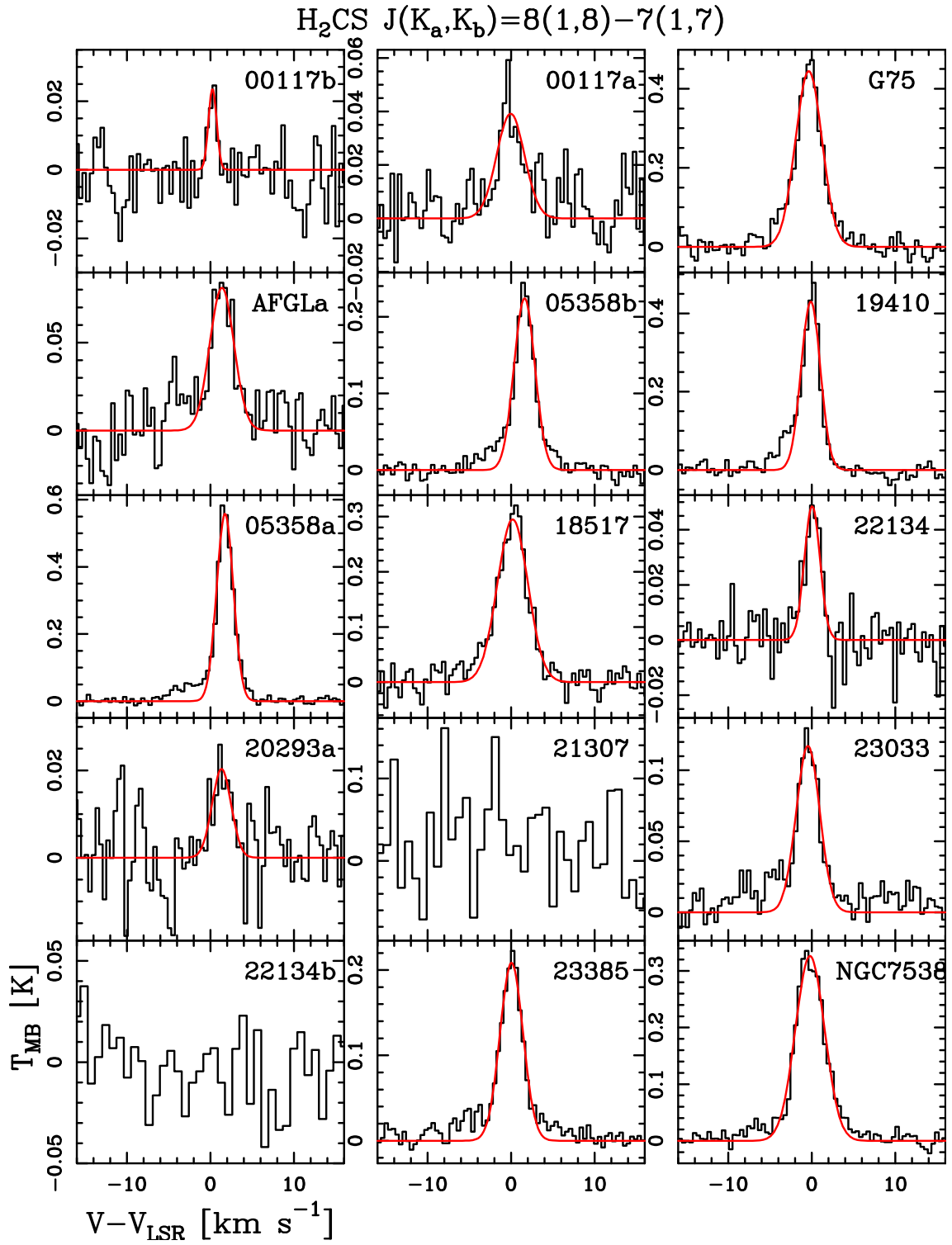


Fig. A.20. Same as Fig. A.1 for the $\text{H}_2\text{CS } J(K_a, K_b) = 8(1, 8) - 7(1, 7)$ lines.

NO $J=7/2-5/2$ $J=5/2-3/2$

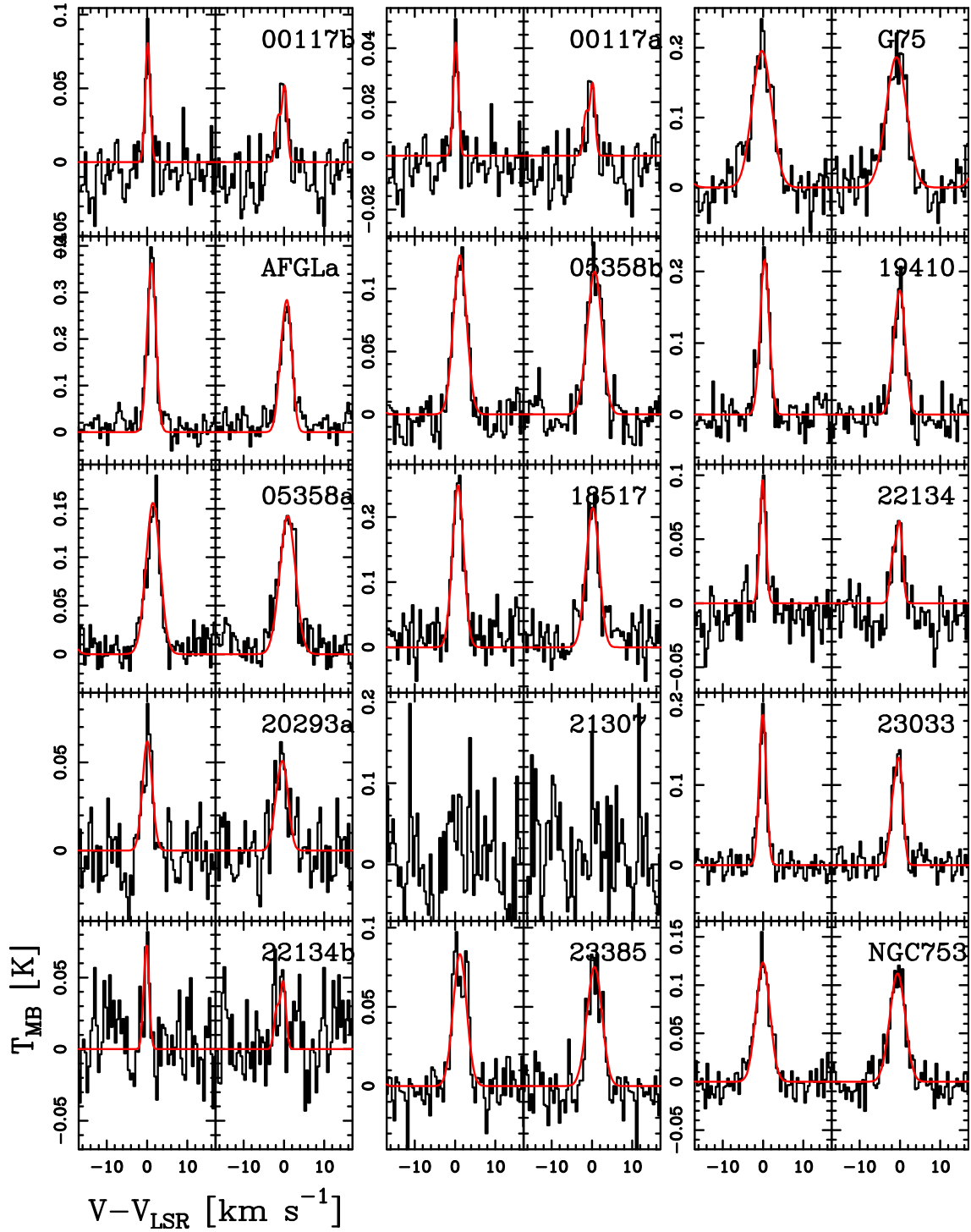


Fig. A.21. Same as Fig. A.1 for the NO lines listed in Table 3.

Appendix B: Best-fit parameters

In this appendix, we include the best-fit parameters of the species analysed obtained with `MADCUBA` (Sect. 2.3): centroid velocities, line widths at half maximum, excitation temperatures, and total column densities.

Table B.1. Best fit centroid velocities in km s⁻¹ for the molecules with two atoms analysed. Numbers in brackets give the uncertainties.

sources	¹³ CS	C ³⁴ S	SO	SO ⁺	NS	NO
HMSCs						
00117b	-36.02(0.08)	-36.07(0.02)	-35.77(0.02)	-	-	-36.1(0.12)
AFGLa	-2.71(0.05)	-2.87(0.04)	-2.04(0.05)	-	-2.79(0.14)	-2.79(0.04)
05358a	-16.46(0.08)	-16.48(0.08)	-16.17(0.08)	-16.0(0.2)	-15.70(0.02)	-16.18(0.08)
20293a	6.39(0.05)	7.00(0.02)	7.08(0.04)	-	-	6.37(0.16)
22134b	-18.46(0.08)	-18.55(0.02)	18.53(0.02)	-	-	-18.46(0.13)
HMPOs						
00117a	-36.02(0.08)	-36.20(0.03)	-36.21(0.02)	-	-35.83(0.12)	-36.14(0.09)
05358b	-16.33(0.07)	-16.43(0.06)	-16.12(0.03)	-16.1(0.2)	-15.91(0.06)	-16.10(0.08)
18517	43.70(0.03)	44.14(0.02)	43.94(0.02)	43.2(0.3)	43.82(0.14)	44.44(0.08)
21307	-46.29(0.06)	-46.35(0.02)	-46.33(0.03)	-	-	-
23385	-49.8(0.1)	-49.9(0.1)	-49.54(0.03)	-49.9(0.3)	-50.3(0.1)	-49.24(0.15)
UCHIIs						
G75	-0.30(0.07)	0.22(0.07)	-0.01(0.5)	0.4(0.2)	0.30(0.09)	-0.04(0.11)
19410	22.58(0.03)	23.07(0.04)	22.75(0.02)	22.7(0.1)	22.67(0.02)	22.80(0.06)
22134	-18.29(0.03)	-18.41(0.02)	-17.97(0.02)	-17.8(0.2)	-18.1(0.2)	-18.40(0.10)
23033	-52.96(0.03)	-53.06(0.02)	-53.02(0.02)	-53.3(0.2)	-53.4(0.1)	-53.09(0.05)
NGC7538	-56.93(0.08)	-57.06(0.07)	-56.96(0.02)	-56.6(0.2)	-57.11(0.09)	-57.04(0.08)

Table B.2. Same as Table B.1 for the remaining molecular species

sources	CCS	HCS ⁺	H ₂ S	OCS	SO ₂	CCCS	H ₂ CS
HMSCs							
00117b	-36.16(0.09)	-36.13(0.09)	-	-	-	-35.7(0.1)	-36.04(0.09)
AFGLa	-2.1(0.2)	-2.72(0.03)	-2.54(0.05)	-2.72(0.04)	-2.7(0.1)	-	-2.52(0.17)
05358a	-16.0(0.1)	-16.33(0.06)	-16.02(0.05)	-16.0(0.1)	-15.7(0.1)	-	-15.84(0.04)
20293a	7.1(0.3)	6.67(0.06)	-	-	-	7.14(0.07)	7.6(0.3)
22134b	-	-18.37(0.06)	-	-	-	-18.6(0.02)	-
HMPOs							
00117a	-36.1(0.1)	-36.03(0.07)	-	-	-	-35.29(0.04)	-36.3(0.2)
05358b	-15.9(0.1)	-16.62(0.06)	-15.7(0.1)	-16.3(0.1)	-16.0(0.1)	-	-15.99(0.06)
18517	43.9(0.2)	43.90(0.05)	43.78(0.08)	43.98(0.09)	43.4(0.1)	44.3(0.1)	43.90(0.08)
21307	-	-46.40(0.12)	-	-	-	-46.09(0.07)	-
23385	-50.34(0.09)	-49.65(0.07)	-	-50.3(0.2)	-50.1(0.1)	-49.4(0.1)	-50.44(0.07)
UCHIIs							
G75	-0.03(0.02)	-0.37(0.05)	0.13(0.04)	-0.17(0.09)	0.40(0.08)	-0.41(0.09)	-0.15(0.06)
19410	22.46(0.05)	22.95(0.02)	22.31(0.05)	21.8(0.1)	22.20(0.08)	23.6(0.1)	22.29(0.07)
22134	-18.7(0.13)	-18.27(0.05)	-17.8(0.1)	-	-17.82(0.06)	-18.8(0.2)	-18.2(0.2)
23033	-53.23(0.09)	-52.87(0.03)	-53.9(0.4)	-53.8(0.2)	-53.6(0.1)	-	-53.44(0.09)
NGC7538	-57.2(0.13)	-57.08(0.05)	-57.6(0.1)	-57.4(0.5)	-56.7(0.1)	-	-57.20(0.06)

Table B.3. Best fit line widths at half maximum in km s^{-1} for the molecules with two atoms analysed. Numbers in brackets give the uncertainty.

source	^{13}CS	C^{34}S	SO	SO^+	NS	NO
HMSCs						
00117b	1.8(0.2)	1.89(0.04)	2.02(0.05)	–	–	1.5(0.3)
AFGLa	3.2(0.1)	3.19(0.09)	4.4(0.1)	–	1.3(0.3)	2.6(0.1)
05358a	3.4(0.2)	3.4(0.2)	4.1(0.2)	4.3(0.4)	2.01(0.05)	4.2(0.2)
20293a	2.8(0.1)	2.70(0.06)	3.46(0.09)	–	–	2.9(0.4)
22134b	1.6(0.2)	1.61(0.06)	1.45(0.05)	–	–	1.6(0.3)
HMPOs						
00117a	1.8(0.2)	2.02(0.08)	1.94(0.03)	2.02	1.2(0.3)	2.0(0.2)
05358b	3.6(0.2)	3.50(0.15)	4.61(0.07)	5.3(0.6)	2.73(0.16)	3.3(0.1)
18517	3.11(0.06)	3.12(0.05)	3.34(0.05)	4.5(0.7)	2.9(0.4)	3.3(0.2)
21307	2.2(0.2)	2.20(0.05)	2.25(0.06)	–	–	–
23385	2.7(0.3)	3.1(0.3)	4.94(0.08)	2.7(0.7)	2.1(0.2)	4.2(0.4)
HMSCs						
G75	4.1(0.2)	4.12(0.15)	6.24(0.10)	7.0(0.5)	3.5(0.3)	5.7(0.3)
19410	2.01(0.08)	2.11(0.08)	2.65(0.03)	2.0(0.3)	1.65(0.04)	2.6(0.2)
22134	1.77(0.07)	1.91(0.06)	2.21(0.04)	4.0(0.4)	2.3(0.5)	1.7(0.2)
23033	2.40(0.08)	2.40(0.05)	3.09(0.05)	3.8(0.4)	2.0(0.2)	2.1(0.1)
NGC7538	3.4(0.2)	3.6(0.2)	4.39(0.04)	5.3(0.6)	5.0(0.2)	4.0(0.2)

Notes. The values without uncertainty are the FWHMs assumed to compute the column density upper limits.

Table B.4. Same as Table B.3 for the remaining molecular species

source	CCS	HCS^+	$\text{p-H}_2\text{S}$	OCS	SO_2	CCCS	$\text{o-H}_2\text{CS}$
HMSCs							
00117b	1.5(0.2)	1.6(0.2)	2.02	2.02	2.02	1.7(0.2)	1.13(0.22)
AFGLa	3.5(0.5)	2.28(0.08)	4.40(0.12)	4.69(0.08)	4.7(0.3)	2.28	3.4(0.4)
05358a	3.0(0.2)	3.41(0.14)	2.7(0.1)	3.89(0.2)	5.2(0.3)	3.41	2.33(0.09)
20293a	2.9(0.6)	2.12(0.15)	3.46	3.46	3.46	1.5(0.2)	2.7(0.6)
22134b	1.61	2.18(0.30)	1.45	1.45	1.45	2.9(0.5)	1.61
HMPOs							
00117a	1.0(0.3)	1.7(0.2)	1.94	1.94	1.94	1.3(0.1)	3.9(0.6)
05358b	2.7(0.3)	3.74(0.14)	3.8(0.3)	5.4(0.3)	6.3(0.2)	3.74	2.92(0.15)
18517	3.8(0.6)	3.27(0.11)	4.0(0.2)	4.7(0.2)	5.9(0.2)	2.9(0.3)	4.27(0.18)
21307	0.0(0.0)	2.9(0.3)	2.25	2.25	3.37	1.9(0.2)	0. (0.)
23385	2.0(0.2)	3.10(0.17)	4.94	4.0(0.4)	5.9(0.3)	3.5(0.2)	3.23(0.16)
UCHIIs							
G75	4.3 (0.4)	4.52(0.12)	4.48(0.09)	6.3 (0.2)	6.8 (0.2)	2.4 (0.2)	3.73(0.14)
19410	1.7(0.1)	2.09(0.04)	3.1(0.1)	5.5(0.3)	6.4(0.3)	2.6(0.2)	2.69(0.16)
22134	2.2(0.3)	1.89(0.12)	2.0(0.3)	0. (0.)	2.5(0.1)	4.3(0.4)	2.2(0.4)
23033	2.3(0.2)	2.49(0.08)	6.0(1.0)	4.5(0.4)	4.4(0.2)	2.49	3.3(0.2)
NGC7538	3.1(0.3)	3.59(0.18)	3.9(0.2)	5.3(1.1)	5.4(0.2)	3.59	4.10(0.13)

Notes. The values without uncertainty are the FWHMs assumed to compute the column density upper limits

Table B.5. Excitation temperatures (in K) derived with MADCUBA.

source	SO	CCS	HCS ⁺	OCS	SO ₂
HMSCs					
00117b	11.9(0.4)	12(3)	13(3)	–	–
AFGLa	11(1)	18(3)	12.8(0.7)	– ^a	73 ^b
05358a	24.2(1.0)	17(3)	22.0(1.0)	76(3)	68(3)
20293a	12.6(0.4)	12(3)	12.1(0.9)	–	–
22134b	10.7(0.4)	12(4)	12(2)	–	–
HMPOs					
00117a	16.7(0.4)	13(3)	19(2)	21	–
05358b	20.9(0.5)	26(4)	16.6(0.6)	66(5)	63(5)
18517	25.8(0.6)	21(3)	26.4(0.9)	60(3)	48(4)
21307	16.5(0.9)	16(4)	25(2)	21	17(2)
23385	33.0(0.6)	22(3)	27.8(1.0)	48(2)	56(5)
UCHIIs					
G75	18.4(0.9)	29(5)	27.3(0.5)	54(4)	47(5)
19410	23.4(0.4)	25(2)	21.5(0.3)	85(8)	42(5)
22134	23.9(0.6)	25(5)	14.3(1.2)	–	62(6)
23033	21.3(0.4)	13(2)	14.4(0.6)	105(8)	50(4)
NGC7538	49.7(1.0)	21(3)	22.3(0.5)	90(6)	93(7)

Notes. The values without uncertainty are the temperatures assumed to derive the upper limits on the total column densities. ^(a) the $J = 18 - 17$ line is too strong with respect to the LTE predictions. It is unlikely that the discrepancy in intensity between this line and the LTE prediction is due to contamination with nearby lines because no reliable candidates have been found around it; ^(b) T_{ex} needs to be fixed to 73 K to obtain a reasonable fit, but the $J(K_a, K_b) = 11(1, 11) - 10(0, 10)$ intensity is largely underestimated probably due to contamination with methyl formate $J(K_a, K_b) = 11(5, 6) - 11(3, 9)$ at 221.969 GHz.

Table B.6. Column densities in cm⁻² of the analysed diatomic molecules

source	¹³ CS	C ³⁴ S	SO	SO ⁺	NS	NO
HMSCs						
00117b	1.0(0.1)×10 ¹²	3.16(0.06)×10 ¹²	1.7(0.1)×10 ¹³	3.2×10 ¹²	5.0×10 ¹¹	1.9(0.2)×10 ¹⁴
AFGLa	8.9(0.3)×10 ¹²	2.34(0.06)×10 ¹³	3.0(0.2)×10 ¹⁴	1.3×10 ¹³	2.5(0.8)×10 ¹²	1.48(0.05)×10 ¹⁵
05358a	7.6(0.3)×10 ¹²	1.82(0.08)×10 ¹³	1.4(0.2)×10 ¹⁴	7.1(0.4)×10 ¹²	1.95(0.02)×10 ¹³	8.5(0.3)×10 ¹⁴
20293a	2.24(0.08)×10 ¹²	5.9(0.1)×10 ¹²	2.2(0.1)×10 ¹³	5.0×10 ¹²	5.0×10 ¹¹	2.3(0.3)×10 ¹⁴
22134b	5.9(0.6)×10 ¹¹	1.95(0.06)×10 ¹²	1.20(0.06)×10 ¹³	3.5×10 ¹¹	7.9×10 ¹¹	1.5(0.3)×10 ¹⁴
HMPOs						
00117a	1.1(0.1)×10 ¹²	2.45(0.08)×10 ¹²	1.78(0.06)×10 ¹³	4.3×10 ¹²	9(2)×10 ¹¹	1.8(0.2)×10 ¹⁴
05358b	7.1(0.3)×10 ¹²	1.62(0.06)×10 ¹³	1.38(0.04)×10 ¹⁴	7.2(0.5)×10 ¹²	6.8(0.2)×10 ¹²	6.3(0.3)×10 ¹⁴
18517	8.7(0.1)×10 ¹²	1.95(0.03)×10 ¹³	1.82(0.05)×10 ¹⁴	1.4(0.1)×10 ¹³	7.8(0.3)×10 ¹²	1.07(0.05)×10 ¹⁵
21307	1.29(0.08)×10 ¹²	3.80(0.06)×10 ¹²	5.4(0.2)×10 ¹³	5.5×10 ¹²	1.6×10 ¹²	2(1)×10 ¹⁴
23385	3.8(0.3)×10 ¹²	1.02(0.08)×10 ¹³	7.1(0.2)×10 ¹³	2.8(0.3)×10 ¹²	2.5(0.1)×10 ¹²	4.3(0.3)×10 ¹⁴
UCHIIs						
G75	1.55(0.05)×10 ¹³	3.5(0.1)×10 ¹³	6.2(0.1)×10 ¹⁴	2.3(0.1)×10 ¹³	1.02(0.03)×10 ¹³	1.45(0.06)×10 ¹⁵
19410	1.15(0.04)×10 ¹³	2.46(0.08)×10 ¹³	1.10(0.03)×10 ¹⁴	4.8(0.4)×10 ¹²	1.41(0.03)×10 ¹³	7.6(0.3)×10 ¹⁴
22134	2.19(0.08)×10 ¹²	6.0(0.2)×10 ¹²	4.4(0.1)×10 ¹³	1.32(0.04)×10 ¹³	1.1(0.3)×10 ¹²	2.2(0.2)×10 ¹⁴
23033	4.5(0.1)×10 ¹²	1.20(0.02)×10 ¹³	6.2(0.3)×10 ¹³	5.1(0.4)×10 ¹²	1.9(0.3)×10 ¹²	5.1(0.2)×10 ¹⁴
NGC7538	6.8(0.3)×10 ¹²	1.70(0.06)×10 ¹³	1.02(0.02)×10 ¹⁴	5.5(0.3)×10 ¹²	5.6(0.2)×10 ¹²	6.6(0.3)×10 ¹⁴

Table B.7. Column densities in cm^{-2} of the molecules with three and four atoms

source	CCS	HCS ⁺	p-H ₂ S	OCS	SO ₂	CCCS	o-H ₂ CS
HMSCs							
00117b	$1.3(0.6)\times 10^{12}$	$5.0(0.5)\times 10^{11}$	3.2×10^{12}	3.2×10^{13}	7.9×10^{11}	$1.7(0.2)\times 10^{12}$	$8(1)\times 10^{12}$
AFGLa	$3.8(0.8)\times 10^{12}$	$3.6(0.1)\times 10^{12}$	$2.29(0.06)\times 10^{14}$	$9(1)\times 10^{14}$	2.8×10^{13}	1.0×10^{12}	$9(1)\times 10^{13}$
05358a	$4.3(0.3)\times 10^{12}$	$5.1(0.2)\times 10^{12}$	$6.5(0.3)\times 10^{13}$	$7(1)\times 10^{13}$	$4.6(0.8)\times 10^{13}$	4.0×10^{12}	$9.3(0.3)\times 10^{13}$
20293a	$1.4(0.3)\times 10^{12}$	$9.8(0.6)\times 10^{11}$	1.2×10^{13}	4.0×10^{13}	5.0×10^{12}	$1.0(0.1)\times 10^{12}$	$9(2)\times 10^{12}$
22134b	$5.0(0.9)\times 10^{11}$	$3.7(0.4)\times 10^{11}$	1.1×10^{12}	4.0×10^{13}	7.9×10^{12}	$1.3(0.2)\times 10^{12}$	1.6×10^{12}
HMPOs							
00117a	$1.1(0.2)\times 10^{12}$	$7.9(0.6)\times 10^{11}$	7.9×10^{12}	1.6×10^{13}	5.5×10^{12}	$1.18(0.08)\times 10^{12}$	$1.4(0.2)\times 10^{13}$
05358b	$4.2(0.4)\times 10^{12}$	$4.4(0.2)\times 10^{12}$	$7.1(0.6)\times 10^{13}$	$8(2)\times 10^{13}$	$4.8(0.2)\times 10^{13}$	9.3×10^{11}	$9.6(0.4)\times 10^{13}$
18517	$2.5(0.3)\times 10^{12}$	$3.72(0.08)\times 10^{12}$	$8.1(0.5)\times 10^{13}$	$2.0(0.4)\times 10^{14}$	$2.0(0.2)\times 10^{14}$	$1.3(0.1)\times 10^{12}$	$6.0(0.2)\times 10^{13}$
21307	$7.9(0.9)\times 10^{11}$	$9.6(0.6)\times 10^{11}$	7.9×10^{12}	3.2×10^{13}	3.3×10^{13}	$1.15(0.08)\times 10^{12}$	2.3×10^{13}
23385	$1.7(0.2)\times 10^{12}$	$2.5(0.1)\times 10^{12}$	9.3×10^{12}	$3(2)\times 10^{13}$	$2.5(0.3)\times 10^{13}$	$2.4(0.1)\times 10^{12}$	$3.2(0.2)\times 10^{13}$
UCHIIs							
G75	$2.5(0.3)\times 10^{12}$	$5.9(0.1)\times 10^{12}$	$3.2(0.1)\times 10^{14}$	$4(1)\times 10^{14}$	$3.16(0.04)\times 10^{14}$	$1.2(0.1)\times 10^{12}$	$7.8(0.3)\times 10^{13}$
19410	$2.8(0.2)\times 10^{12}$	$5.50(0.08)\times 10^{12}$	$5.0(0.2)\times 10^{13}$	$6.9(0.8)\times 10^{13}$	$5.1(0.5)\times 10^{13}$	$1.5(0.1)\times 10^{12}$	$8.7(0.4)\times 10^{13}$
22134	$1.5(0.2)\times 10^{12}$	$1.15(0.06)\times 10^{12}$	$3.0(0.5)\times 10^{13}$	5.0×10^{13}	$1.8(0.1)\times 10^{13}$	$3.0(0.3)\times 10^{12}$	$2.4(0.4)\times 10^{13}$
23033	$3.0(0.3)\times 10^{12}$	$3.02(0.08)\times 10^{12}$	$2.5(0.6)\times 10^{13}$	$3.0(0.3)\times 10^{13}$	$2.2(0.1)\times 10^{13}$	8.9×10^{11}	$8.7(0.5)\times 10^{13}$
NGC7538	$2.9(0.3)\times 10^{12}$	$5.4(0.2)\times 10^{12}$	$6.3(0.6)\times 10^{13}$	$7(2)\times 10^{13}$	$1.3(0.1)\times 10^{14}$	6.3×10^{11}	$8.9(0.2)\times 10^{13}$

Appendix C: Plots of fractional abundances versus all evolutionary parameters

In this appendix, we show plots of the fractional abundances of all molecular species analysed as a function of the physical parameters expected to vary with evolution: dust temperature (T_{dust}), kinetic temperature (T_{k} , already shown in Fig. 8), source bolometric luminosity (L), and luminosity-to-mass ratio (M/L).

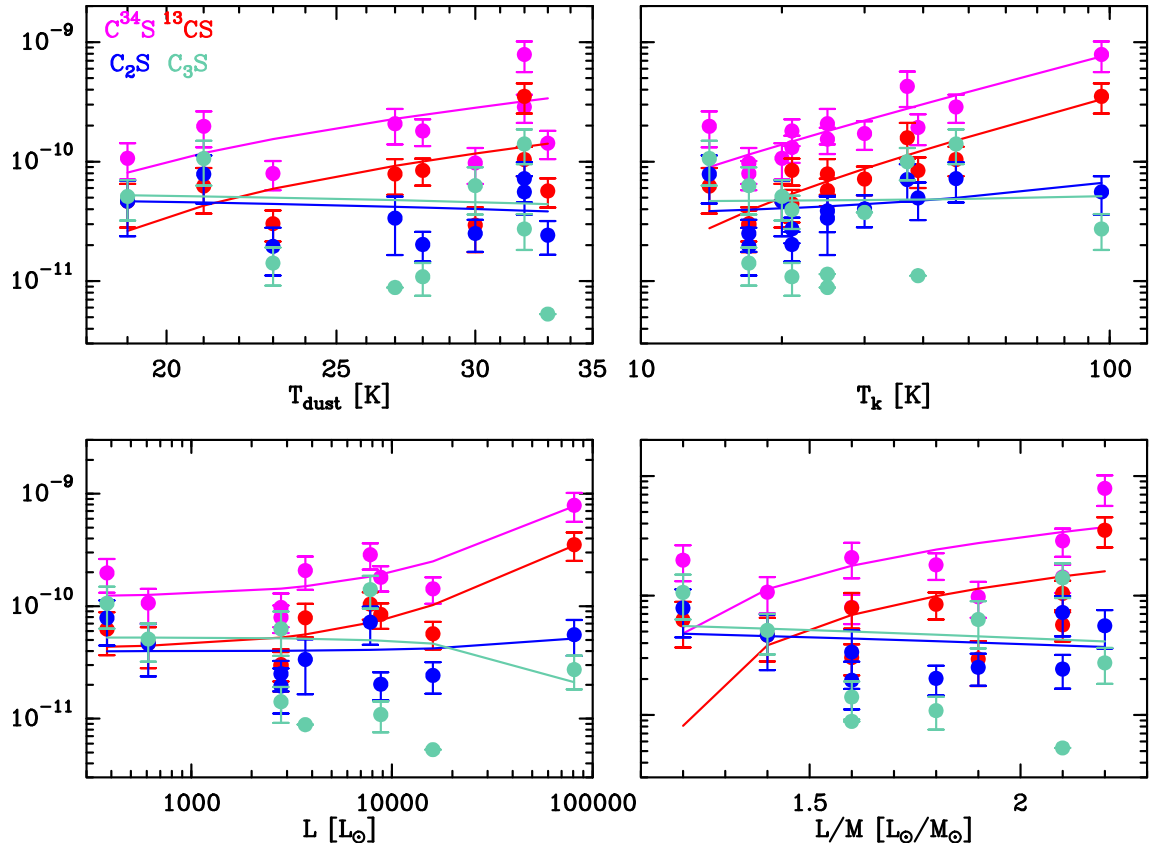


Fig. C.1. Fractional abundances as a function of evolutionary parameters. *Top-left panel:* measured abundances of molecules containing only sulphur and carbon as a function of the dust temperature. T_d was derived by fitting the Spectral Energy Distribution (SED) (Mininni et al. 2021). The symbols without uncertainty are upper limits. The curves represent linear fits to the data including upper limits; *Top-right panel:* same abundances as in top-left panel as a function of the gas kinetic temperature derived from ammonia (Fontani et al. 2011); *Bottom-left panel:* same abundances as a function of the source bolometric luminosity derived from the SED (Mininni et al. 2021); *Bottom-right panel:* same abundances as a function of the luminosity-to-mass ratio (Mininni et al. 2021).

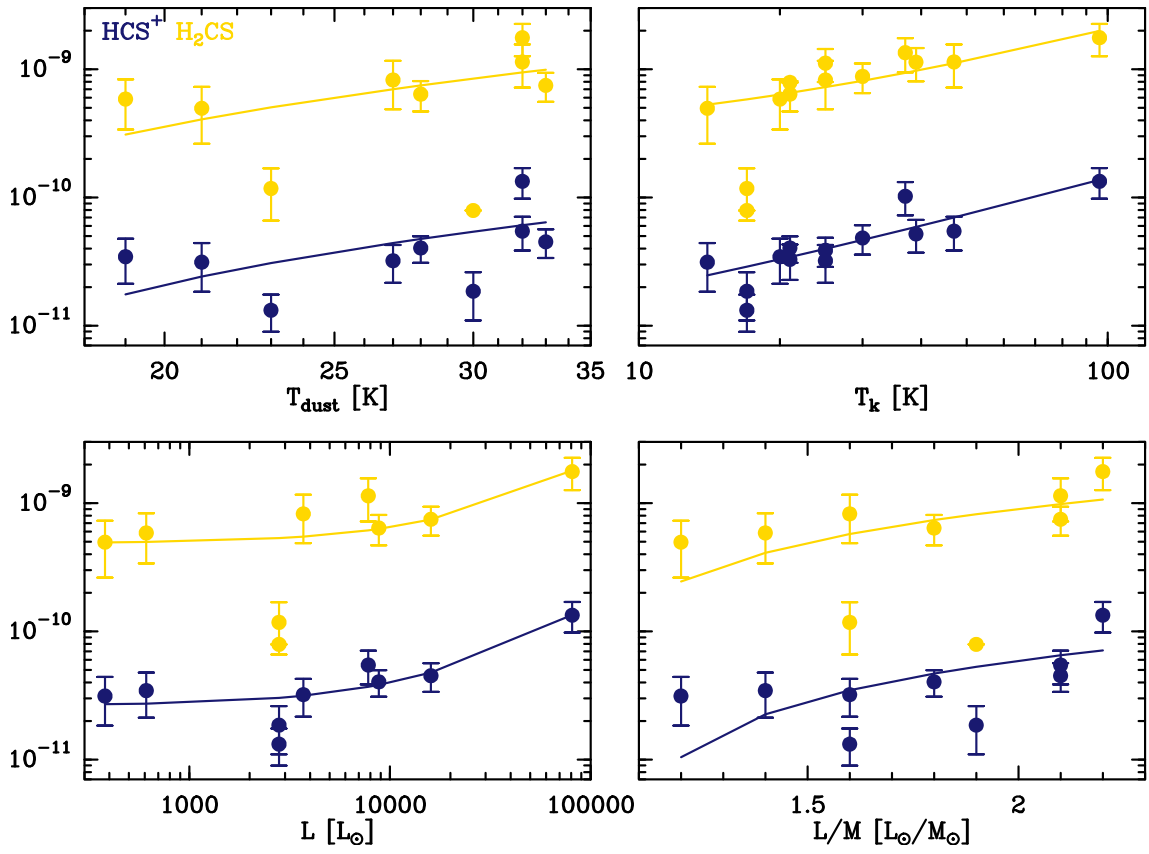


Fig. C.2. Same as Fig. C.1 for molecules containing only sulphur, carbon and hydrogen.

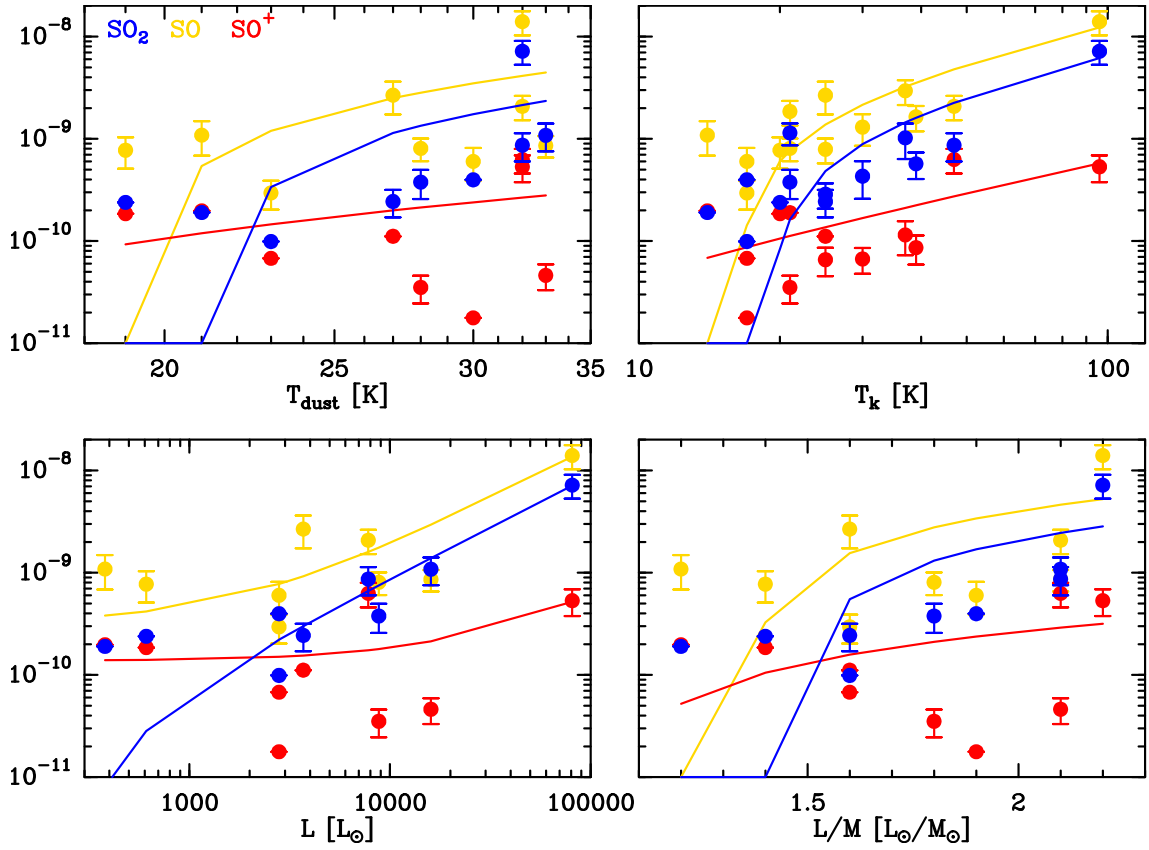


Fig. C.3. Same as Fig. C.1 for molecules containing only sulphur and oxygen.

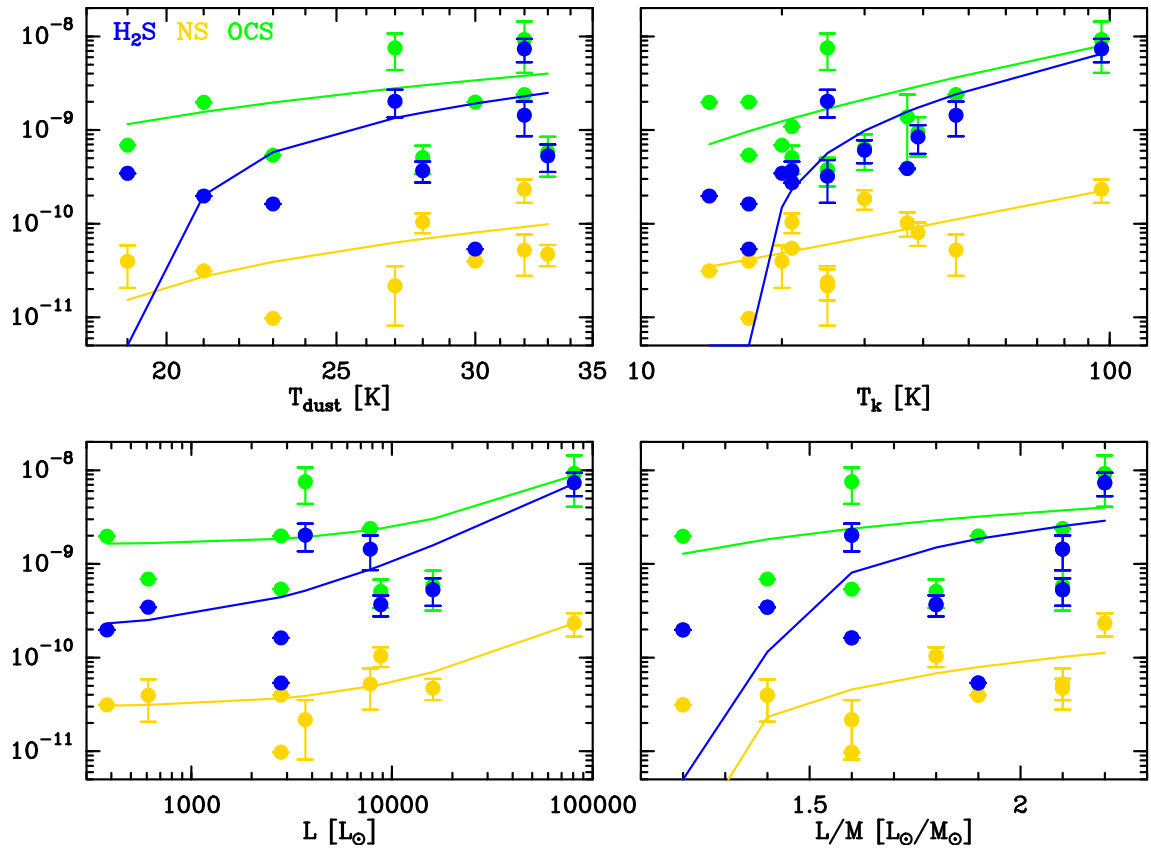


Fig. C.4. Same as Fig. C.1 for all other molecules.